DISSERTATION

FCC-ee Radiation Challenges and Mitigation Measures

Ausgefürt zum Zwecke der Erlangung des akademischen Grades einer Doktorin
der technischen Wissenschaften unter der Leitung von

Privatdoz. Dipl.-Ing. Dr.techn. Michael Benedikt
Atominstitut (E141) und
European Organization for Nuclear Research (CERN)

Dr. Francesco Cerutti (CERN, SY-STI-BMI)
Dr. Anton Lechner (CERN, SY-STI-BMI)

eingereicht an der Technischen Universität Wien
Fakultät für Physik
der Technischen Universität Wien

von
Dipl.-Ing. Barbara HUMANN, BSc
Matrikelnummer 01325686

Wien, am

Unterschrift Verfasser/in

KURZFASSUNG DER DISSERTATION

In einem Teilchenbeschleuniger für Leptonen, wie es die Leptonmaschine des Future Circular Colliders (FCC-ee) sein wird, stellt eine hohe Strahlenbelastung ein mögliches Problem für viele Bereiche des Beschleunigerkomplexes dar. Studien zur Strahlenbelastung leisten einen wertvollen Beitrag dazu, problematische Teilbereiche in der Maschine zu evaluieren und Maßnahmen zur Abschwächung dieser Strahlenbelastung zu integrieren. In dieser Dissertation werden zwei Bereiche des FCC-ee Beschleunigerkomplexes für unterschiedliche Operationsmodi untersucht.

Der erste Teil dieser Dissertation befasst sich mit der Strahlenbelastung in einer möglichen Realisierung der Positronenerzeugungsquelle für den Z Operationsmodus bei 45.6 GeV. In diesem Lösungsansatz erzeugen hochtemperatursupraleitende (HTS) Spulen das Magnetfeld des Adiabatic Matching Devices (AMD), welches die Positronen in Vorwärtsrichtung bündelt, bevor diese in den darauffolgenden Capture Linac geleitet werden. Verglichen zu normalleitenden Spulen erreichen supraleitende Spulen signifikant höhere Magnetfelder, was in weiterer Folge zu einer besseren Positronausbeute führt. In dieser Studie sollen neuartige Hochtemperatursupraleiter verwendet werden, welche höheren Hitzebelastungen durch Strahlen standhalten können. Trotzdem sind diese Materialien anfällig auf Strahlenschäden, was detaillierte Strahlenbelastungsstudien in den Spulen und der Umgebung notwendig macht. Das Target besteht aus amorphen Wolfram, welches aufgrund seiner hohen Ordnungszahl optimal zur Erzeugung von Positronen ist. Durch Bremsstrahlung und Paarproduktion wird im Target ein ausgeprägter elektromagnetischer Schauer gebildet, der eine hohe Strahlenbelastung im Target, den Spulen und dem folgenden Capture Linac induziert. Der Capture Linac ist von normalleitenden Spulen umhüllt, welche die Positronen weiter in Vorwärtsrichtung fokussieren. Am Ausgang dieser Maschine werden die Positronen aus dem elektromagnetischen Schauer gefiltert und nun noch weiter beschleunigt. In dieser Arbeit wird die Energiedepositions mittels dem Monte-Carlo Programm FLUKA berechnet, um die Machbarkeit eines solchen Setups zu evaluieren, wobei zwischen instantanen Effekten und möglichen Langzeitstrahlenschäden unterschieden wird.

Im zweiten Teil dieser Dissertation, werden die Effekte durch Synchrotronstrahlung (SR), welche durch die zirkulierenden Elektronen und Positronen ausgesandt wird, für die Bögen des FCC-ee bei einer Energie von 182.5 GeV ($t\bar{t}$ Modus) untersucht. Bei dieser Strahlenergie wird durch SR eine große Menge an Photonen mit hoher Energie ($>$1.25 MeV) ausgesandt, welche die Maschine schwerwiegend beeinträchtigen können. Um die Strahlenbelastung im Tunnel zu reduzieren, sind lokalisierte Photonenabsorber vorhergesehen. Es werden unterschiedliche Materialien untersucht, und das Modell der lokalisierten Photonenabsorbern wird mit einem Modell ähnlich zu dem von LEP verglichen. Dieses besteht aus einer kontinuierlichen Schicht Wolfram, welches an den äußeren Teilen der Vakuumkammern angebracht ist. Diese Arbeit untersucht die ab-

sorbierte Leistung, die Gesamtdosis (TID) und Teilchenfluenzverteilungen in den Magneten und in der Tunnelumgebung. Des Weiteren werden Optionen für Abschirmungen der Elektronik analysiert und Überlegungen bezüglich der Boosterposition angestellt. Dieser Teil wird durch Studien der Bremsstrahlungserzeugung an Gasmolekülen für den Z Modus 45.6 GeV komplementiert. In diesem Modus ist der Strahlstrom signifikant höher, wodurch der Einfluss von Interaktionen der Strahlteilchen mit Restgasatomen in der Vakuumkammer relevanter wird.

Die unterschiedlichen Themen dieser Dissertation belegen, dass die Strahlenbelastung die Maschine erheblich beeinflusst. Die Belastung erreicht ein Niveau, wo eine Abschwächung der Effekte durch zielgerichtete Maßnahmen dennoch möglich ist. Es wird gezeigt, dass die Strahlenbelastung in den HTS-Spulen der Positronenerzeugungsquelle höchstwahrscheinlich vertretbar sind. Dies stimmt ebenfalls für das Target selbst, sofern ein durchdachtes Kühlungssystem inkludiert wird. Die Strahlenbelastung im Beschleunigertunnel, die von SR herrührt, erreicht ein hohes Niveau, selbst wenn dezidierte Photonenabsorber verwendet werden. In Anbetracht weiterer Schutzmaßnahmen, wie zusätzliche lokale Abschirmungen von kritischen Komponenten oder optimierte Positionierung von Komponenten im Tunnel, wird das Ausfallrisiko dennoch beträchtlich gesenkt werden können.

ABSTRACT

A lepton collider, like the Future Circular Collider lepton machine (FCC-ee), faces various radiation challenges in different parts of the accelerator complex. Radiation load studies are valuable in finding potential showstoppers and mitigating issues, aiming to implement feasible solutions. This thesis studies two parts of the FCC-ee accelerator complex for different operation modes.

First, the radiation load for a possible option of the positron production source is studied for the Z-operation mode (45.6 GeV). This solution features a superconducting solenoid made of high-temperature superconductor (HTS) coils as an adiabatic matching device, which captures positrons produced in the target before they enter the capture linac. Compared to normal-conducting coils, superconducting coils produce a solenoid field with a higher magnetic field strength, improving the positron yield. In this setup, novel HTS coils are implemented that can resist higher radiation loads than common superconducting materials. Nevertheless, these coils still are prone to a high radiation load, which requires a detailed analysis of the power load on the coils and their surroundings. The considered target is made out of amorphous tungsten, which is optimal for positron production due to its high atomic number. Bremsstrahlung and pair production generate a significant electromagnetic shower in the target, implying a high radiation load in the target itself, the superconducting coils, and the capture linac downstream. From this electromagnetic shower, the positrons are then accelerated and at a later stage extracted. The capture linac downstream is embedded in normal conducting solenoids that focus the positrons in the forward direction. Energy deposition calculations with FLUKA are carried out to assess the feasibility of such a setup, studying the heat load and long-term radiation damage on the structure.

The second part of the thesis studies the synchrotron radiation (SR) emitted by electrons and positron beams in the FCC-ee arcs for the $t\bar{t}$-operation mode at 182.5 GeV. At this beam energy, SR includes a vast amount of photons with energies higher than 1.25 MeV (E_c) that heavily impact the entire machine. Dedicated photon absorbers are envisaged as a mitigation strategy to reduce the radiation load on the tunnel. Different materials for the absorbers are investigated and compared to a layout resembling the LEP SR mitigation strategy, which comprises a continuous shielding along the arcs. The study assesses the heat load, time-integrated dose, and particle fluence distribution in the magnets and the surrounding tunnel environment. Furthermore, shielding options for the electronics in the tunnel and considerations for the booster placement are presented. This part is complemented with beam-gas bremsstrahlung studies for the Z-operation mode, where the beam current is significantly higher and hence the impact of interactions with residual gas atoms in the vacuum chamber is more relevant.

The various topics in this thesis show that radiation is significantly impacting the machine, but to an extent where mitigation measures can be implemented efficiently. It is demonstrated that the radiation load on the HTS coils of the positron production target coils is most likely sustainable, which is also true for the target, considering an elaborate cooling scheme. The radiation levels in the collider tunnel are challenging, even if photon absorbers are used. Considering further mitigation strategies, like additional localized shielding of critical components or optimised positioning of components in the tunnel, can effectively reduce the risk of failure.

Contents

ACKNOWLEDGEMENTS

Doing a PhD is a long, interesting, fun, instructive, but also a hard and often times challenging. As it is so often in cycling: only one person gets to step onto the podium, but behind, there is a full team that is there for support. Without this support you would not go far and definitely not be able to do a PhD.

So, first and foremost, I could not be happier than having Dr. Francesco Cerutti and Dr. Anton Lechner as my supervisors on a daily basis. Your knowledge is incredible and your drive and motivation to do research is contagious. Talking about contagious, a good bit of my PhD time was affected by the COVID lock-downs, but during these several months I never felt left alone as I could count on your absolutely crucial support in all areas. I always felt really respected as a person and a colleague, and it was an honour to get more responsibilities during the past months.

Of course, I also want to thank my university supervisor Dr. Michael Benedikt for the opportunity to do my thesis about in the field of future accelerators in this great environment. It gave me the possibility to learn a lot and grow as a person. Thanks for all the opportunities I got regarding schools, workshops and conferences, at times often busy but really instructive and enjoyable.

Thanks also to the many people involved in the FCC-ee project and I was working with more or less closely over the past few years. The SR studies would not have been possible without Roberto Kersevan, who provided a lot of the input and was always open to discuss modifications on the design. The magnets models were kindly offered by Jeremie Bauche, and the several iterations of tunnel geometries were provided by Fani Valchkova-Georgieva. I also want to thank Ruben Alia-Garcia and Giuseppe Lerner for their time, they sacrificed to discuss R2E related issues in the tunnel and gave great input on how to possibly mitigate some issues.

The positron target simulations were performed in close collaboration with several institutes. From the magnet group at PSI I would like to thank Jaap Kosse and Bernhard Auchmann for providing several designs of the positron source, as this process was particularly smooth every single time. Further, thanks to Matthia Schär the input regarding the capture linac and all the additional discussions. Without Paolo Craievich, who is organising the FCC-ee injector programme together, we would not have gone far either. From IJCLab in Paris I need to thank Iryna Chaikovska for all her work as work package leader for the positron target. It is needless to say, I am deeply impressed on how you managed to always be there in such a good a mood, despite all the (outside of work) circumstances. Thanks as well to Salim Ogur for the input regarding the filling scheme of

the accelerator. Last but not least, thanks to Ramiro Mena Andrade and Antonio Periollo Marcone from SY-STI-TCD for the close collaboration in terms of the target design.

I dearly want to thank James Hunt and Daniele Calzolari for the hours they spent with me, trying to figure out why simulations do not run even if they should. Doing a PhD without any immediate application could be lonely, so it helps to have office mates you can turn around to and discuss with them and get a quick feedback. Also thanks to Cesc Salvat-Pujol for the various discussions, sometimes more, sometimes less physics related. I still don't think it is worth bringing a pear to the coffee break to perform "disappear". Jokes aside, thanks for the insights in your incredible knowledge in physics and for the conversations about how to do a PhD.

An especially big thanks to all my friends that were there, encouraging me, spending time with me doing fun stuff, listening to me, getting me out when I didn't really feel like it. So especially thanks to Elli, Ashley, Philippe, Lucie, Oriol, Leyre, Roddy.

Finally, I have to thank my family. Without them I would never be where I was today. Thanks to my mum, supporting me from the early days on and encouraging me on following my dreams. Thanks to my dad, for giving me the confidence to try new things, even if they seem scary at first. I hope, you enjoyed your "Base Camp Geneva". Thanks to my little sister for regularly giving me updates from home and your positive spirits. And thanks to my brother, who often brings me down back to earth, reminding me what really counts.

Last but not least, an immense thank you to my partner, Michi. Thanks for always being there, especially when things get tough, and for the occasional confidence boosts.

Thank you!

This work was funded by the Austrian Fedreal Ministry of Education, Science and Research in the framework of the Austrian Doctoral Student Programme.

List of Figures

List of Tables

List of Acronyms

ABS	Photon absorber
AMD	Adiabatic Matching Device
ARC-DPA	Athermal Recombination Corrected DPA
BC	Bunch compressor
BLT	Beam lifetime
CDR	Conceptual Design Report
CERN	European Organisation for Nuclear Research
CLIC	Compact Linear Collider
DPA	Displacement per Atom
DR	Damping ring
E_c	Critical energy
EC	Energy Compressor
EMF-CUT	Transport threshold for electromagnetic particles
FC	Flux concentrator
FCC-ee	Future Circular Collider Lepton machine
FCC-hh	Future Circular Collider Hadron machine
fedb	FLUKA Element Database
HEH-eq	High energy hadron equivalent fluence
HL-LHC	High Luminosity LHC
HTS	High temperature supcerconductor
LB	Line Builder
LEP	Large Electron Positron Collider
LET	Linear energy transfer
LHC	Large Hadron Collider
MB	Main dipole
MC	Monte Carlo
MDI	Machine Detector Interface
MF	Magnetic field
MQ	Main quadrupole
MS	Main sextupole

NIEL	Non-Ionising Energy Loss
PBR	Pre-Booster Ring
PEDD	Peak energy density deposition
PKA	Primary knock-on atom
pp	per primary
PROD-CUT	Production threshold for secondary particles
PS	Proton Synchrotron
QWT	Quarter wave transformer
R2E	Radiation to electronics
RF	Radio frequency
rms	Root-mean square
RP	Radiation Protection
SEE	Single Event Effect
Si-1MeVN-eq	Silicon 1Mev neutron equivalent fluence
SPS	Super Proton Synchrotron
SR	Synchrotron radiation
TheN-eq	Thermal neutron equivalent fluence
TID	Total ionising dose
TWS	Travelling wave structure
VC	Vacuum chamber
X_0	Radiation length

1

First Chapter

Introduction: Motivation, CERN & FCC-ee

1.1 Motivation

This thesis aims to find mitigation strategies for excessive radiation load in the accelerator complex of the Future Circular Collider Lepton machine (FCC-ee)[1]. The centre of focus is the positron production source, where possibly superconducting solenoids are used, and secondly, the impact of synchrotron radiation (SR) in the collider arcs, where the highest beam energies are observed.

To understand why a new generation of accelerators is studied, the history of accelerator physics should is reviewed. The theory of particle physics started to predict new particles, fundamental particles, which would build the standard model from the beginning of the 20th century. At the time, the means to measure such particles were limited, which gave rise to the technology of accelerators, which developed itself into its own branch of physics. The 700 kV generator, which was used to split lithium atoms with 400 keV protons in 1932, by Cockroft and Walton counts as the birth hour of accelerator physics and the two men were honoured by receiving the Nobel Prize in 1951 [2, 3]. The first circular accelerator was a cyclotron, designed by E. Lawrence, which accelerated protons up to 1.25 MeV[4]. In cyclotrons, the maximum reachable energy is limited by the size of the machine, which led to the development of synchrotrons. The biggest synchrotron to date is the Large Hadron Collider (LHC)[5] at CERN (Conseil européen pour la recherche nucléaire, European Organisation for Nuclear Research)[6].

As the European centre for particle physics, CERN was founded in 1954. It serves as a centre for developing new accelerator technologies and hosts several accelerators and large experiments, where data for ground-breaking fundamental science is gathered. The first synchrotron in place was the Proton Synchrotron (PS)[7], which accelerates protons up to 26 GeV. Nowadays, the PS is used as one of the pre-accelerators in the accelerator

chain leading up to the 27 km long LHC, where protons are accelerated up to 6.8 TeV. The LHC hosts four main experiments, CMS[8], ATLAS[9], ALICE[10] and LHCb[11], which are evenly spaced along the ring. CMS and ATLAS are nearly counterparts, and both detected the Higgs Boson within a short period of time, which was the primary goal of LHC. This detection led to the Nobel Prize for P. Higgs and F. Englert in 2013[12].

Since then, the question has persisted: What will the next significant milestone in particle physics be? First, the baryonic matter in our universe only makes up for 16% of all the matter in the universe. Next to the baryonic matter, there is dark sector which is widely not understood yet. Precision measurements could shed light on this curious part of our universe, which requires outstanding statistics.[13] For performing these measurements, experiments must provide high luminosities to achieve these results, and accelerators must be developed that allow for such collisions.

On one hand, research in accelerator physics is investigating better-performing accelerator technologies, like wakefield accelerators[14], free electron lasers[15] or the Muon Collider[16]. The other approach uses already known strategies but increases the scales of the projects, leading to higher energies, higher luminosities and eventually promising results. Next to FCC at CERN, several projects of this kind are in study at the moment, including CLIC[17], CEPC (Circular Electron Positron Collider)[18] and ILC (International Linear Collider)[19].

In 2020, the European Strategy for Particle Physics (ESPP)[20] gave an update stating:

> *Europe, together with its international partners, should investigate the technical and financial feasibility of a future hadron collider at CERN with a centre-of-mass energy of at least 100 TeV and with an electron-positron Higgs and electroweak factory as a possible first stage.*

This statement launched the FCC feasibility study in 2021, which should provide a feasibility report by 2025, with a mid-term review[21] published in 2023. The baseline for this project is an integrated programme, similar to the history of LHC, where LEP (Large Electron Positron Collider)[22], a lepton machine, was installed in the tunnel first. Such an integrated programme provides the best output, timeline, and overall cost option. If the project gets approved, the physics operation should start by 2040[23].

The first stage, FCC-ee, is operated with energies up to 182.5 GeV[24], which leads to severe radiation load in the collider ring and its surrounding. In other parts of the machine, like the positron production source, superconducting solenoids are foreseen, prone to radiation issues. If possible problems occur, mitigation issues should be implemented. This thesis contributes to the feasibility study with radiation load studies for FCC-ee, adding to a reliable and complete study.

1.2 Outline of the Thesis

This section provides an outline of the thesis. This first chapter discusses the motivation and why this thesis is valuable and needed. Furthermore, the FCC-ee accelerator complex is introduced together with the operational parameters. After reading this chapter, the reader should be knowledgeable about the machine and its different components, as they are a central part of the following chapters.

The second chapter discusses the underlying physics. First, beam physics is introduced as it forms the foundation for the operation of an accelerator. The radiation load in machines is caused by particle matter interactions, which are addressed next. Finally, a whole section is devoted to synchrotron radiation, one of the primary radiation sources in a circular lepton collider.

In the 3rd chapter, the simulation tool FLUKA is introduced after briefly establishing the Monte Carlo method. Furthermore, the quantities observed in the simulations and their impact on machines are discussed.

In Chapter 4, the results concerning the positron production source are presented. This chapter is split into two main parts: the Adiabatic Matching Device (AMD), which includes the positron target, and secondly, the Capture Linac, which follows downstream. In the AMD, a solenoid field is foreseen to be provided by high-temperature superconducting (HTS) coils. It is evaluated if the use of these coils is sustainable, and the positron target is studied in detail. These studies first analyses the properties of the observed particle types, and then in-depth energy deposition studies are elaborated. The second part, which investigates the capture linac, follows the same structure. This structure is analysed in detail, as it has to be understood if cavities suffer from unsustainable heatload and how much the solenoids around the linac are impacted.

Chapter 5 treats the second part of simulation results covering the SR studies for the FCC-ee collider ring arcs. After a reminder of the relevant parameters, the total absorbed power for several layouts in the accelerator components is discussed. Next, mitigation strategies for protecting critical components, mainly electronics, in the tunnel from too much radiation load are compared and discussed. This chapter concludes with an additional section discussing beam-gas bremsstrahlung events in the FCC-ee arcs for the lowest energy operation mode, which is more relevant due to the higher bunch charge.

The thesis is concluded in Chapter 6, summarising the outcomes of the studies. It highlights possible bottlenecks and gives incentives on what should be studied in more detail in the future.

1.3 The FCC Feasibility Study

The FCC (Future Circular Collider) is a feasibility study for a possible future accelerator and collider installed at CERN in the Geneva region (see Fig. 1.1). With a circumference of nearly 91 km, unprecedented energies and luminosities could be reached. FCC is planned as an integrated programme to optimise knowledge gain, cost, and time[23]. First, there will be the lepton machine (FCC-ee), followed by the hadron machine (FCC-hh)[25] on the same footprint. Such an integrated approach has been used successfully with LHC, which was constructed in the same tunnel as the LEP accelerator. With its extraordinarily high luminosity, FCC-ee will serve as a machine for precision measurements up to the $t\bar{t}$ threshold (182.5 GeV per beam), including establishing a better accuracy of the Higgs mass. FCC-hh will explore a terrain of novel collision energies up to 100 TeV, nearly one order of magnitude higher than LHC, hopefully bringing new insights into the physics beyond the standard model. These two modes are possibly complemented by an FCC-eh (lepton-hadron) and an FCC-ePb (lepton-heavy ion) operation, where protons or Lead ions collide.[13]

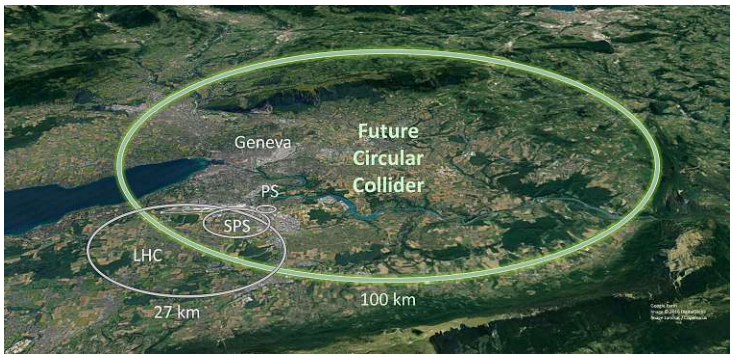

Fig. 1.1. FCC and the accelerator complex in the Geneva basin[26].

The timescale of the project is extensive, reaching until 2095, including the operation of FCC-hh. FCC-ee should run from 2045 to 2063, with FCC-hh following from 2070 to 2095. Considering this timescale, construction should start during the High Luminosity LHC (HL-LHC) operation[27], so the time gap between the collider programmes can be minimal[23].

Generally, the fundamental technologies are already available for FCC-ee nowadays, including areas like magnets, radio frequency (RF) technology[28], and vacuum[29]. The challenge is to design an efficient, sustainable machine that performs optimally. Furthermore, additional R&D efforts are made for particular parts of the machines, like a superconducting solenoid for the positron production or the use of SWELL cavities in the RF section[30].

For FCC-hh, where 100 TeV should be reached, dipoles with fields up to 16 T are necessary. These will be based on Nb_3Sn superconductors, a brittle material that still requires extensive R&D to make the technology usable.[31]

Next, the FCC-ee is discussed in greater detail as it is the subject of study in this thesis.

1.4 FCC-ee

FCC-ee is a lepton machine where electrons and positrons are accelerated and put into collision. This collider type is attractive as extraordinarily clean results are produced in the collisions between fundamental particles. With the achievable high luminosity, precision measurements are possible, a type of research often seen in linear colliders. The advantage of linear colliders is that higher energies[1] can be reached due to the lack of SR, but only one experiment can be put in place. This draws attention to circular colliders, where beams can collide particles often along several experiments along the ring, where high luminosities can be reached. As mentioned, the emitted SR limits the maximum reachable energy.The major advantage of FCC-ee compared to linear colliders is that up to 4 experiments can be hosted in the ring, leading to reliable statistics and the possibility of cross-checking results in the fashion of how ATLAS and CMS co-exist.[24]

FCC-ee has a circumference of 90.657 km, which results in 8 arcs with a length of 9.617 km (see Table 1.1). This translates into a bending radius of 12.24 km. Eight surface sites are foreseen, which allow access to the eight main underground sites. The two (or four) experiments will be located on opposite sides hosted in two (or four) of four short straight sections of 1.4 km. The long straight sections will host technical sites and have a length of 2.031 km. Implementing this design leads to a fourfold symmetry, facilitating the optics design.[32]

Parameter	Optimised 2023
Total circumference	90.657 km
Total arc length	76.93 km
Arc bending radius	12.24 km
Arc length (number)	9.617 km (8)
Length (number) of straights	1.4 km (4), 2.031 km (4)
Superperiodicity	4

Table 1.1. The geometrical parameters for FCC-ee, as they are set by June 2023[32].

The physics runs at FCC-ee are set to be at four different energies ranging from 45.6 GeV (Z), 80 GeV (W), 120 GeV (WH) to 182.5 GeV ($t\bar{t}$). Each energy is selected so that it operates at different particle thresholds, giving the name to the operation modes. The beam current is defined as such that the SR power for the entire collider arcs always stays at 50 MW/beam. Eventually, this means the higher the energy, the lower the beam

[1] In CLIC, the possible future linear collider at CERN, collision energies of electrons up to 3.5 TeV could be reached.[17]

current (see Table 1.2). With the highest bunch intensities forseen at the lowest energies, this means that also the highest luminosity is achieved for the Z operation mode.[24]

The synchrotron radiation energy loss per turn and per particle is nearly three orders of magnitude higher for the $t\bar{t}$ mode than for the Z mode, because the energy loss per turn scales with E^4.

Parameter	Unit	Z	W	ZH	$t\bar{t}$
Beam energy	GeV	45.6	80	120	182.5
Beam current	mA	1270	134	26.7	4.94
Bunches/beam		15880	688	260	40
Bunch intensity	10^{11}	2.43	2.91	2.04	2.64
SR energy loss /turn	GeV	0.04	0.37	1.9	10.0
RMS horizontal ε_x	nm	0.71	2.16	0.67	1.55
RMS vertical ε_y	pm	1.42	4.32	1.34	3.1
RMS hor. IP spot size	μm	8	21	14	39
RMS ver. IP spot size	nm	34	66	36	69
Luminosity/IP	10^{34} cm^{-2}s^{-1}	182	19.4	7.3	1.33

Table 1.2. Accelerator parameters for the four operation modes of FCC-ee. The values are given for one beam each.[32, 33] (Root-mean square (rms); hor./vert. emittance ($\varepsilon_{x,y}$); Interaction point (IP))

Each operation mode should be running for several years. The final order has not been decided yet, but the first proposal had the operation modes follow in ascending energy order. The Z should be performing for 4 years and the W for 2 years. After this time, collision data five and four orders of magnitude higher than what was observed in LEP should be obtained. The Higgs mode follows for 3 years, leading to unprecedented precision measurements of the Higgs boson. After a downtime of approximately a year, FCC-ee should start the $t\bar{t}$ operation mode, which should run for five years. However, this schedule is still subject to change, and a final decision has yet to be taken.[34]

As mentioned several times, SR has a significant impact on circular machines. This thesis tackles the issues occurring due to SR in the arcs, especially in the operation mode with the highest energy. A viable solution must protect the components sufficiently and simultaneously it should be cost-efficient due to the length of the accelerator

1.4.1 | Injector Chain

So far, the collider ring of FCC-ee has been introduced, where particles are stored and collide at top energy, which depends on the operation mode. The particles are injected into the collider at the top energy, which they gain over the length of the injector chain. This section introduces the reader to this part of FCC-ee.

The concept of the accelerator chain is similar to the one of LHC, where several stages of accelerators are necessary to accelerate the particles to their final energy. With many

accelerators in several energy ranges already available at CERN, using existing machines to accelerate the particles could be attractive. For FCC-ee, the injector chain consists of several stages. Compared to a hadron machine like LHC, for FCC-ee, positrons must also be produced and accelerated in this injector chain. Generally, the injector chain can be split into three stages: the pre-injector, Super Proton Synchrotron (SPS) or High Energy Linac, and the booster ring (see Fig. 1.2).[35]

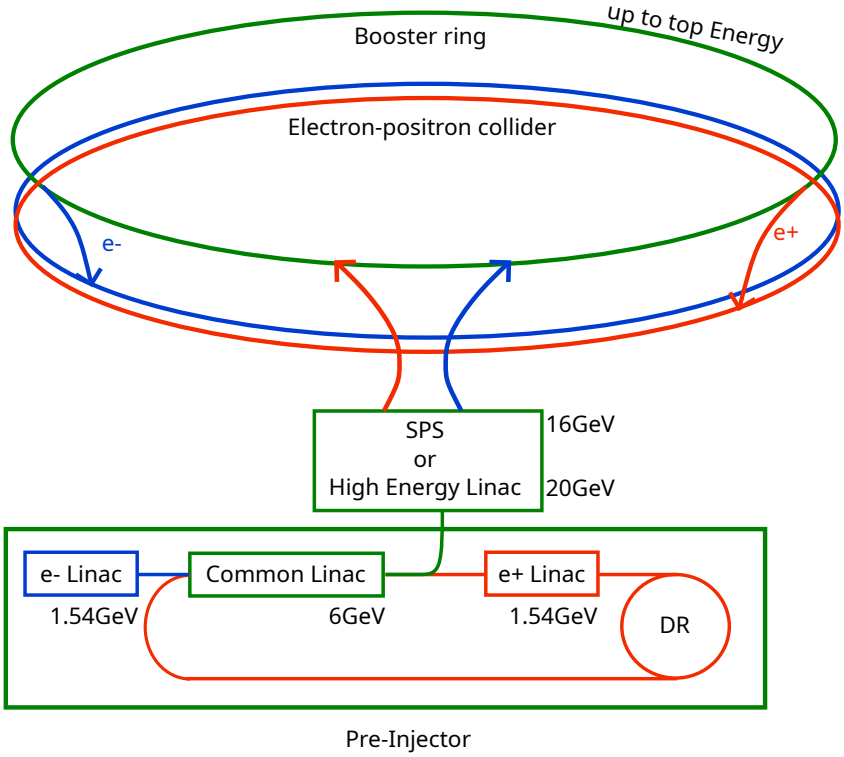

Fig. 1.2. Overview of the injector chain. The particles are produced and accelerated to 6 GeV in the Pre-Injector. In the next stage, either the SPS or a High Energy Linac, the particles reach an energy of 16 GeV or 20 GeV, respectively. In the booster, the electrons and positrons reach the top energy before they are injected into the collider ring.

Figure 1.2 shows that the pre-injector complex has several stages, where electrons and positrons are produced and accelerated to 6 GeV. In the next stage, the leptons are accelerated to up to 16 GeV (SPS) or 20 GeV (HE Linac). So far, no decision has been taken on which machine should eventually be used. Regardless of the decision, the machine always accelerates the particle types separately, meaning the machines are filled with either positrons or electrons. The advantage of the SPS is that infrastructure already exists, but due to the small radius, excessive power loss due to SR is seen, which would not be the case in a linac. The SR power loss limits the maximum energy that can be reached with the SPS, which leads to the 20% lower number of achievable energy (16 GeV instead of 20 GeV with the HE Linac)[36]. The booster ring, placed in the same tunnel as the collider rings, accelerates the electrons and positrons to the top energy, making a

so-called top-up injection possible[37]. Top-up injection allows a constant injection of particles at top energy into the collider ring, which counteracts the short beam lifetime.

Next, the different acceleration stages are discussed in greater detail. The in-depth discussion of the positron production target and the capture linac is be found in Chapter 4, as it is a core part of this thesis.

The Pre-Injector

This section introduces the different components of the FCC-ee pre-injector complex and briefly discusses their use.[38]

The pre-injector complex is an elaborated scheme (see Fig. 1.3), which is used to accelerate electrons and positrons up to 6 GeV. The electrons are produced in an electron gun and then accelerated to 1.54 GeV in an electron linac, within around 90 m. At this energy, the electrons enter the common linac, which accelerates the electrons to 6 GeV. Depending on the on the filling mode (e+ or e-), two different options exist for the electrons at this point. If the electrons should be injected into the collider, they are transferred into an energy compressor and further into the higher energy accelerators. If positrons need to be produced, the 6 GeV electrons enter into the positron production source.

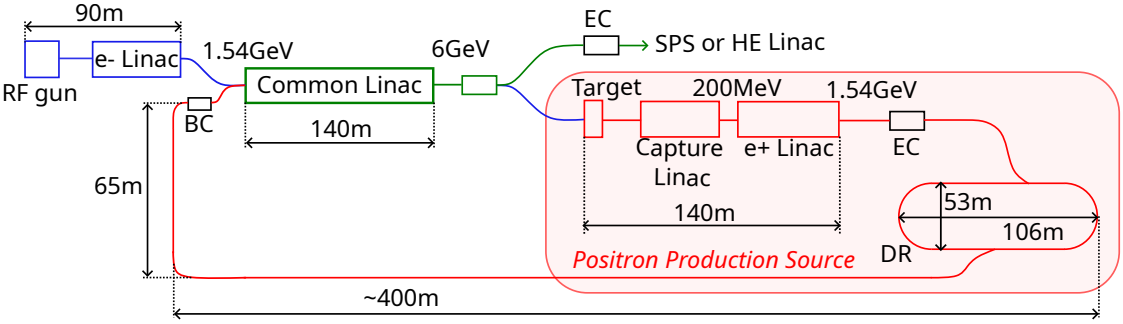

Fig. 1.3. Sketch of the pre-injector complex. Blue lines describe the path of electrons, red the path of positrons, and green lines indicate components that are used for accelerating both types of particles. (The schematic is adapted from [38])

For the positron production, bunches of 6 GeV electrons impact on an amorphous tungsten target. The target is embedded in a structure that provides a solenoid field, also known as the adiabatic matching device (AMD), which is necessary to ensure the positron capture and further improves the positron yield. In this study, the solenoid field is achieved using HTS (High-Temperature Superconductor) coils placed around the target. The produced positrons are shaped into a beam and accelerated to 200 MeV in the capture linac. The positron linac, which follows immediately downstream, accelerates the positrons to 1.54 GeV. In the energy compressor (EC), the energy spread of the beam is reduced before entering the damping ring (DR), which shrinks the angular divergence of the beam. This DR is required so that the beam can be inserted into the common

linac. Before the positrons enter the common linac, the beam passes a bunch compressor (BC) where the bunch length is reduced from 5 mm to 0.5 mm[2]. The positrons are then accelerated to 6 GeV in the common linac and finally transferred into the next stage of the accelerator complex.

In the following, the different components of the pre-injector complex are explained in greater detail.

Electron Source

An RF gun is put in place, which generates electrons for the ring injection and the electrons necessary for the positron production mode. It should provide electrons with a transverse emittance of <4 mm·mrad and a bunch length of 1 mm, so no specific damping ring for the electrons is needed. Simultaneously, charge modulation of 10-100% at 200 Hz has to be possible to account for changes in the electron bunch charge needed for the top-up injection. This variation could be achieved using mirrors that cut parts from the laser that induce the photoemission while the space charge density remains constant.[35, 40]

In the current design, the electron source has a total length of 15 m and consists of four structures. First, there is the electron gun enclosed by a focusing solenoid. The electron gun comprises 2.5 cells with a gradient of 100 MV/m over a length of 0.17 m. It is operated at 3 GHz, the same frequency as the three travelling wave structures (TWS) downstream. The TWS have each 120 cells and a length of 4 m with a gradient of 16.2 MV/m for the first one and 25 MV/m for the other two (see Table 1.3).

	Number of cells	Gradient	Frequency	Length
RF Gun	2.5	100 MV/m	3 GHz	0.17 m
1st TWS	120	16.2 MV/m	3 GHz	4 m
2nd TWS	120	25 MV/m	3 GHz	4 m
3rd TWS	120	25 MV/m	3 GHz	4 m

Table 1.3. Parameters for the components of the electron source, which consists of the RF gun and three travelling wave structures (TWS).

This setup can meet all the bunch property requirements with some margin for a bunch charge of 5 nC. For bunches shorter than 0.5 mm, the emittance would bee too large, while for an emittance <4 mm·mrad, the bunch length would exceed the bunch length limit of 1 mm, not fulfilling the requirements. [41]

[2] Bunch compressors are used to produce high charge density beams. After the source has produced a beam with a small emittance, the density is increased at higher energies with the shortening of the bunch, where space charge effects are no longer dominant.[39]

Electron Linac

The electron linac accelerates the particles from 200 MeV to 1.54 GeV. It linac has a length of 67.5 m and consists of 18 cells with a length of 3 m. It operates at 2.8 GHz with a gradient of 25 MV/m. The FODO lattice has a 90° phase advance, with one quadrupole per RF structure. The electron linac aims to reach the optimal working point, which means 0.1%-0.15% of energy spread at the end of the electron linac while keeping the emittance at an acceptable level. Several scenarios are studied on achieving these requirements, including using a short bunch from the gun, a bunch compressor at the exit of the electron linac, or producing shorter bunches in the gun and applying linearisation downstream. All these solutions have different advantages and disadvantages that must be studied thoroughly.[42, 43]

Common Linac

In the common linac, electrons and positrons are accelerated from 1.54 GeV to 6 GeV. It has a total length of 232.5 m, including 62 accelerating structures of each 3 m. Similar to the electron linac, the phase advance is 90°, and the gradient is found at 25 MV/m.

After the electrons have been accelerated in the common linac, they are either transferred into the further accelerator chain or impinge on the positron target, where they produce positrons. The positrons accelerated in the common linac originate from the positron source and, after the common linac, are also transferred into the further accelerator chain.[43]

Positron Target

While electrons can be relatively simply produced with an RF gun, the positron production is more complex. One possible solution is to use an amorphous tungsten target impinged by 6 GeV electrons. When the electrons enter the 17.5 mm long target, positrons are produced through the bremsstrahlung and pair production effect. The so-called Adiabatic Matching Device (AMD) is a structure providing a solenoid field to enable the positron production by manipulating the phase space of the particles. The aim is to find an AMD solution, which results in the best achievable positron yield, while having a sustainable technical solution. In this project, a novel solution using HTS coils that enclose the target is studied. Such a setup can provide a higher magnetic field and improve the positron yield.[44]

A more detailed description of this component is given in Chapter 4, where the geometry and the operational parameters are discussed in depth. Furthermore, other possible positron production sources are introduced there.

Capture Linac and Positron Linac

The angular spread of the positrons has already been mitigated in the AMD, and the capture linac now forms the particles further into a beam, located around 20 cm downstream of the longitudinal target centre. The capture linac consists of five RF structures surrounded by normal-conducting solenoids that add a solenoid field that focuses the positrons into the forward direction. At the exit of the capture linac, the positrons are accelerated to 200 MeV. Again, a detailed description follows in Chapter 4 as energy deposition studies were performed for this machine part.

Between the two stages of the linacs, there is a chicane where the electrons are separated from the positrons, and only the latter ones continue to be accelerated in the positron linac. Then the positron linac follows, accelerating the beam to 1.54 GeV. In this part of the machine, the RF structure is not enclosed in solenoids anymore. It consists of 14 RF structures, with a gradient of 14 MV/m and 14 quadrupoles. The total length of the positron linac is 58 m, which leads to 120 m for the length of the entire structure from the capture linac to the exit of the positron linac. At the exit of the positron linac, the positron energy is already matches the energy of the common linac. However, other beam parameters, like the energy spread and the emittance, need to be manipulated first so the beam matches the conditions of the common linac. This is done in the downstream energy compressore and the following dampring ring.[45]

Energy Compressor

The energy compressor (EC) manipulates the beam to reduce the energy spread and hence to increase the percentage of positrons that have the correct energy to be accepted downstream in the Damping Ring (DR). The reduction is achieved with a C-shaped chicane and two RF structures downstream. The chicane consists of four 1 m long dipoles with a bending angle of 15°. While the beam energy spread decreases, the beam length increases from 2 mm to 4 cm. Similarly, the horizontal beam dimensions grow. Quadrupoles are used for transverse focusing and dispersion compensation between the dipoles and RF structures. The EC system has a total length of 19 m.[46]

Damping ring (DR)

The positron damping ring reduces the longitudinal and transversal emittance of the positron beam. Longitudinal damping is achieved with SR damping [3], while the horizontal damping is through betatron motion. Crucial for the damping ring design are

[3] For lepton beams, a significant amount of energy is lost at every turn due to SR, which leads to the damping of oscillations and transverse displacement. While the energy loss is recovered in the longitudinal direction in the RF structures, the transverse component is not recovered, and this effect leads to a decrease in the emittance.[47]

wigglers that increase the integrated magnetic field seen by the beam, which leads to a reduced damping time for the same DR length.[47]

The DR for the FCC-ee positron source has a length of 239.2 m following a racetrack layout. The two straight sections house 2+2 wigglers of 6.64 m length each, with a magnetic field strength of 1.8 T. The beam is stored in the DR for 42.5 ms, while the damping time varies from 5.4 ms for the longitudinal component to 10.8 ms for the transversal component. The incoming beam has an energy of 1.54 GeV, and the emittance shrinks from the μm scale to nm.

A DR with three straight sections and three arcs is proposed as a second option. This solution would offer a higher magnetic field, which leads to a shorter damping time. Fewer magnets would be needed, but this would cause the emittance to stay larger. [48, 49]

After the DR, the positron beam moves again through a bunch compressor before entering the common linac. The compression is achieved using a dogleg scheme comprising two triple bend achromats[50]. In the common linac, the 1.54 GeV positron beam is accelerated in there to 6 GeV before it is transferred to another energy compressor and into the next acceleration stage.

SPS or HE Linac

This acceleration stage is used for both particle types, electrons and positrons. Two possible solutions are being investigated: the Pre-Booster Ring (PBR), which is foreseen to be in the tunnel of SPS, or a High Energy (HE) linac. The choice will determine the achievable energy reached in this accelerator stage, which is at 16 GeV for the solution with the SPS and 20 GeV for the HE Linac solution. In SPS, the energy is limited by the large amount of SR emitted due to the small bending radius. When the particles are accelerated to the maximum energy, they are transferred into the booster ring.

The idea to use the SPS as an accelerator stage for FCC-ee is copied from LEP, where the leptons were accelerated from 3.5 GeV to 20 GeV[51]. The use of dedicated SR absorbers was inevitable, even with lower beam currents than what is expected for FCC-ee.[4] For the SPS that is required for FCC-ee, an acceleration to 16 GeV leads to an energy loss of 31.5 MeV/turn, compared to 128 MeV/turn for 20 GeV. Furthermore, the energy spread and the horizontal emittance can be held at a lower level to accelerate to 16 GeV. The current SPS machine cannot withstand these SR properties, which would require an upgraded machine with a new vacuum system with cooled chambers and an adequate absorber layout.[36]

The HE linac covers a length of 615 m over 164 RF structures in 82 modules. The baseline is an S-Band structure that is operated at 2.8 GHz with a voltage of 29.5 MV, and the bunches from the beam are entering the linac with a frequency of 200 Hz. This

[4] Assuming an achieved bunch intensity of 8.6×10^{10} electrons (same for positrons), a beam energy of 18 GeV, and the circumference of 6.9 km, one obtains an energy loss of 8.57 MeV/turn and a total SR power of 5 kW.[51]

linac uses the same RF modules as the electron linac, which makes it cost-efficient for spares. The bunch charge is 4.4 nC for both particle species, which is the same for the solution using the SPS. Similarly to the requests of the RF gun, it is necessary that the bunch-by-bunch intensity can vary between 0% and 100% during the top-up injection for balancing out the collider ring intensities.[52]

Both solutions are investigated for the mid-term review. The final decision will be taken in a later stage of the project, considering feasibility and cost aspects.

Booster

The booster ring, also known as High Energy Booster (HEB), is needed due to the particularities of a lepton machine. A beam in a circular collider at this energy range is lost within a few minutes due to Bhaba scattering, beamstrahlung and SR[24]. The booster ring counteracts this phenomenon as it allows for constant top-up injection into the collider ring, even if the RF system compensates for the energy loss due to SR.

Electrons and positrons enter the booster at 16 GeV or 20 GeV, depending on the machine upstream. In the booster, they are ramped up to the final energy that depends on the operation mode. Ramping up to top-energy takes less than 1 s with a ramp rate around 80 GeV/s-100 GeV/s.

The booster is built on the same footprint as the collider ring on top of the machine due to the lower radiation levels than at the beam level (see Chapter 5). The design of the detector bypasses is still a work in progress. Compared to the collider ring, the machine has only one beam pipe[53], alternately filled with electrons and positrons. The magnets can stay with the same polarization for the operation of electrons and positrons, as the particles only differ in their charges, which means that the electrons and positrons are moving in opposite directions.

The FODO cells have a length of around 52 m, consisting of 4 dipoles, four quadrupoles (1.5 m) and two sextupoles each (0.5 m). The magnetic field strength in the dipoles, which have a length of 11 m, ranges from 6.4 mT at 20 GeV to 59.3 mT at 182.5 GeV. At the injection, the low magnetic field strength poses a challenge.

The particles entering into the booster have an emittance (normalized) of $10\,\mu\text{m}\times10\,\mu\text{m}$. While they are accelerated to 45.6 GeV (Z mode), the emittance shrinks to $<0.3\,\mu\text{m}$ horizontally and <1.4 pm vertically. The energy spread decreases from 0.1-0.15% to 0.04%.[54]

When the particles reach these beam parameters, they are inserted into the collider ring.

1.4.2 | Injection scheme

So far, the layout of the accelerator chain has been discussed. Electrons and positrons go through the acceleration process and eventually enter into the collider ring. An elaborate injection scheme has been developed to guarantee a smooth operation and is discussed now.

The collider ring is filled alternatively with electrons and positrons, which means that the booster is operating once with electrons and then with positrons. If the collider ring is filled from scratch, a so-called bootstrap filling is necessary, which keeps charge imbalances between the two beams at 5% at the Z mode and 3% for the other operation modes. During the top-up injection, the bunch charges must be kept balanced in the collider ring, which requires the injected bunch charges to vary between 0% and 100% in the booster as the lifetime per bunch is different[55].

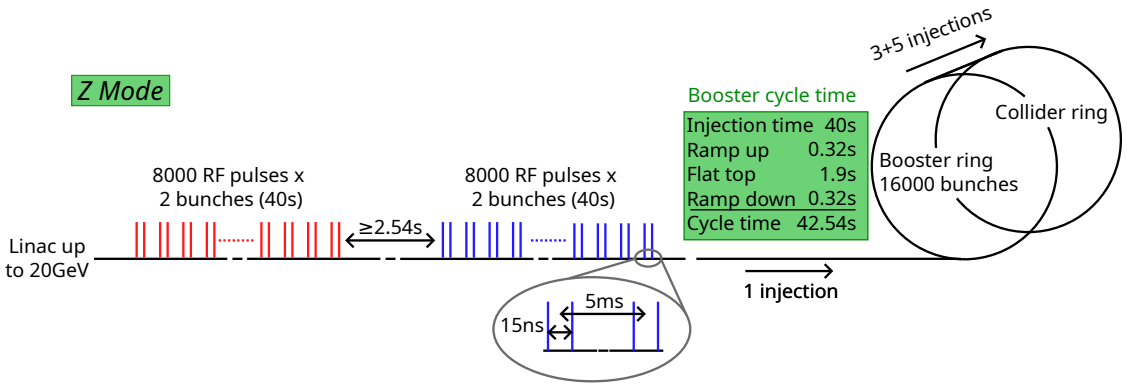

Fig. 1.4. Filling scheme of the injector chain. Blue lines indicate the electron bunches and red lines are the positron bunches. (Plot adapted from [40])

In Fig. 1.4, the filling of the collider is explained in greater detail, assuming the solution using the HE Linac to accelerate the leptons to 20 GeV and a further acceleration for the Z mode. The electrons and positrons, respectively, leave the HE Linac in 8000 RF pulses with two bunches each, so 16000 bunches in total. Between two RF pulses, there are 5 ms and between two bunches, 15 ns. Between a train of electrons and a train of positrons, there is a gap of at least 2.54 s. The 16000 bunches of electrons are injected into the booster[5], which takes 40 s. As soon as all electron bunches are in the booster, the energy is ramped up to top energy, which takes 0.32 s, and then it stays at flat top energy for 1.9 s, before ramping down again for 0.32 s. This leads to a booster cycle time of 42.54 s.

From the booster, the 16000 bunches are transferred to the collider ring. The filling from scratch takes 127.62 s per species, which results in 680.64 s for both beams, which is close around 11 min20 s.

For the top-up injection mode, a time of 42.54 s is assumed per species.[40]

[5]Table 1.2 shows a slightly different value for the total number of bunches. This inconsistency is due to the use of different parameter sets in different groups.

2

Second Chapter

Theoretical background

This chapter discusses the underlying physical principles. First, beam physics is introduced, followed by beam machine interaction mechanisms. The sources of secondary particles are discussed, focusing on those relevant to this project, including synchrotron radiation.

2.1 Short Introduction to Beam Physics

In this section, the physics of beams moving around the accelerator is discussed. Sources like [56] or any CAS proceedings like [57] are recommended for deeper information, as only a short introduction is given here. Even though this thesis is not on beam physics, it is crucial to understand the basics of the operation of an accelerator.

2.1.1 | Lorentz Force and Beam Rigidity

The Lorentz force describes the force a particle experiences in an accelerator,

$$\vec{F}_{\text{Lorentz}} = q(\vec{E} + \vec{v} \times \vec{B}), \tag{2.1}$$

with q being the charge, $\vec{E}$ being the electric field, $\vec{v}$ being the velocity of the particle and $\vec{B}$ being the magnetic field the particle is moving through. For moving particles around an accelerator, electric fields, as well as magnetic fields, can be used. For bending the particle onto the right trajectory in a high-energy accelerator, the magnetic field is superior to the electric field due to the amplification factor of $v \approx c$. Therefore, bending a particle in a high-energy accelerator requires only a small magnetic field compared to the electric field necessary to achieve the same bending. There are some cases of low-energy rings where it is easier to bend the particles with the electric field. For accelerating

particles in RF structures, the electric field is used to accelerate the particles to higher energies.

Assuming that there is a magnetic component in the y direction and velocity in the z direction and all the other components are 0, Equation 2.1 reduces for an electron to

$$F_{\text{Lorentz}} = evB. \tag{2.2}$$

The other force a particle on a bent trajectory experience is the centrifugal force,

$$F_{\text{Centrifugal}} = \frac{\gamma m_0 v^2}{\rho}, \tag{2.3}$$

where again only the longitudinal velocity, v_z, is assumed to be non-zero. In Equation 2.3, $\gamma = \frac{E}{mc^2}$, is the relativistic gamma factor, and ρ is the bending radius of the machine. If those two equations are now set to be equal, one can obtain the beam rigidity,

$$B\rho = \frac{\gamma m_0 v}{e} = \frac{p}{e}, \tag{2.4}$$

that is a normalised measure of how difficult it is to bend the beam. One can approximate the inverse bending radius with,

$$\frac{1}{\rho[\text{m}]} = 0.2998 \frac{B[\text{T}]}{E[\text{GeV}]}. \tag{2.5}$$

In the arcs of the collider, the dipoles bend the beam by a given angle, depending on the magnetic strength. The bending angle α is also given as, $\alpha = \frac{l_m}{\rho}$, where l_m is the magnetic length of the dipole. Over the length of the full ring, an angle of 2π is achieved if all dipoles are added up.

2.1.2 | Frenet-Serret Coordinate System

The optimal trajectory of a particle in an accelerator is the design orbit. On this orbit, turn after turn, the particle is precisely at the same position as it was one turn before. A curvilinear coordinate system is the best choice to describe the orbit, and the transversal plane is described by the coordinates x and y, where the design particle follows along $x = y = 0$ (see Fig. 2.1). In reality, a particle does not stay on this trajectory but deviates from the design orbit due to various physical effects, leading to a displacement in the horizontal and vertical plane.

Longitudinally, the particle on the design orbit follows s, with an arbitrary point chosen as $s = 0$. z gives the longitudinal offset of the particle compared to s tangentially along the ring. With this system, the position of a particle with respect to the design orbit is always known.

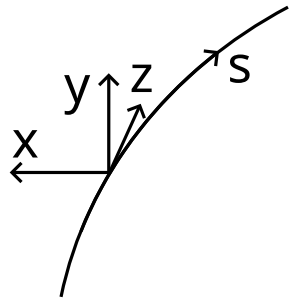

Fig. 2.1. Frenet-Serret Coordinate System.

2.1.3 | Different Magnets

The path of the particles through the machine is defined by the bending of the dipoles and the straight field-free sections in-between. However, the beam particles do not perfectly follow the design orbit but go around the ring with offsets. Higher-order magnets, like quadrupoles, sextupoles, octupoles, and even higher-order magnets, are used to keep the beam focused.

Dipoles, Quadrupoles and Higher Order Magnets

So far, dipoles have been discussed as they are used for bending the particles so they follow the right trajectory. For magnetic fields up to 2 T, mostly iron-dominated magnets can be used[56], while for higher magnetic field strengths, superconducting magnets are needed, like is the case in LHC at CERN[5]. The magnets discussed here have only transversal field components. Dipoles have a component in the horizontal direction, x, or vertical direction, y, while the other ones are zero (see Fig. 2.2). Since a bending in the horizontal plane is needed in an accelerator, the magnetic field is in the vertical direction that can be described with equipotential lines as $y = \pm g$, with $2g$ being the gap between the two poles.

The next higher order of magnets are quadrupoles that focus the beam in horizontal and vertical directions. While the field focuses the beam in one plane, it acts defocusing in the other plane[1], which means focusing and defocusing quadrupoles are needed. Otherwise, the beam would blow up. The field lines in a quadrupole can be described with $xy = \pm\frac{1}{2}R^2$. With that, the magnetic field in x and y can be described as,

$$\begin{aligned} B_x &= -g \cdot y \\ B_y &= -g \cdot x, \end{aligned} \tag{2.6}$$

where g is the gradient, the minus assures that a focusing quadrupole with a positive amplitude leads to a Lorentz force that reduces the amplitude. After dividing g by the beam rigidity, the normalised gradient, $k = \frac{g}{p/e} = \frac{g}{B\rho}$, is obtained.

[1] If the quadrupoles are focusing the beam in the horizontal plane, they are defocusing it in the vertical plane,

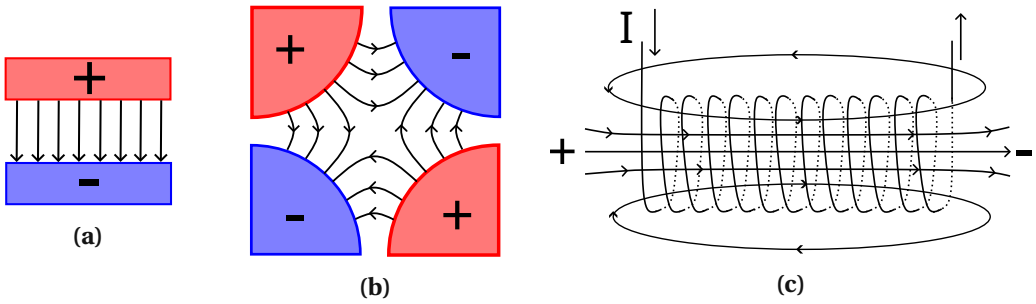

Fig. 2.2. Schemes of magnetic field lines in (a) dipoles, (b) quadrupoles and (c) solenoids.

An iron-dominated quadrupole, as it is relevant for this thesis, is built with four hyperbolic-shaped poles. If this setup is rotated by 45°, one obtains a so-called skew quadrupole that can be described as $(x^2 - y^2) = \frac{1}{2}R^2$. Perfectly shaped field lines are only achieved by infinite parabolas. In reality, so-called shimming on the edges has to be added to manipulate the magnetic field lines so they resemble a perfect quadrupole as much as possible[57].

Higher-order magnets like sextupoles and octupoles are used to correct higher-order beam errors.

These higher orders magnets lead to more complex fields. The full normalised magnetic field can be described using a Taylor expansion as follows:

$$\frac{B(x)}{p/e} = \frac{1}{\rho} + kx + \frac{1}{2!}mx^2 + \frac{1}{3!}nx^3 + ... \tag{2.7}$$

For $B(y)$, this would look quite similar, only that the first term disappears as the bending in dipoles only happens in the horizontal plane. The second term describes the quadrupole, the third one the contribution of the sextupoles, and the higher-order terms describe the contribution from the higher-order magnets.

It is also possible to build combined function magnets, where by shaping the poles in a certain way, the field lines result in a field that one obtains by overlapping a quadrupole and dipole field. However, they are usually not used for the collider ring but more for special cases like transfer lines.[56]

Solenoid Fields

So far, the discussed magnetic fields only have transversal but no longitudinal component. However, for special applications, a magnetic field in the longitudinal direction, a solenoid field, is helpful. They are used, for example, in the CMS experiment, which stands for "Compact Muon Solenoid"[8], but also in specific locations of an accelerator

and vice versa.

chain, like the positron production source. Here, the magnetic field helps to catch the particles that otherwise form a highly divergent beam. However, this magnet type is not commonly found in storage rings or synchrotrons[56].

In a solenoid, the current is going through cylindrical coils that provide a magnetic field, with components in the longitudinal direction, B_z and components in the radial direction, B_r. Due to symmetry considerations, the angular contribution B_φ evens out to 0. In the centre of the solenoidal field, the radial component also vanishes. The radial component is the most dominant in the fringe fields, where the magnetic field lines turn back to close the loop (see Fig. 2.2).

The magnetic field strength is calculated using Stoke's theorem, which leads to

$$B_0(x=0, y=0) = \mu_0 \mu_r J, \tag{2.8}$$

with μ_0 being the magnetic permeability, μ_r being the relative permeability and J the current that flows through the coils. The current is directly proportional to the achieved magnetic field. In other words, the maximum of the magnetic field is limited by the current in the coils. Therefore, superconducting coils are discussed in Chapter 4 as they can carry higher currents.

2.1.4 | Transversal Beam Dynamics: Equation of Motion, Phase Space, Emittance, and Divergence

The equation of motion describes the movement of a particle. The radial acceleration a_r a particle experiences is given as

$$a_r = \frac{d^2\rho}{dt^2} - \rho\left(\frac{d\theta}{dt}\right)^2, \tag{2.9}$$

with θ being the bending angle of a dipole magnet. The first term describes the change in the bending radius for a particle following the design orbit, which is 0. For the general case, where the particle has a transversal offset, ρ should be replaced by $\rho + x$. The second term describes centrifugal acceleration. In the next step, the equilibrium between the centrifugal force and the Lorentz force has to be found,

$$F = m\frac{d^2}{dt^2}(x+\rho) - \frac{mv^2}{x+\rho} = evB. \tag{2.10}$$

Using $B_y = B_0 + x\frac{dB_y}{dx}$ and $x' = \frac{dx}{ds} = \frac{dx}{dt}\frac{dt}{ds}$, one finally obtains the following equations of motion for the particle in x and y:

$$\begin{aligned} x'' - x(k - \frac{1}{\rho^2}) &= 0 \\ y'' + yk &= 0. \end{aligned} \tag{2.11}$$

In the x component, there is an additional term, $1/\rho^2$, that describes the phenomenon of weak focusing in dipoles. The term in the bracket is often defined as $K := \frac{1}{\rho^2} - k$. The vertical dipole field does not impact the vertical beam component, so this term does not appear in the equation for y. Both these equations resemble the harmonic oscillator, so similar solutions can be found for x and y. The solutions for x and x', with as x_0 as amplitude and x_0' as angle, can be found at:

$$\begin{aligned} x(s) &= x_0 \cdot \cos(\sqrt{|K|}s) + x_0' \cdot \frac{1}{\sqrt{|K|}} \sin(\sqrt{|K|}s) \\ x'(s) &= -x_0 \cdot \sqrt{|K|} \sin(\sqrt{|K|}s) + x_0' \cdot \cos(\sqrt{|K|}s). \end{aligned} \tag{2.12}$$

These equations can be put into a matrix that makes the handling more convenient:

$$M_{\text{foc}} = \begin{pmatrix} \cos(\sqrt{|K|}s) & \frac{1}{\sqrt{|K|}} \sin(\sqrt{|K|}s) \\ -\sqrt{|K|} \sin(\sqrt{|K|}s) & \cos(\sqrt{|K|}s) \end{pmatrix} \tag{2.13}$$

for a focusing quadrupole. For the defocusing quadrupole, the matrix changes as the magnetic field is rotated concerning the focusing quadrupole,

$$M_{\text{defoc}} = \begin{pmatrix} \cosh(\sqrt{|K|}s) & \frac{1}{\sqrt{|K|}} \sinh(\sqrt{|K|}s) \\ \sqrt{|K|} \sinh(\sqrt{|K|}s) & \cosh(\sqrt{|K|}s) \end{pmatrix}. \tag{2.14}$$

The drift space between two quadrupoles is described with the following simple matrix,

$$M_{\text{drift}} = \begin{pmatrix} 1 & s \\ 0 & 1 \end{pmatrix}. \tag{2.15}$$

As already discussed, if a quadrupole focuses the beam in one plane, it defocuses the beam in the counter plane. However, a combination of magnets in the accelerator must be found where finally the beam is focused. This condition can be achieved with a so-called FODO cell consisting of a focusing quadrupole, a drift space, a defocusing quadrupole and another drift space. As it is more convenient to have a symmetric cell, it is usually defined from half of a focusing quadrupole and ends with the other half of the focusing quadrupole. These periodic cells, repeating themselves many times, usually make up the building blocks of the arcs in an accelerator.

Emittance and Twiss Parameters

So far, a single particle moving through the accelerator has been discussed, but a beam consists of many particles, which can be described as an ensemble of particles. Each particle is characterised by a set of 6 parameters (x, p_x, y, p_y, s, E), which makes the particles distinguishable. For systems where the energy E does not change, p_x and p_y can be replaced by x' and y', meaning the slope of the particle trajectory. This assumption is possible as small angles are assumed, so $\sin(x') \approx x'$. Furthermore, if $\Delta E = 0$, there

is no coupling between the horizontal and vertical planes. The lack of coupling makes it possible to split the 6D phase space into 3×2D phase space, which is much easier to handle.

The area that the particles occupy in the phase space is called emittance, ε, which is one of the most important parameters to describe the beam. If the planes are decoupled, the beam has three independent emittances, one in x, one in y and one longitudinal one, and generally, it is held as low as possible. If it exceeds a certain limit, the vacuum chamber can be touched, which must be avoided. Due to Liouville's theorem that states that the phase space must stay constant, the emittance stays constant along a beam transfer line. However, the emittance changes with the energy of the particles. To account for this, a normalised emittance, ε_n, is introduced and it has the following form:

$$\varepsilon_n = \beta\gamma\varepsilon. \tag{2.16}$$

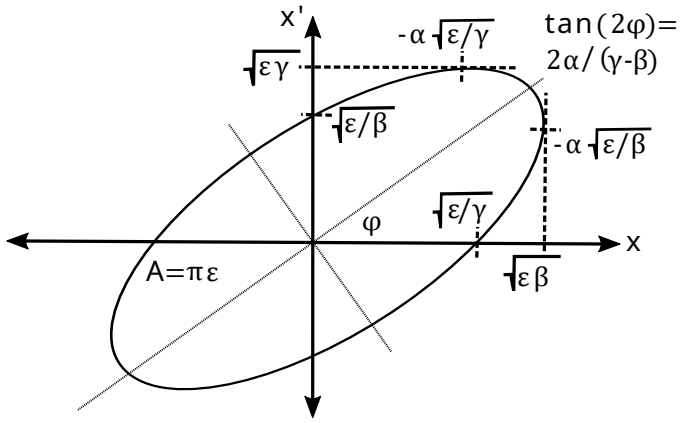

Fig. 2.3. Phase space ellipse with twiss parameters indicated.

The ellipse of the emittance can be described as

$$\gamma x^2 + 2\alpha x x' + \beta x'^2 = \varepsilon, \tag{2.17}$$

where α, β and γ are the so called Twiss parameters (see Fig. 2.3) fulfilling $\beta\gamma - \alpha^2 = 1$. These coefficients must not be confused with the relativistic parameters β and γ[2]. The area of the ellipse is given as $A = \pi\varepsilon$. Every particle in the beam moves along a different ellipse within the envelope ellipse without ever leaving the envelope.

While the shape of the ellipse changes moving through the line, the area stays constant. If the ellipse is located in the first and third quadrant, it translates into a diverging beam, and vice versa.

As in the previous section, the equation of motion for the beam is the baseline. The form is fairly similar to the description for a single particle, only without the term for weak focusing. Instead it has periodically repeating elements that show in $k(s) = k(s+L)$,

[2] Usually, one know from context if either the Twiss parameters or the relativistic parameters are meant.

$$x''(s) - k(s) \cdot x(s) = 0, \tag{2.18}$$

which is also known as Hill's equation. The solutions for $x(s)$ and $x'(s)$ now include the Twiss parameters, especially $\beta(s)$, also known as the betatron function:

$$\begin{aligned} x(s) &= \sqrt{\varepsilon}\sqrt{\beta(s)}\cos(\psi(s) - \phi) \\ x'(s) &= \sqrt{\varepsilon}\sqrt{\beta(s)}\left(\frac{1}{2}\beta'(s)\cos(\psi(s) - \phi) + \sin(\psi(s))\right), \end{aligned} \tag{2.19}$$

where ψ is giving the phase oscillation and ϕ is given by the initial condition.

The periodic betatron function gives amplitude of a transverse oscillation of any particle at a certain location s along the ring. The number of oscillations per turn per revolution unit of 2π is also known as tune, Q, of a machine, which has crucial impacts on designing a working lattice for a machine.

Dispersion

So far, transversal beam effects have been discussed, but particles of a beam also have an energy spread. A distribution of particles with respect to their energy or momentum is visible, which is usually in the range of $\frac{\Delta p}{p} \approx 1.0 \cdot 10^{-3}$.

This effect impacts the beam stability negatively, as it leads to changes in the bending of the beam or focusing strength for offset particles. So if a particle with too little energy comes into a dipole, it is bent more than it is designed for, while for a particle with higher momentum, it is bent less.

Taking the energy spread into account, the equation of motion changes into a heterogeneous differential equation,

$$x'' + x(\frac{1}{\rho^2} - k) = \frac{\Delta p}{p} \cdot \frac{1}{\rho}. \tag{2.20}$$

This implies that a solution in form of

$$x(s) = x_\beta(s) + x_i(s) \tag{2.21}$$

has to be found, with the first term being the solution for the situation without energy spread. Here, the dispersion is introduced, which is defined as

$$D(s) = \frac{x_i(s)}{\Delta p / p}, \tag{2.22}$$

and can be calculated analytically by beam optics codes. Similar to the betatron oscillation that describes the orbit offset for a particle with ideal momentum, the dispersion function describes the offset arising from a momentum deviation.

2.1.5 | Time Structure

In an accelerator, the beam has a continuous structure or is bunched. In storage rings, the beams are usually bunched, as acceleration with the RF structures is convenient. A bunch pulse is defined by the duration of an RF pulse and is split into smaller micro-bunches. For a typical C- or S-Band linac, the pulse duration is usually in the range of μs[58].

As a time structure is attached to the beam, different definitions of currents exist that depend on the regarded time span. The average current is defined as

$$\langle I \rangle = \frac{n_\mu q}{T_{\text{rep}}}, \tag{2.23}$$

with n_μ being the number of micro-bunches per pulse, q the charge in one micro-bunch and T_{rep} the repetition time.

Another time-related property that must be considered is the duty factor of a machine, which describes the actual beam time available for an experiment. A typical number for the duty factor is around 80%, which is also the case for the FCC-ee machine[50], as it will be discussed at a later stage.

2.2 Beam Machine Interaction

This section and the following discuss the beam-machine interaction. While this section stays more qualitative in discussing the beam-machine interaction, the following section quantitatively discusses the physical phenomena.

In the previous section, where beam physics was discussed, it was assumed that the beams move through a perfect vacuum without any disturbances, which is far from reality. In an optimal machine, the beam particles would circulate infinitely long in the ring, which is not the case as all beam particles and secondaries will eventually interact with the environment or decay at some point. In a collision point, these interactions are deliberate, but for the rest of the accelerator they are destructive. Therefore, the reasons for the interactions must be well understood and mitigated if necessary.

The underlying physical processes represent a vast spectrum of different atomic and nuclear processes. The effects seen in hadrons can be highly complex, less so for leptons, which are the centre of attention in this thesis. These processes are discussed in more detail in the next section.

The interactions between the beam and the machine lead to different effects on the machine. Generally, one distinguishes between long-term radiation effects that lead to material degradation over time and instantaneous effects that can lead to heating of the material and limits the operation of the machine in this way. The related physical quantities can be calculated with codes like FLUKA (see Chapter 3), and the risks can be assessed and mitigated if needed.

This chapter is mainly based on information from [59].

2.2.1 | Beam Intercepting Devices

Usually, the beam is meant to go through the accelerator with as little interaction as possible. In some cases, these interactions are deliberate and forced.

Over time, the quality of the beam degrades due to various factors, up to a point where it is more beneficial to dispose of the beam and insert a new one into the machine. For disposal, the beam is steered on a dump where the beam impacts. The huge impact of beams on the dump leads to a high strain on the material. Depending on the machine, the activation of the material is another issue. Hence, studying and developing beam dumps is highly important when designing a collider.

Another area where beam intercepting devices are used is in the field of machine protection or beam manipulation. Typical tools are collimators placed in locations where the halo around the beam should be removed to achieve a beam as clean as possible, for example, next to the experiments.

For completeness, devices for beam extraction, like stripping foils or crystals, should also be mentioned. These devices are used to manipulate a beam to transfer it from one accelerator to the next. The devices manipulate the beam in different ways. Stripping foils can change the charge of the circulating particles, and bent crystals are used for

selecting specific particles with the right angle with respect to the crystal axis while simultaneously discarding the other particles.

Finally, beam intercepting devices are often used for particle production on targets, like in neutron facilities where spallation targets produce neutrons[60]. This thesis uses a target to produce positrons from impacting electrons. The radiation of such a target can be hostile for machine components as the dose and heat load levels are potentially high. Therefore it is essential to study this region in great detail.

2.2.2 | Sources of Secondary Particles

The beam intercepting devices just discussed are a source of secondary particles. However, secondaries are also produced due to various other effects.

A large contribution of secondaries is due to luminosity production, meaning collisions in experiments. While the majority of the secondaries goes into the different detectors that are enclosing the collision point in a cylindrical shape, the most energetic particles are scattered in forward direction. They exit the experiment and enter back into the collider. The long straight sections just next to the collider often host superconducting magnets [61] which makes it important to study the energy deposition there.

In the collider, the beams circulate in vacuum chambers, where the machine requirements determine the quality of the vacuum. A higher vacuum is more beneficial for a stable beam, but similarly is more expensive and harder to maintain. The lower the quality of the vacuum, the more likely collisions between the beam and the residual gas in the vacuum chamber. For hadrons, this leads to inelastic scattering events. More relevant in this thesis are the interactions with electron and positron beams, which lead to bremsstrahlung losses (see Section 2.3.5) where beam particles can lose significant energy. If the RF system does not constantly replace this energy, bremsstrahlung shortens the beam lifetime. The underlying physical theory of bremsstrahlung losses is discussed in the following section.

The vacuum chambers must be thoroughly cleaned before a machine is operated. Otherwise, dust or other macroscopic objects can interact with the beam and induce unwanted losses.

Regarding circular electron-positron colliders, synchrotron radiation is a primary source of secondaries. Here the beam loses significant energy in the form of photons. These photons impact somewhere else on the machine, and the beam lifetime decreases due to this effect, which requires compensation by the RF system. The machine can be protected by placing absorbing material in the way of the SR photons. As this type of secondary production plays a significant role for FCC-ee, SR is discussed in great detail in the section.

2.3 Quantitative Description of Secondary Particle Production

The previous section discussed the basics of beam-machine interaction, focusing on the macroscopic effects and their consequences. This section delves into the underlying physics of these effects, which are also the foundation of this thesis. FCC-ee is a lepton machine, so the occurring effects are mainly electromagnetic, caused by electrons, positrons, and photons, which are all stable particles. Electrons and positrons are charged negatively and positively, respectively, with a mass of 511 keV/c. Photons are the gauge bosons for the electromagnetic force and are massless. Furthermore, effects caused by neutrons are also covered due to their possibly severe impact on the machine.

This section introduces the relevant electromagnetic effects, including, Bremsstrahlung, pair production, and Compton scattering[3]. Furthermore, photo-nuclear effects are discussed.

This section is mainly based on the literature such as [59] and [62, Chapter 30].

2.3.1 | Interaction Probabilities, Cross Section and Mean Free Path

The cross-section characterizes the probability of an interaction between two particles happening. Several definitions exist for different types of cross-sections, and three of them are discussed here.

The **microscopic cross-section**, σ, is commonly given in the unit of barn, where $1\,\mathrm{b} = 1 \times 10^{-24}\,\mathrm{cm}^2$. The area given as the cross-section is directly proportional to the probability of the reaction happening. The size of the microscopic cross-section depends on the energy and the type of the atoms, the mass, A, and the charge, Z.

The microscopic cross-section correlates directly with the **mean free path**, λ, which gives the average distance a particle travels between two collisions in m. As said, the mean free path is the inverse of the product of the microscopic cross-section, the material density, ρ, and the Avogadro constant, N_A,

$$\lambda = \frac{1}{N_A \rho \sigma}. \tag{2.24}$$

Equation 2.24 shows that a larger σ and a higher density lead to a shorter distance between interactions. If the material is a compound, the different relative weights of the constituents must be considered.

The inverse of the mean free path,

$$\Sigma = \frac{1}{\lambda}, \tag{2.25}$$

is also known as the **macroscopic cross-section**, with the units of cm^{-1}. It measures the likelihood of an interaction happening per unit length.

[3] Synchrotron radiation (SR) is another electromagnetic effect. Due to its complexity and importance in this thesis, the next section is dedicated to SR and not further discussed here.

The interaction probability for a particle moving through a homogeneous material is given with

$$p(l)dl = \frac{1}{\lambda} e^{-\frac{l}{\lambda}} dl, \tag{2.26}$$

with l being the distance travelled by the particle. If the particle travels indefinitely far through the material, at some point, there has to be an interaction leading to

$$\int_0^\infty p(l')dl' = 1. \tag{2.27}$$

The probability of a particle having interacted with the matter within a certain length, l, is calculated with the cumulative distribution function,

$$P(l) = \int_0^l p(l')dl' = 1 - e^{-\frac{l}{\lambda}}. \tag{2.28}$$

The probability that the particle has undergone an interaction after λ is around 63%, after 2λ, the probability is around 86.5%, and at 95% for 3λ.

The exponential function can be expanded in a Taylor series for a thin target, meaning $d << \lambda$, with d being the target thickness, which leads to $P(d) \approx \frac{d}{\lambda}$. Here, the interaction probability is simply given by the ratio of the target thickness and the mean free path length.

Finally, there is the **differential cross section**, $\frac{d\sigma}{d\omega}$, which is a measure for the probability of the particles being scattered into a solid angle (see Fig. 2.4). If a particle scatters on another particle within an impact parameter of b and $b + db$, it is scattered with an angle of θ to $\theta + d\theta$. The area of the small ring is $d\sigma = 2\pi b db$, whereas the large ring has an area of $d\omega = 2\pi\theta d\theta$[4]. The differential cross section now gives the ratio between the small and large rings, resulting in a characteristic value for different combinations of two particles. Additionally, there is the **double differential cross section**, which measures the probability of a particle being scattered into a certain angle with a specific energy, $\frac{d\sigma}{d\omega dE}$.

2.3.2 | Photon interactions

Now an overview of electromagnetic interactions is given, including interactions of electrons ($e-$), positrons ($e+$) and photons (γ). Some specific effects like Bremsstrahlung and Synchrotron Radiation are later explained in greater detail, as they are the main effects causing energy deposition for the projects in this thesis. In the following, the effects are discussed in increasing order of the energy domain, where these phenomena are relevant.

[4] Assuming small θ, so $\sin(\theta) = \theta$.

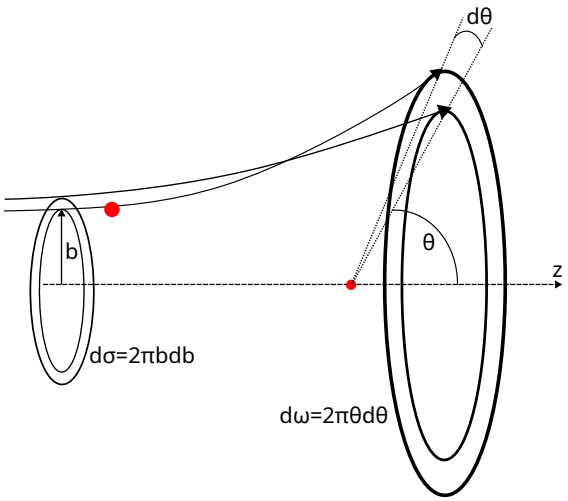

Fig. 2.4. Differential cross section schematic.

For **Rayleigh scattering**, also known as coherent scattering, the incoming photon is scattered on the atomic electron without ionising the atom. As shown in Fig. 2.5, Rayleigh scattering is never the dominant contributor to the cross-section, which scales with Z^2. In accelerators, this kind of scattering usually is negligible, as it does not contribute to any absorption or emission of photons or other electromagnetic particles.

If the incoming photon is absorbed, and an electron is released from the atom, the effect is called **Photoelectric effect**, proposed by Albert Einstein and resulted in a Nobel prize in 1921 [63]. The energy of the released electron, $E = E_0 - U_i$, is equal to the difference between the incoming photon energy, E_0, and the binding energy of the electron to the atom, U_i. The energy of the incoming photon must exceed the binding energy for the electron to be emitted. If the incoming photon interacts with an electron of an inner shell, the emission is followed by an atomic relaxation of an electron from an outer shell jumping down to the vacancy. This atomic relaxation leads to an emission of an X-ray or a so-called Auger electron.

The photoelectric effect dominates at energies up to tens of keV for high Z materials and up to hundreds of keV for low Z materials. The cross-section of this interaction depends strongly on the atomic number of the material with $\propto Z^{4-5}$.

In the range of MeV the cross section is dominated by **Compton scattering**. The dominant range varies strongly for different materials. With a cross-section dependence on the atomic number of $\propto Z$, the Compton-dominated region is much smaller for high Z than low Z materials.

In this process, also known as incoherent scattering, an incoming photon with the energy E_0 hits a bound atomic electron. The incoming photon transfers some of its energy to the electron, and both particles are scattered under an angle, while the energy of the incoming photon splits into $E_0 = E_0' + E_{e-}$. The amount of energy transferred from

the incoming photon to the electron is not pre-defined and can range from nearly zero to a significant fraction of the photon's energy. This effect is crucial in the chapter about photon absorbers, as this mechanism is dominant there.

If the energy of the incoming photon exceeds 1.022 MeV and it moves in the field of a nucleus, **pair production** happens, where a photon produces an electron-positron pair.The threshold energy of the effect is defined by the sum of the rest mass of an electron and a positron. The cross-section of this effect scales with Z^2, so it depends stronger on the atomic number than Compton scattering. As it can be seen in Fig. 2.5, for the case of higher Z materials, like lead, pair production is the dominating effect at already 5 MeV, while it is only at 25 MeV for carbon. Together with Bremsstrahlung, explained later in greater detail, pair production is responsible for the electromagnetic shower development and is used for positron production in positron targets.

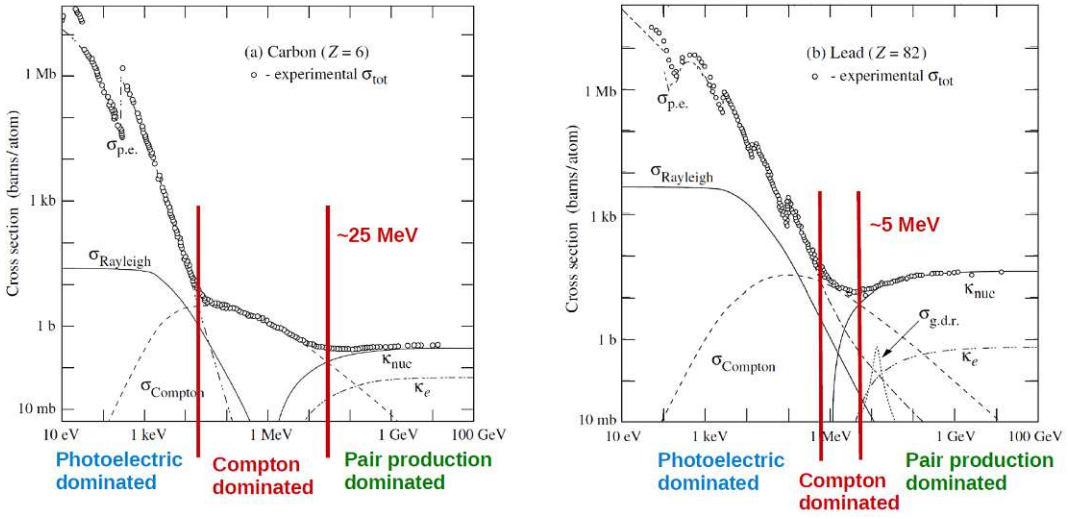

Fig. 2.5. Cross section of photon effects, comparing two different materials, on the left side a low Z material (carbon) and on the right side a high Z material (lead). The plots are taken from [59].

2.3.3 | Energy Loss in Matter

If a charged particle moves through a material, it loses energy. The energy loss originates from Coulomb interactions of the incoming particle with the field of the atomic electrons. This process, also known as electronic energy loss, dominates at lower energies up to tens of MeV for electrons and positrons and higher energies for heavier particles. The so-called radiative loss becomes the dominant process for particles with higher energies.[59]oc

When the incoming particle interacts with the nucleus of an atom, the particle does not lose as much energy but is mainly subject to an angular deflection. The corre-

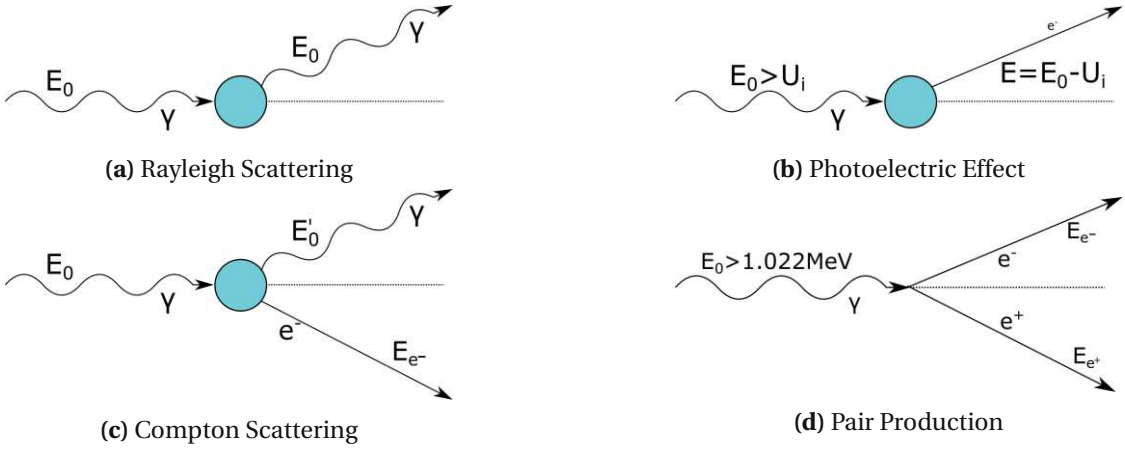

(a) Rayleigh Scattering

(b) Photoelectric Effect

(c) Compton Scattering

(d) Pair Production

Fig. 2.6. Electromagnetic Interactions. Plots taken from [61]

sponding energy loss is also known as Non-Ionising Energy Loss (NIEL), as the atom is not ionised but possibly displaced. A related quantity is the Displacement per Atom (DPA)[64], giving the fraction of displaced atoms. If the incoming particle exceeds the binding energy of the atom to the lattice, the atom can be removed from the original position and form a vacancy-interstitial atom pair (Frenkel pair[65]).

Coulomb Scattering

Coulomb scattering is the scattering between two point-like charges following the potential

$$V(R) = \frac{1}{4\pi\varepsilon_0}\frac{zZe^2}{R}, \tag{2.29}$$

with ε_0 being the permittivity, z and Z the charges between the interaction is happening, and e is the elementary charge. The charges can either be attractive or repulsive without impacting the cross-section.

The cross-section, also known as the Rutherford cross-section, can be described with

$$\frac{d\sigma_{\text{Ruth}}}{d\Omega} = \frac{z^2Z^2e^4}{4c^2\beta^2p^2\sin^4\left(\frac{\theta}{2}\right)}, \tag{2.30}$$

where $\beta = v/c$, θ is the scattering angle, and p the momentum. One of the most important takeaways from 2.30 is that forward scattering is much more likely backward scattering due to $\frac{d\sigma_{\text{Ruth}}}{d\Omega} \propto 1/\sin^4\left(\frac{\theta}{2}\right)$. Using the 4-momentum transfer, $q = 2p\sin\left(\frac{\theta}{2}\right)$, and the target recoil energy, $T = \frac{q^2}{2M}$, where M is the target mass, the cross-section can be transformed to,

$$\frac{d\sigma_{\text{Ruth}}}{dT} = \frac{2\pi z^2Z^2e^4}{\beta T^2 M}. \tag{2.31}$$

In Equation 2.31 it shows that $\frac{d\sigma_{\text{Ruth}}}{dT} \propto \frac{1}{T^2}$, which points to the fact that low energy transfers are much more likely than large energy transfers.[66]

As it was just seen, the interaction with atomic electrons dominates the energy loss of particles. Since it is impossible to track every incoming particle, and the particles act as an ensemble, energy loss is treated statistically.

The interaction of the projectiles with the atomic electrons dominates the energy loss of particles. The energy loss per unit path length $\frac{dE}{dx}|_{\text{elec}}$, also known as the **electronic stopping power**, is calculated using the differential cross-section,

$$\frac{dE}{dx}|_{\text{elec}} = N \int_0^{T_{max}} T \frac{d\sigma(T)}{dT} dT. \tag{2.32}$$

The electronic stopping power is calculated by integrating the probability of each energy transfer happening, $\frac{d\sigma}{dT}(T)$, times the energy, T, over all possible energy transfers up to T_{max} and multiplying it by the number of interactions N.

Coulomb interactions also occur between the incoming particle and the atomic nucleus, which leads to **nuclear stopping power**, which is dominant in low energy ranges (up to 100 keV/u) in the case of heavy projectiles. Contrary to the electronic energy loss, the atom is not ionised by this effect, which is why this type of energy loss is also known as non-ionising energy loss (NIEL). This effect is closely related to the displacement of atoms (DPA), which is discussed in greater detail later. For a lepton machine like FCC-ee, the effects of nuclear stopping are expected to be minor.

Energy loss of electrons

The average energy loss of heavy particles, $M >> m_e$, can be described with the Bethe-Bloch formula. However, this equation cannot be used for electrons and positrons, as the projectile and target have the same mass. This leads to larger deflection effects, and the onset of radiative losses happens at lower energies. At low energies, the electrons lose their energy mainly due to ionisation, meaning Coulomb interactions. Radiative losses dominate for higher energies, where Bremsstrahlung is the underlying process. It depends on the Z of the material where this transition happens. For low Z materials, radiative losses start to dominate above a few tens MeV, while for high Z materials, this threshold is below 10 MeV (see Fig. 2.7).

With the mass being the same for the incoming and target electron, the largest energy transfer possible between the two electrons is $T_{max} = T/2$. Considering quantum mechanics, it follows that the two electrons are indistinguishable after the interaction, meaning it is unknown which electron was the target and which was the projectile before. With these considerations, the average stopping power is described as

$$-\left\langle \frac{dE}{dx} \right\rangle = K \frac{Z}{A} \frac{1}{\beta^2} [ln\left(\frac{m_e c^2 \beta^2 \gamma^2 T}{2I^2}\right) - F(\gamma)], \tag{2.33}$$

with K being a constant, Z the atomic number of the impacted material, A the atomic mass of the impacted material, $\beta = v/c$, with v being the velocity of the incoming electron, I the mean excitation energy for the material and $F(\gamma)$ a correction function.[67]

Radiation Length

As just discussed, ionisation dominates lower energies, while Bremsstrahlung dominates the energy losses for higher energies. The energy, where the two contributions are equal, shown in Fig. 2.7, is the critical energy E_C. The higher the Z of the material, the lower the critical energy.

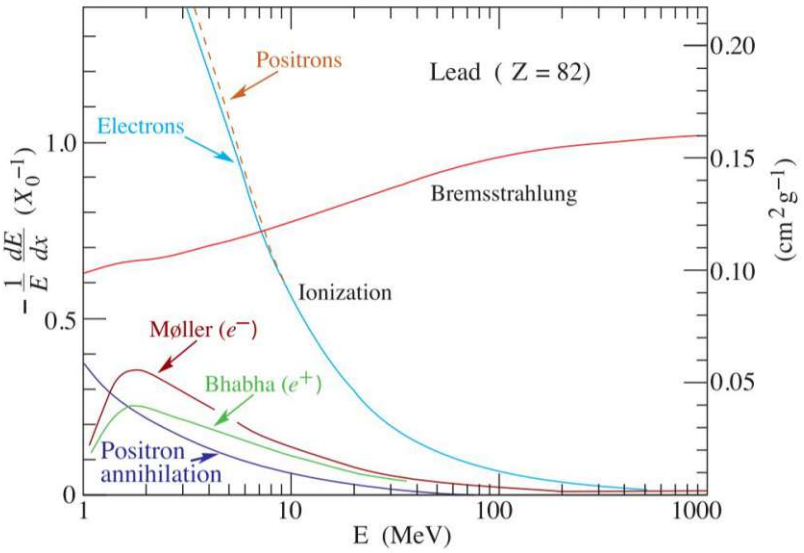

Fig. 2.7. Energy loss for electrons and positrons in lead. The plot is taken from [59].

In the region where radiative losses dominate, the energy loss is almost linearly proportional to the electron energy by a factor X_0^{-1}, the inverse radiation length, which can be then noted as

$$-\frac{dE}{dx} = \frac{E}{X_0}. \tag{2.34}$$

If this equation is solved for the average energy of the electrons, one finds

$$\langle E(x) \rangle = E_0 \cdot \exp\left(-\frac{x}{X_0}\right), \tag{2.35}$$

which means that the energy of the electron decreases exponentially with the distance travelled in the medium, with E_0 being the energy at $x = 0$. The radiation length is the length that is needed to reduce the energy of the electrons by $1/e$, which is a characteristic length and is different for every material. The higher the Z of the material, the

shorter the radiation length. For tungsten, the radiation length is 0.35 cm[68]. Generally the radiation length can be approximated with

$$X_0' = \frac{716.4\,\mathrm{g/cm^2}\,A}{Z(Z+1)\ln(287/\sqrt{Z})}, \tag{2.36}$$

where $X_0' = X_0\rho$ in g/cm^2, and Z and A are the atomic number and mass of the material.

The radiation length is the length over which an electron loses all but $\frac{1}{e}$ of its energy and can be approximated by using [69]

$$X_0' \approx \frac{716.4\mathrm{g/cm^2}\,A}{Z(Z+1)\ln(287/\sqrt{Z})} \tag{2.37}$$

with X_0' being $X_0\rho$ in g/cm^2. With the equation being an approximation, the experimental values from the PDG website [70] should be taken into account.

In Fig. 2.5, one can see that the cross-section for pair production is constant for high-energy photons. This cross-section can be brought into relation to the radiation length using

$$\sigma_{pair} \approx \frac{7}{9}\frac{A}{\rho N_A X_0}. \tag{2.38}$$

This means the shorter the radiation length, the larger the cross-section for the pair production. For this reason, high Z materials are usually the choice for targets as due to the larger cross-section a better positron yield can be achieved.

2.3.4 | Energy Deposition & Electromagnetic showers

When a particle loses energy moving through a volume, the energy loss is not necessarily equal to the amount of energy deposited in the same volume. This is due to the possibility of energy being carried away in so-called δ-rays, which are energetic. The actual energy deposition depends on several factors, like the beam energy, the beam size, the longitudinal and transversal distribution in the beam, and the impacted material.

The radiation length, X_0, is the characteristic feature of the impacted material in the case of a lepton machine. For analysing the effects, one has to distinguish between lower-energy particles in the MeV regime and higher energies, as the effects are changing.

If a MeV electron beam impacts a target, first, the energy deposition builds up and then forms a broad peak. If the Z of the material increases, the peak is more pronounced, which is formed by the Coulomb scattering of the electrons while they are decelerating. This process is followed by a contribution due to Bremsstrahlung photons, which is possibly still significant, depending on the energy and the material.

Contrarily, for a relatively heavy proton beam, a Bragg peak appears, which is much sharper, and the tail is less pronounced. More details can be found in the literature.

If the energy of the incoming beam is high enough, meaning from tens to hundreds of MeV, shower production is possible. In the case of impacting electrons and positrons, the main effect is the production of Bremsstrahlung, while impinging photons lead to pair production. In an electromagnetic shower, these effects happen in the form of a cascade, meaning photons produced by Bremsstrahlung will then undergo pair production. The newly produced electrons and positrons can undergo Bremsstrahlung again.

The particles decrease their energy from generation to generation. As soon as they go below the critical energy, E_c, radiative effects become less important, and ionisation effects dominate.

A simplified way to describe the shower development was described by Heitler [71] and uses the fact that the radiation length X_0 applies to Bremsstrahlung and pair production. After passing one radiation length, an interaction takes place, and one particle splits is replaced by two particles:

$$N(t) = 2^t, \tag{2.39}$$

where N is the number of particles and t the generation number, which also can be interpreted as the number of X_0. As discussed before, the energy decreases from generation to generation, which can be described with

$$E(t) = E_0/2^t, \tag{2.40}$$

where E_0 is the energy at the entrance of the material, which also defines the number of particles that will be produced. The shower maximum is reached as soon as $E(t) = E_c$, and after this, the shower decreases. Taking this condition into account, the generation of the maximum is

$$t_{max} \propto \log\left(\frac{E_0}{E_c}\right). \tag{2.41}$$

The radiation length is proportional to $A/(Z^2\rho)$, meaning the electromagnetic showers are shorter, the higher the atomic number and the higher the density of the material. Depending on the aim of the material put in place, high or low Z materials should be selected with care as their properties impact the energy deposition behaviour strongly. Generally, low Z materials are more robust as they absorb less power, leading to a milder and slower shower development. Similarly, these properties indicate that low Z materials are not suitable as absorbers and other protection elements.

Heitler provides a clear and simple model, but it cannot predict the situation accurately on a quantitative level. However, as this shower process is complex and it is impossible to solve this issue analytically, the best way is to use MC Codes such as FLUKA.

2.3.5 | Bremsstrahlung

This phenomenon is one of the crucial effects for both parts of this thesis, so it is discussed in more detail.

As the name says, Bremsstrahlung, breaking radiation, occurs if a charged particle, mainly electrons (or positrons), is decelerated in the Coulomb field of an atom. In this process, kinetic energy is is taken by the generation of a photon, while the impacting electron loses this energy. Depending on the Z of the material, this process is the dominant mechanism for energy loss of electrons and positrons in the range of MeV or a few tens of MeV. The cross-section of this effect is proportional to $\propto \frac{Z^2}{M^2}$, so this effect becomes more critical for high Z materials. Similarly, the effect is much smaller for a proton of the same energy as an electron, so this is why this effect is particularly important for lepton machines.[72]

In targets with high Z, this effect is used to produce high numbers of photons and further positrons. Less beneficially, Bremsstrahlung also happens for beam electrons interacting with residual gas molecules in the vacuum chamber, leading to energy deposition and possibly decreasing beam lifetime. These two applications are discussed in more detail in later chapters.

The cross section was first described by Bethe and Heitler in 1934 [73], which is corrected and extended for several physical effects, some in the original work, some several tens of years later. As the quantitative description of the cross-section is not necessary in the scope of this thesis, a qualitative description follows to give the reader an overview to the contributions.

The first effect corrected for is the screening by the electron cloud of the Coulomb field of the nucleus. It depends on the energy of the incoming electron if it feels the screening effect. If the electron enters at lower energies, there is hardly any screening, while for ultra-high relativistic particles, there is the full screening effect.

Secondly, there is not only the Coulomb field from the nucleus, but the electrons around the nucleus also provide a field. Therefore, also Bremsstrahlung happens between the incoming electron and the atomic electrons. After the calculations, it is evident that this effect only scales with Z and not Z^2.

The cross-section of Bethe and Heitler is based on perturbation theory, which assumes plane waves for the electrons, as it considers the Born approximation, which is valid as long as the energy is high enough. For lower energies, plane waves can no longer be assumed. Instead, Coulomb waves should be used, which is considered with the Coulomb correction.

As discussed previously, the power loss goes with $-\frac{dE}{dx} = \frac{E}{X_0}$, which then leads to the energy loss in the material depending on the distance as seen in Equation 2.35. However, this is the average energy loss, where the large fluctuations of the energy loss are not included, which are anyways not impacting the photons spectrum. The cross-section of the bremsstrahlung events is calculated in two parts, with specific selected cut energy, splitting high-energy and low-energy photons, as the energy loss scales differently for high- and low-energy photons.[72]

Beam Life Time Reduction due to Bremsstrahlung

As just discussed, the energy losses due to Bremsstrahlung fluctuate strongly and can also take away a large amount of the initial energy of the incoming electron in one interaction. This can be an issue for lepton colliders as these particles are more prone to such losses than protons, which are about a factor of 1000 heavier. These losses are caused by interactions with the residual gas in the vacuum chamber. If an electron of the beam undergoes a significant energy loss, the energy loss exceeds the energy acceptance of the machine, and the particle is lost. Therefore, it is crucial to calculate the probability of such events happening. In an accumulation of these events happening, the beam lifetime gets shorter. [56]

Taking the relative energy loss $\delta = dE/E_0$ into account, the probability of this event happening was derived by Bethe and Heitler. After some calculations, it follows that the probability for an energy loss of a particle per radiation length is larger than the energy acceptance with

$$P_{\text{rad}} = -\frac{4}{3}\ln\delta_{\text{acc}}. \tag{2.42}$$

The probability of a particle loss per unit time is proportional to the inverse of the beam lifetime. Therefore, the beam lifetime is composed of

$$\tau^{-1}_{\text{bremsstrahlung}} = -\frac{4}{3}c\sum_i \frac{1}{760}\frac{\tilde{P}_i}{L_{r,i}}\ln\delta_{\text{acc}}. \tag{2.43}$$

The sum is used to include the radiation lengths $L_{r,i}$ for several different gas species. As the radiation lengths are usually given for a pressure of 760 Torr, the residual partial gas pressure $\tilde{P}_i$ is given for each molecule type.

From Equation 2.43 is clear that the beam lifetime due to bremsstrahlung events only depends on the pressure of the vacuum and the machine's energy acceptance.

2.3.6 | Photonuclear Interactions

Energy deposition is mainly due to Coulomb interactions of charged particles. In the case of a lepton machine, the main contribution comes from the atomic interactions of electromagnetic particles. However, due to the severity of the effects of neutrons, photonuclear interactions must also be considered.

Neutrons are usually more abundant high energy hadron machines. However, with electrons of such high energies as in FCC-ee, secondary photons can lead to photonuclear interactions.

The incoming particles interacted with the atoms' Coulomb field in the previously discussed interactions. Now, the nucleus of the atom absorbs the photons directly, which can lead to the emission of nuclei. The photon energy threshold above which neutrons can be emitted depends on the neutron binding energy of the material. The energy range, where the photonuclear effect is especially large, is also known as Giant Dipole

Resonance[74]. In Fig. 2.5, the contribution can be seen for lead at around 10 MeV. A higher energy photon can emit more neutrons, but its probability is lower.

Neutrons are particularly interesting as they are the only 'stable' neutral hadrons with a mean lifetime of around 15 min. If a neutron with a few MeV is emitted, it is mainly slowed down by elastic scattering. If the neutron thermalises it is normally caught by a nucleus.

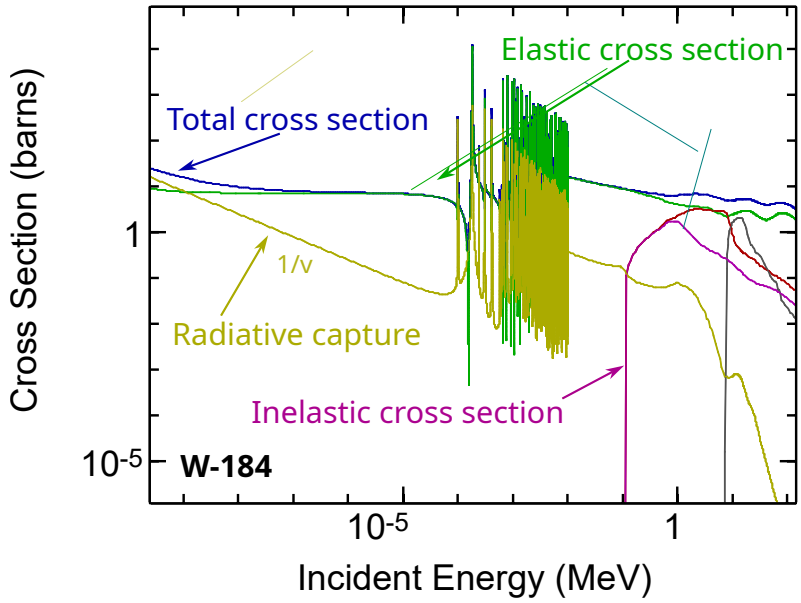

Fig. 2.8. Different cross sections of neutrons in tungsten (W-184). Plot produced with [75].

As shown in Fig. 2.8, the elastic cross section dominates over a wide energy range. The resonances are characteristic of every material due to the nuclear structure of different nuclei. Since tungsten is used widely in this project, the plot was generated for one of its isotopes.

For higher energies, inelastic scattering contributes to the cross-section. This happens above a certain threshold and contributes to the deceleration of the neutrons.

The radiative cross-section is inversely proportional to the neutron velocity below the resonance region, which means that the probability of absorbing a thermal neutron[5] is higher than a fast one. For heavier materials, it is likely that these neutrons also induce fission. The values for the neutron cross sections are usually measured and stored in databases, where the values can be read out.[75]

[5]Thermal neutrons are neutrons with an energy of 0.025 eV

2.4 Synchrotron Radiation

Synchrotron radiation (SR) is electromagnetic radiation emitted by a charged particle following a curved trajectory. SR is actively used in light sources, as the radiation provides high brilliance that can be used in a wide range of research[76]. In storage ring, SR is a parasitic effect and the resulting issues have to be mitigated.

The physical foundation for the description of SR was given with the Maxwell equations formulated in 1873, stating that moving charges lead to electromagnetic waves. The experimental demonstration followed in 1887 by Hertz. Later, Liénard and Wiechert [77] described the potentials of moving charges and the energy loss of relativistic charged particles following a circular path. [56]

After the theoretical description of SR, it took several years until the effect was seen experimentally in a machine. The first indirect confirmation was found in 1946 at the Great Energy 100 MeV betatron by Blewett[78], where the expected energy loss could be shown. Trying to directly detect SR failed in the first place, as the experiment was searching in the microwave regime. Finally, SR was directly observed at the Great Energy 70 MeV synchrotron[79] when it was understood that the SR is to be found at much shorter wavelengths.

One of the main issues of SR is the energy loss per turn of the beam, which a suitable RF system must replace. Depending on the size and energy of the machine, the beam loses energy up to the range of GeV/turn. The energy loss per turn heavily affects the design of the machine in terms of size and maximum achievable energy.

SR impacts several areas of the accelerator design. In beam dynamics, it leads to effects like radiation damping, affecting the design of the vacuum system, and quantum excitation. Close to the interaction points, SR substantially impacts the design of the Machine Detector Interface (MDI) region, as only a certain amount of background photons can be accepted[80]. The RF system design depends strongly on the SR energy loss per turn since it is responsible for restoring the lost energy. Finally, SR leads to gas desorption in the vacuum chamber, degrading the vacuum quality and leading to beam losses.

This thesis focuses on energy deposition in the FCC-ee arcs caused by SR. The energy loss per turn impacts the machine and the tunnel infrastructure, leading to radiation damage that must be well understood. The goal has been to develop feasible shielding solutions to reduce the impact of SR in the FCC-ee arcs.

2.4.1 | Basic Properties of Synchrotron Radiation

The phenomenon of synchrotron radiation is explained by electrodynamics, stating that an accelerated charge radiates electromagnetic waves. Liénard describes the emitted instantaneous power of a relativistic accelerated charge, whereas it does not matter if

the acceleration is in longitudinal or radial direction. However, as it is shown later, the radiation effect for a particle following a straight trajectory is much smaller than for a bent trajectory.

For a non-relativistic particle, the generated power is described by the Larmor formula [81],

$$P = \frac{e^2}{6\pi\varepsilon_0 m_0^2 c^3}\left(\frac{d\vec{p}}{dt}\right), \tag{2.44}$$

where ε_0 is the vacuum permittivity, c the speed of light, m_0 the rest mass of the particle and $\vec{p}$ the momentum.

Equation 2.44 is only valid for non-relativistic particles and therefore cannot be used in the case of FCC-ee, where the electrons are relativistic. This indicates that the Lorentz invariant form using $d\tau = \frac{1}{\gamma}dt$ has to be considered. The instantaneous power emitted in a machine with relativistic particles, hence considering the Lorentz invariant form, is

$$P = \frac{e^2 c}{6\pi\varepsilon_0}\frac{1}{(m_0c^2)^2}\left[\left(\frac{d\vec{p}}{d\tau}\right)^2 - \frac{1}{c^2}\left(\frac{dE}{d\tau}\right)^2\right]. \tag{2.45}$$

For a storage ring, where the energy of the particle does not change over time, $\left(\frac{dE}{d\tau}\right)^2$ disappears, and the power results in

$$P = \frac{e^2 c}{6\pi\varepsilon_0}\frac{1}{(m_0c^2)^2}\gamma^2\left(\frac{dp}{dt}\right)^2. \tag{2.46}$$

In a circular machine, the radiated power is proportional to γ^2 ($\gamma = \frac{E}{m_0c^2}$), while for linear machines, the power is proportional to $\frac{dE}{dx}$, which is orders of magnitude smaller.

Using $\frac{dp}{dt} = p\omega = p\frac{c}{\rho}$, Equation 2.46 simplifies to

$$P = \frac{e^2 c}{6\pi\varepsilon_0}\frac{1}{(m_0c^2)^4}\frac{E_b^4}{\rho^2}, \tag{2.47}$$

where E_b is the beam energy and ρ the bending radius.

From Equation 2.47 it becomes evident that the instantaneous power scales strongly with the beam energy and the mass of the particles. For lighter particles, the effect is much stronger, which explains the relevance of the topic for a lepton collider. The SR power can be decreased by using a larger circumference of the accelerator, which explains the large footprint of the FCC-ee machine.

However, for practical applications, the power loss per turn is more interesting, as this number indicates how much energy has to be replaced by the RF system. For this, the instantaneous power (Equation 2.47) has to be integrated over one turn,

$$U_0 = \oint dtP = \oint \frac{P}{\beta\gamma}ds = \frac{e^2}{3\varepsilon_0}\frac{1}{(m_0c^2)^4}\frac{E_b^4}{\rho}, \tag{2.48}$$

where it is assumed that all the dipoles along the ring have a similar bending radius ρ. In FCC-ee for the operation mode of 182.5 GeV, the energy loss per turn, U_0, is found at 9.2 GeV/turn for the CDR [24] parameters.

Another key property is the power the beam emits in the form of SR. Considering the beam current, I_b, the number of electrons in the ring, N_e, and the orbit time T_0, the beam power is calculated with

$$P_b = \frac{U_0 N_e}{T_0} = \frac{U_0 I_b}{e}. \tag{2.49}$$

In FCC-ee, this translates to 50 MW per beam for all four operation modes, which is a design choice [24]. The same beam power for all operation modes is achieved using a higher current for the operation with lower energies. The highest energy leads to the most challenging energy deposition conditions, which is explained by the SR spectrum discussed in the next section.

Equations 2.48 and 2.49 can be approximated for lepton machines with [82]

$$\begin{aligned} U_0[\text{keV}] &= 88.46 \frac{E^4[\text{GeV}]}{\rho[\text{m}]} \\ P_{\text{SR}}[\text{kW}] &= 88.46 \frac{E^4[\text{GeV}]\, I[\text{A}]}{\rho[\text{m}]}. \end{aligned} \tag{2.50}$$

Table 2.1 compares the characteristic numbers of different machines, showing the significant differences between hadron machines like LHC and lepton machines, like LEP or FCC-ee.The beam energy is several orders of magnitude larger in LHC, but due to the large mass of the protons the SR power significantly smaller. Regarding the lepton machines, a difference in radius shows strongly effects on the energy loss per turn and the critical energy, which is already described in Equation 2.48. The critical energy, E_c, is another characteristic property of SR, which is introduced in more detail in the next section.

	E **in GeV**	r **in m**	U_0 **in MeV**	I **in mA**	E_c **in keV**	P **in MW**
LEP	45.6	3026	126	0.32	70	0.4
	94.5	3026	2332	0.75	619	13.37
LHC	7000	2784	0.0069	0.85	0.045	0.0037
FCC-ee*	45.6	12240	39.1	1280	17.2	50
	80	12240	370	135	92.8	50
	120	12240	1869	26.7	313	50
	182.5	12240	10000	5.0	1101	50

Table 2.1. SR Parameters in various machines. *...The FCC-ee numbers are given for the updated 2023 version[32]. The values for LHC and LEP are taken from [83] and [84], respectively.

2.4.2 | Spectra of SR

So far, the energy loss and power of SR have been discussed, giving a first estimate of the impact on the machine and the tunnel. However, to comprehend the impact of the SR photons on the machines on a deeper level, it is necessary to understand the spectrum that defines how penetrating the photons concerning energy deposition are. A short introduction following [56, Part IX] and [85] is given now, but for diving deeper into the mathematics and theory behind, relevant literature is recommended.

Synchrotron light is emitted constantly all along the ring. For an observer located in one point, the synchrotron light appears periodically over time as a short flash (see Fig. 2.9).

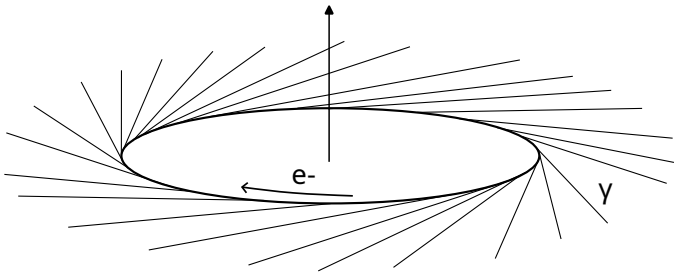

Fig. 2.9. Synchrotron light emitted along the ring. (Graphic similar to [56])

Synchrotron radiation is usually high in brightness and strongly focused due to the relativistic velocity of the particles. A non-relativistic particle emits radiation as well, however this follows a $\sin^2\theta$ distribution, where θ is the angle with respect to the acceleration axis (see Fig. 2.10). If the reference frame for the relativistic particle is moved from the lab system to the centre of mass system, the particle now is non-relativistic as well. In this reference frame, the radiation is the same as for a non-relativistic particle. However, in the lab system the radiation distribution for a relativistic particle is strongly forward-directed, with an opening angle of $1/\gamma$ per side (see Fig. 2.11). This means that the opening angle gets smaller for higher energy and lighter particles, which is the effect used in light sources.

Next, the SR spectrum has to be elaborated. The duration of the synchrotron light seen by an observer at one point has to be calculated, depending on the paths of the beam electron and SR photon (see Fig. 2.12). An electron travelling along the circular trajectory from A to B covers a distance of $2\rho/\gamma$. A photon is not bent, which leads to a distance of $2\rho\sin(1/\gamma)$. Considering that the photon moves straight with the speed of light, c, and the electron with βc, the length of the flash is found at

$$\begin{aligned}\delta t &= t_e - t_{ph} \\ &= \frac{2\rho}{\gamma\beta c} - \frac{2\rho}{c}\sin\frac{1}{\gamma}.\end{aligned} \tag{2.51}$$

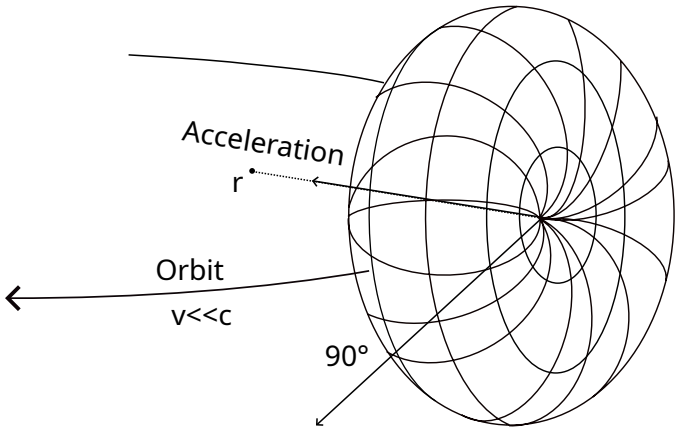

Fig. 2.10. Electromagnetic radiation from a non-relativistic particle in the lab system. In the centre of mass system of a relativistic particle, the particle sees a similar radiation pattern.

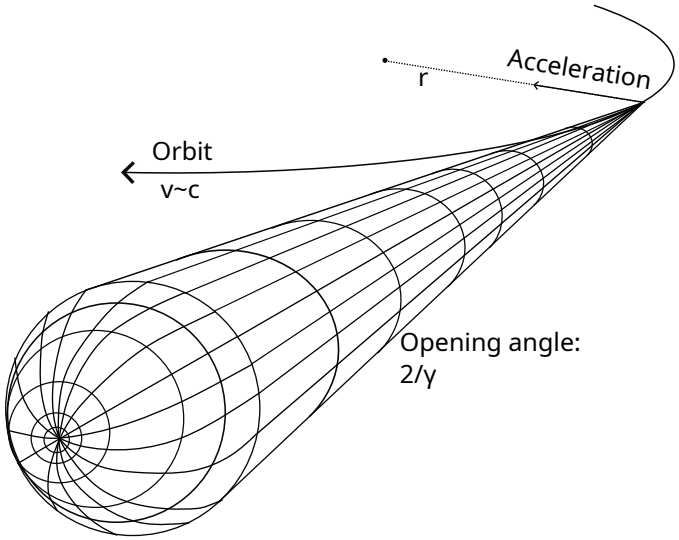

Fig. 2.11. Synchrotron radiation from a relativistic particle in the lab system.

For a more convenient expression, the sinus is expanded to the third order, $\sin\frac{1}{\gamma} \approx \frac{1}{\gamma} - \frac{1}{6\gamma^2} + O(\gamma^5)$. Furthermore, $\gamma >> 1$, so $\beta = \sqrt{1-\left(\frac{1}{\gamma}\right)^2}$ can be expanded to $\beta = 1 - \frac{1}{2\gamma^2} + O(\gamma^4)$. Using these expansions and $\beta \approx 1$, the light pulse duration results in

$$\delta t = \frac{4}{3}\frac{\rho}{c\gamma^3}. \tag{2.52}$$

The pulse duration is proportional to $1/\gamma^3$, so it becomes shorter with higher electron energy. The shorter peak in the time domain, the broader is the observed spectrum in the frequency domain.

For the effective pulse duration, per definition [56] only the half pulse duration should should be considered. Now, the critical photon frequency ω_c can be calculated,

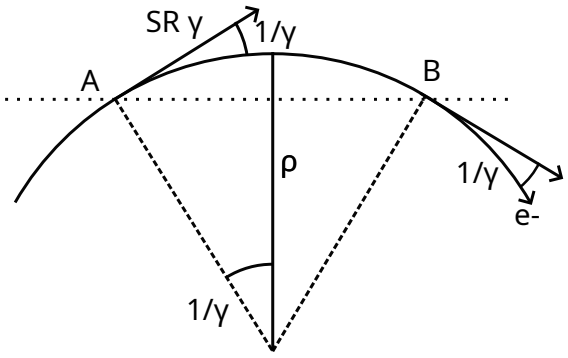

Fig. 2.12. Geometric scheme to understand the duration of the SR light flash.

which gives the upper end of the spectrum in the frequency domain,

$$\omega_c \approx \frac{1}{\frac{1}{2}\delta t} \approx \frac{3}{2} c \frac{\gamma^3}{\rho}. \tag{2.53}$$

Knowing the relation between frequency and energy, $\varepsilon_c = \hbar\omega_c$, the critical energy, ε_c, results in

$$\varepsilon_c = \frac{3\hbar c}{2(mc^2)^3} \frac{E^3}{\rho}. \tag{2.54}$$

The critical energy splits the SR spectrum into two parts of equal power. For energy deposition studies, this property is crucial, as it establishes how energetic the majority of particles are. As discussed in the previous section, different energy ranges are associated to different interaction mechanisms, which eventually lead to a different distribution of the deposited energy. The critical energy for electron machines can also be calculated by using [86]

$$\varepsilon_c[\text{keV}] = 2.2183 \frac{E^3[\text{GeV}^3]}{\rho[\text{m}]} = 0.66503 E^2[\text{GeV}^2] B[\text{T}]. \tag{2.55}$$

For FCC-ee, the critical energy[6] is found at 1.25 MeV for the $t\bar{t}$ operation mode at 182.5 GeV and at 0.019 MeV for the Z operation mode at 45.6 GeV, which shows that for higher energies much more energetic particles are emitted by SR. In Fig. 2.13, the spectra for the two energies at two different currents are plotted. For the same beam power but different beam energies and beam currents, the total radiation load on the machine is identical. However, the distribution of the power differs, as the energy range of the beam determines the dominant physical effects that occur in the scope of the interaction. For low beam energies, the power is absorbed mostly locally, while for high beam energies,

[6]The critical energies are given for the currents given in the FCC-ee CDR, which were used for the simulations in this thesis if not said otherwise.

effects like Compton scattering occur that results in a wider spread of power as particles can be back-scattered.

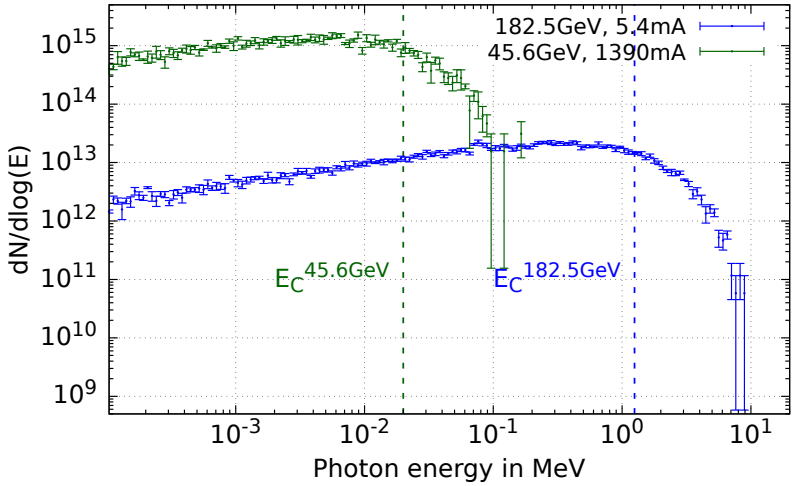

Fig. 2.13. SR spectrum for an electron beam of 182.5 GeV and 45.6 GeV, respectively. The plot is displayed using a double-logarithmic scale and normalised to the respective current.

The spectrum of SR in a circular accelerator comprises the harmonics of the revolution frequency ω_0 up to the critical frequency ω_c, and even beyond that.

It is worth remarking that the spectral distribution of the SR only depends on the critical energy, the radius of the machine and some added mathematical functions, and was found independently by Schwinger[87], and Sokolov and Ivanenko[88]. If the spectrum gets normalized to the critical frequency, it no longer depends on the energy and a universal distribution is observed, valid for any energy and machine size. As shown in Fig. 2.13, for low energies, the spectrum rises slowly, just up to the critical energy and beyond that, it decreases exponentially.

3

Third Chapter

Methods and Tools

This chapter discusses the background and application of Monte Carlo Simulations. Subsequently, FLUKA, Flair, and Linebuilder, the tools used for this thesis, are presented. This part finishes with a discussion of the scored quantities and their relevance for the machine.

3.1 Monte Carlo Simulations

In accelerators, highly energetic particles lead to a hostile radiation environment that must be considered for the tunnel and the accelerator component design. Monte-Carlo-based radiation transport simulations are used to gauge the severity of the impact present in different locations. These simulations allow for mitigating possible issues over several iterations while improving the layout and reducing the impact on the machine and its environment.

A core part of the radiation transport problem is the radiation source, which can take various forms and shapes. The reasons for radiation in an accelerator are manifold, ranging from physical effects like synchrotron radiation to interaction with residual gas molecules and beam impact on targets, to name a few. The particles constituting the radiation are various: photons, leptons, hadrons, and heavy ions. For FCC-ee, especially electromagnetic particles in an energy range from keV to GeV are concerned, including electrons, positrons, and photons. For neutrons that are also present in the machine in small fractions, the lower end of the energy range is given by the thermal neutrons (0.025 eV at 300 K).[89]

The radiation source interacts with the matter of the implemented geometry. Combinatorial geometry uses different bodies, like planes, spheres, cones, and cylinders. These bodies are the baseline for defining regions with an assigned material, which can be pure or compound. Furthermore, magnetic or electric fields can be present, which can heavily

influence the behaviour of charged particles.

The particles of the radiation source undergo interactions with the matter they are propagating in. In this process, secondary particles can be produced, as well as full particle showers. Accurate results are obtained by considering the various interaction probabilities and describing the interaction outcome employing suitable models and data.

Finally, the produced radiation has to be quantified. In experiments, different quantities can be measured. The equivalent for simulations is the so-called scoring that allows estimating them. Depending on the problem, the scoring can deliver spectra, deposited energy, quantities related to material damage, biological effects and activation of materials.

As discussed in the previous chapter, particle-matter interactions include different processes, such as angular deflections of the incoming particle, displacement of atoms, and ionisation, which results in energy loss and eventually in energy deposition.

So far, the radiation transport problem has been discussed qualitatively. Now, an introduction to the quantitative solution of this problem is given [90]. An ensemble of particles, which possibly consists of different particle species, at a position $\mathbf{r}$, moving with the energy of E, along the direction of $\Omega = (\theta, \phi)$[1], is known as the radiation field. The transport equation aims to describe the change of the radiation field at a later time within a small volume V, which has a surface S. Another required quantity is the particle density at the radiation source, $n_0(\mathbf{r}, E, \Omega, t = 0)$. In equation 3.1, Ω'' denotes a direction so that the scattering angles Ω' bring it eventually to Ω, and N is the target atom density.

The transport equation is written as,

$$\begin{aligned}\int_V \mathrm{d}\mathbf{r} \frac{\partial n_i(\mathbf{r}, E, \Omega, t)}{\partial t} = &- \oint_S \mathrm{d}A \mathbf{j}(\mathbf{r}, E, \Omega, t) \cdot \hat{\mathbf{a}} \\ &- N \int_V \mathrm{d}\mathbf{r} n_i(\mathbf{r}, E, \Omega, t) v(E) \sigma(E) \\ &+ N \int_V \mathrm{d}\mathbf{r} \int \mathrm{d}E' \int \mathrm{d}\Omega' n_i(\mathbf{r}, E', \Omega', t) v(E') \frac{\mathrm{d}\sigma}{\mathrm{d}\Omega'' \mathrm{d}E''} \\ &+ N \int_V \mathrm{d}\mathbf{r} \int \mathrm{d}E' \int \mathrm{d}\Omega' \sum_j n_j(\mathbf{r}, E', \Omega', t) v(E') \frac{\mathrm{d}\sigma_{\mathrm{sec},i}}{\mathrm{d}\Omega'' \mathrm{d}E''} \\ &+ \int_V \mathrm{d}\mathbf{r} Q_{\mathrm{source}}(\mathbf{r}, E, \Omega, t).\end{aligned} \tag{3.1}$$

The change in the radiation field is a sum of several contributions. The first term describes the particles moving through the volume without being scattered. The following two terms express the number of particles scattered out of and into the volume. The second to last line considers the contribution from secondaries due to interaction events. The last term describes the source particles already in the volume before any interaction.

[1] θ and ϕ are the polar and the azimuthal angle.

Equation 3.1 can be solved for any arbitrary source density and geometry as long as realistic cross-sections are considered. However, an analytic solution of this integro-differential equation is only possible in a few specific cases, including cases with an infinite medium, only one particle species or taking only a few interaction mechanisms into account.

Therefore, this problem must be tackled numerically, where the Monte Carlo method is well-suited. Another method is the numerical quadrature integration, which can solve general cases but is relatively inefficient. The stochastic Monte Carlo method can solve the transport equation for any geometry and radiation field while being efficient. The knowledge of the cross-sections of the interactions allows the simulation of the ensemble of particle histories. The more refined the cross-sections are, the higher the reliability of the results. The particle tracks are accumulated to achieve good statistics, allowing for reliable physical observable predictions.[90]

Simulating radiation transport based on the Monte Carlo method was developed in the 1940s as part of the Manhattan Project[91]. While the method gets its name from the casinos in Monte Carlo, the main project drivers were Nicholas Metropolis, Stanislaw Ulam[92], Richard Feynman, Richard von Neumann, and Enrico Fermi[93].

The Monte Carlo method benefits from the Central Limit Theorem, which states that for a large number of random trials, N, the mean of the Gaussian distribution will move towards the actual expectation value, with the standard variation evaluations decreasing as $\propto 1/\sqrt{N}$. Therefore, reducing the error bars by a factor of 10 requires an increase of the trials by two orders of magnitude.

In radiation load studies, the Monte Carlo (MC) method solves the radiation transport equation by calculating the particle tracks and the following energy deposition numerically. As long as the cross sections of the microscopic events are well known, in this case, mainly electromagnetic effects, like bremsstrahlung, Compton scattering, SR, and pair production, the Monte Carlo method delivers reliable results for the macroscopic effects.

3.2 FLUKA

FLUKA [94, 95, 96] is one of several particle tracking codes, next to Geant4[97], MCNP[98], MARS[99], PHITS[100] and Penelope[101], to name a few of them. The capabilities of this tool cover a vast amount of physical effects and can be applied in a wide range of fields. This thesis focuses on lepton beams in the energy range of several hundreds of GeV in a large accelerator complex and how to mitigate possibly destructive effects.

In FLUKA, photon interactions are calculated down to 100 eV and electron and positron interactions down to 1 keV. Neutrons are tracked to the meV range, which is necessary

due to the large cross-section of thermal neutrons. While these are the relevant particles for this thesis, FLUKA offers a much wider range of interactions not discussed here.

The microscopic interactions lead to macroscopic effects, which are calculated in FLUKA. The consequences of radiation include heating, thermal shock, quenching, material deterioration, oxidation, and shielding requirements. The code can also be used in medical physics or for radioprotection, where the activation of materials and the impact on the environment and users is investigated. Energy deposition translates into power density, total power, and dose, while other quantities like DPA and particle and dose equivalent fluences can be calculated.

However, there are some limitations to MC codes like FLUKA. First, the simulated medium is assumed to be amorphous and isotropic. Furthermore, the material is not affected by the previous particles, which means that organic insulators do not change their physical properties even though they would in reality if the total dose has been too high. In reality, particles produced in showers possibly interact with each other. This effect, assumed to be negligible, is not considered in FLUKA, as the particles only interact with the medium.

Furthermore, the next step of a particle does not depend on the previous one, which means that it is a Markovian process.

The code is historically based on Fortran, using different input files and input cards. For a better user experience, a graphic user interface, Flair, is used, which is discussed in more detail in the next section.

3.2.1 | Simulation Ingredients

Several inputs are mandatory for launching a FLUKA simulation, and more options can be added for more elaborate simulations.

In every case, it is necessary to provide a particle source, such as a beam or a particle distribution. A beam is the simplest solution, where the particle type, the energy, the energy spread, the divergence and spatial distribution need to be provided. Additionally, the beam position has to be given, indicating the origin and the direction, which can be done in Flair[102], so no Fortran coding is necessary. If a particle distribution should be used as a source, a designated user routine written in Fortran has to be implemented.

The main task before launching a simulation is often to implement the geometry. In FLUKA, a combinatorial geometry has to be implemented, meaning logical operations are defined between bodies. The bodies vary from infinite planes, RPPs (Rectangular ParallelePiped), spheres, cylinders, and cones. A boolean geometry is preferred over a CAD geometry as it provides higher precision. These bodies then form zones, which get embedded in so-called regions. The regions have the appropriate material assigned, which can be pure or compound. It is important to note that every point in the geometry world has to be assigned to one and only one region, as it otherwise leads to errors. If present, a magnetic field must also be added to the geometry to represent the real conditions.

The equivalent of a measurement at an experiment is the scoring in a simulation. Scoring can be performed on a region basis or in an independent Cartesian or cylindrical mesh, to name a few. The mesh size of the scoring has to be thoroughly thought through, as smaller meshes require more computing time and lead to more significant statistical errors. For a coarse mesh, the seen value will approach the true value quicker, and the statistical errors will be smaller, but no fine resolution is given. So, for a general overview of a large geometry, a large mesh is most likely sufficient, while for understanding the impact on detailed components, a mesh in the range of millimetres is required. Other types of scoring exist as well, where, for example, the amount of particles moving through a boundary is registered. With all those types of scoring options, it is possible to measure all kinds of quantities, like total power, power density, flux, dose, and DPA, to name some relevant ones in this thesis.

There are some cases where the expectation value converges slower than desired due to various issues. These issues could range from scarce amounts of secondaries in a region to too little of a particular particle type. If this is happening, adding some biasing to the simulation is necessary. Biasing exists in several types and is powerful. However, the user has to be careful not to trigger un-physical changes that might appear in the results.

All the information above is merged into one input file, a text file that adheres to columns as needed for Fortran to read the file correctly. The simulation can be launched after producing the executable file, possibly embedding different user routines. The simulations are usually run in sequences called cycles. Each of the cycles has the same amount of primaries. The cycles run in series, but it is possible to launch several jobs in parallel to reduce the runtime of the simulation. The measure to gauge the run time of a simulation is usually the average CPU time per primary, which decides how long it takes to run an extensive simulation as a function of the total number of primary histories required by the desired scoring.

3.3 FLAIR

Flair[102] is a graphical interface based on `python3` to facilitate using FLUKA. It allows the user to work on an intermediate level, where the user still sees how the input information is translated into the FLUKA input card.

One of the core elements of Flair is the geometry editor (see Fig. 3.1), which enables a more intuitive way of building geometries where the geometry is visible from different angles and in 3D. Furthermore, using this editor makes it easier to debug the geometry in case of errors.

The other main benefit of using Flair is the input file editor that allows a simple way of adding information to the input cards without worrying about the correct formatting of the input file (see Fig. 3.2). Possible errors will be spotted and remarked on, which makes debugging much more straightforward. As mentioned above, when one card is

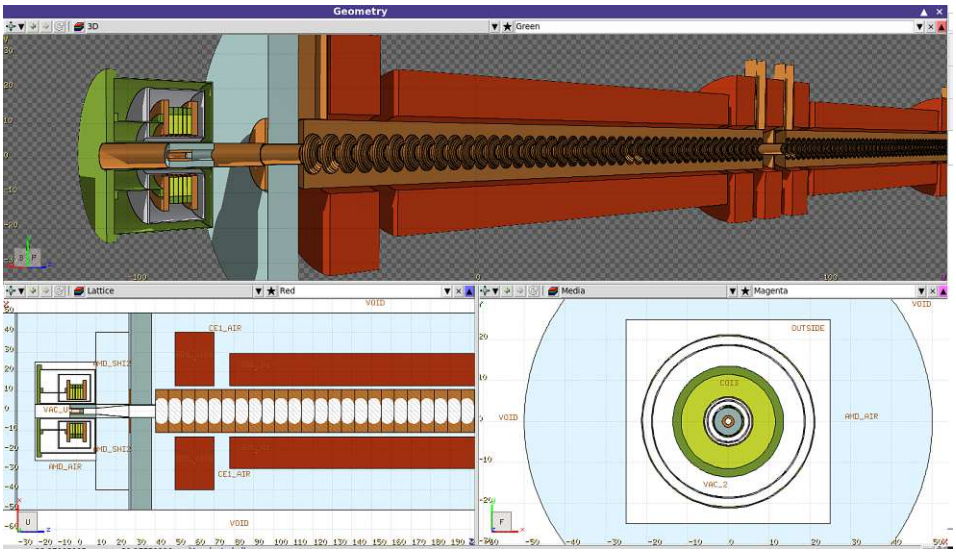

Fig. 3.1. Geometry editor in Flair, displaying the FCC positron source in 3D (top), side cut (bottom left) and the cross-section (bottom right).

selected in Flair, its FLUKA counterpart is displayed at another place on the screen, so the user sees what is happening from the FLUKA perspective.

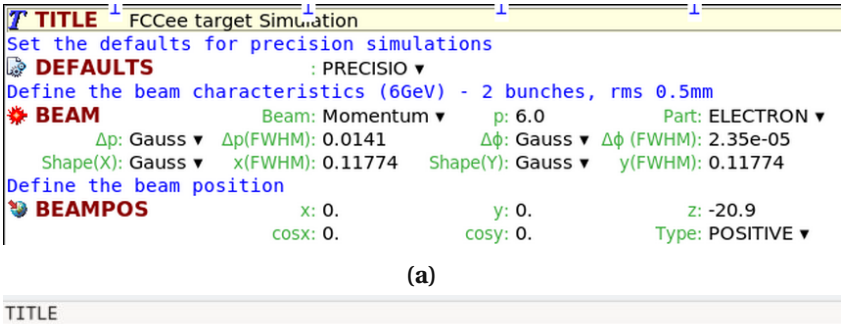

(a)

```
TITLE
FCCee target Simulation
* Set the defaults for precision simulations
DEFAULTS                                                        PRECISIO
* Define the beam characteristics (6GeV) - 2 bunches, rms 0.5mm
BEAM            6.0   -0.0141 -2.35E-05  -0.11774  -0.11774          ELECTRON
* Define the beam position
BEAMPOS          0.        0.     -20.9        0.        0.
```

(b)

Fig. 3.2. Input card in (a) Flair and (b) directly in FLUKA.

Another benefit is the possibility of compiling the executable and launching simulations directly from Flair, where the simulation status can be observed. After a successful simulation run, post-processing is possible within Flair, where scoring output files are merged. One final helpful tool in Flair is directly generating plots from the output file with the underlying geometry. The plotting tool is based on `gnuplot` [103]. However,

the user can still manipulate and plot the data in any other framework.

3.4 Line Builder

If the simulation setups get too complex because full beamlines over several hundreds of meters should be simulated, setting up the simulation, even in Flair, is tedious and error-prone. Line Builder (LB) [104] was developed to facilitate this task. It is a `Python` program that supports the user to build the beamlines in a more automatised way.

One of the core elements of the LB is the so-called `fedb` (FLUKA Element Data Base), where the different FLUKA models of the magnets and other components are stored. Each geometry is saved and split into three files containing the bodies, regions and assigned materials, respectively. This database should be kept updated so that any user can access it.

LB builds the line by placing the magnets according to the provided Twiss file. Usually, those Twiss files are produced with MadX[105] and are received from the beam optics group. The information about the magnetic strength in the Twiss file is translated by the LB into the actual magnetic field value, which can also be used to re-normalise and input map.

Other information eventually found in the input file, like the physics settings or biasing, is prepared in a folder called `customised files`, with a file for each type of information. One of the main files is the file that lists all the required elements from the `fedb` that are included in the beamline. This file also defines the scoring that is associated to each element. For additional general scoring in the `customised files`. Another essential ingredient in this folder is the input file for the tunnel geometry and the beam pipe interconnects between the elements. Depending on the problem, a 2D tunnel section can be created, which is then bent by the LB according to the Twiss file. For parts of the accelerator, where the tunnel section changes along with the longitudinal direction, like for interaction regions, a 3D tunnel with the exact length is used.

Finally, there is the LB input card that is a text file, where the fundamental information is saved. This includes the particle type, energy, the Twiss file path, and the names of the additional user routines that should be included.

LB is then called in a command line, and the final FLUKA input file is created, as it is otherwise assembled in Flair. Building the executable with LB that automatically includes all the selected user routines is also possible.

3.5 User Routines

More custom tasks are not possible to perform directly with Flair. For this, it is necessary to include user routines that need some Fortran code implementation for specific

needs.

In this thesis, user routines are applied in several cases for various simulations. First, a routine called `mgdraw_exbkg.f` [106] is used for the positron production source simulations, which dumps particles as soon as they enter a dedicated region. These particles and their properties, like particle type, energy, location, and angle, are saved into an ASCII file and can be analysed. This information allows to understand the constituents and the origins of the energy deposition later on on a deeper level.

In the studies of the SR in the FCC-ee arcs, the `usrmed.f` [107] routine has been employed. In the arcs, the FODO cells occur periodically, only one half cell has to be implemented if this routine is used. As soon as the particles reach the end of the cell, they enter into a dedicated material, which activates the user routine. In this simulation, gold is chosen as it is not present elsewhere in the beamline. The routine retrieves the information about the particles energy, location and angle. On the latter two a translation and rotation is applied, so they are correctly reinserted at the beginning of the line. The energy is retrieved, as only secondaries should be reinserted but no primaries, to simulate the SR effects of the beam moving through a half cell. The use of the `usrmed.f` routine enables a clean and efficient way of simulating the SR impacts in the FCC-ee arcs.

3.6 Radiation Consequences: Scored Quantities

The radiation effects on the material are distinguished between instantaneous and long-term effects. Generally speaking, these effects impact the material negatively and should be held to a possible minimum. The components in the machine react differently on the radiation impact, depending on the materials and the operating temperature. A machine operated with superconducting devices has other restrictions than a machine operated at room temperature. With the experience that has been gained over the past decades, it is possible to assess if the radiation load is sustainable on components or not.

It shall be noted that this thesis does not cover simulations for assessing the activation of material or of the environment, as these are done by the Radiation Protection (RP) group. Generally, in the FCC-ee arcs, the activation of material is expected to be low, as it is caused by photons in the energy range of the Giant Dipole Resonance[74], which is higher than the SR photon energy.

First, the instantaneous effects are discussed, emphasising the general meaning and the further implications for this thesis.

3.6.1 | Instantaneous: Heat Load

The heat load is usually the first quantity to be investigated when simulation results are available. It is given per machine component and is usually measured in W. Depending on the beam power, size, location, and component type, the absorbed power can vary from a few mW to several hundred kW. The heat load or absorbed power per component is essential and helpful as the power distribution on the whole setup is assessed.

The heat load is also used to design the cooling of the components if necessary. However, it does not indicate the power distribution in the components, which has to be evaluated by the power density.[59]

For obtaining the heat load data in FLUKA, a scoring per region of the power is available. After transforming the binary file into an ASCII file, the can be manipulated by the `PowerByRegion.py` script. This script provides a table of all the absorbed power and the statistical error for each component with the applied normalisation.

3.6.2 | Instantaneous: Power Density

The absorbed power shows how much power goes onto one region or component but does not show the power distribution. The power density in W/cm^3 is calculated for this and is crucial for the design of the machine and its elements. First, it has to be understood why and how power density is deposited in the material.

If the power density rises above kW/cm^3 for even a very short time, this can lead to the melting of the material, ultimately destroying a component. After such an event, the machine possibly requires a downtime of several months as it has to be repaired and prepared again. A failure like this usually happens for fast beam losses, where the beam

impacts the beam pipe instead of a beam dump.

If the machine is operated at low temperatures, meaning in a superconducting state, there is the risk of quenching the superconducting magnets. In a quench, the superconductivity of a magnet is lost, changing it back into a normal conducting device, as soon as the critical temperature ha been exceeded. Eventually, this leads to downtime of the machine for several hours as the magnets have to be cooled down again after a quench. In an accelerator like LHC, quenching can be critical, as the magnets are connected in series, so if one magnet quenches, this phenomenon is transmitted to the neighbouring dipoles as well.[108]

For low-temperature superconductors that are operated at liquid helium temperature, a quench limit of the order of $10\,\mathrm{mW/cm^3}$ applies[108]. This threshold is likely much higher for more modern superconductors, like high-temperature superconductors (HTS), which can be operated at temperatures of liquid nitrogen. Precise numbers have to be still determined.

Generally speaking, if a large gradient in power density is observed in a component, it is usually easier to cool, and locally higher values are more likely acceptable. On the other hand, mechanical stresses have to be evaluated.

This quantity is technically assessed in FLUKA using the `USRBIN` card to score energy density maps. Depending on the structure of the geometry, either a cylindrical or a Cartesian mesh is selected. The mesh size should be according to the needed resolution but not too fine, as this leads to poor statistics and high computational efforts. In FLUKA, the scored quantity has the units of $\mathrm{GeV/cm^3pp}$ (per primary), meaning that for obtaining a power density, one has to apply a normalisation factor that takes the current setup into account.

3.6.3 | Long term: Ionising Dose

Long-term effects impact the components of an accelerator cumulatively. One of the relevant quantities is the ionising dose[2], which is measured in Grey, Gy, with the units of J/kg.

If dose levels are too high, the material becomes brittle and starts to degrade. The change in structure leads to a change of material properties that is destructive. The electronics installed in the tunnel and organic materials used as insulators are particularly vulnerable to high levels of ionising dose. Organic materials, like epoxy, resin, and G11, are used as insulators in coils. The incoming radiation produces free radicals in the insulator. These free radicals undergo different reactions, ranging from cross-linking to gas to oxidation, significantly accelerating the degradation. These chemical reactions change the molecular structure, which eventually results in a change in the macroscopic structure and its properties. Doping the material with certain additives can lead to a beneficial increase in the dose resistance of the material. However, if high dose levels are expected, organic materials should be avoided.[108]

[2]Dose is different from activation and should not be confused.

The other critical parts in the machine regarding dose are the electronic components. In R2E (Radiation to Electronics) terms, the Total Ionising Dose (TID) induces cumulative effects that add up over time. The effects are relatively similar to what happens in organic materials. Generally, a charge builds up in oxides, leading to a shift of the thresholds and an increased leakage current, ultimately destroying the components.

Depending on the part of the machine one is looking at, different thresholds for a tolerable dose are observed. For superconducting magnets with organic material as insulators, the typical threshold is assumed to be at 30 MGy[109, 108], and then they must be replaced. In the case of HTS materials, this threshold still needs to be clarified. For R2E, the thresholds usually are far below, at a few Gray[110].

3.6.4 | Long term: Displacements per Atom (DPA)

Another long-term effect impacting the machine is related to the displacements of atoms. Contrary to the ionising dose, the DPA mainly refer to inorganic material. Due to the underlying physical mechanism, DPA are usually higher in the case of hadron beams as leptons are lighter and have no strong interaction, which makes displacement less likely. Nevertheless, electron beams can lead to relatively high DPA values if the energy and beam intensity is high enough.

On a macroscopic level, high DPA levels lead to swelling of material. In parts where a precise geometry is necessary, like in RF cavities, DPA can impact the behaviour of such components. Otherwise, swelling can also be problematic in space-restricted places.

These effects are caused by processes at the atomic level. The DPA are a dimensionless number proportional to the number of Frenkel pairs[65] (see Fig. 3.3), N_F, in a material. It is given as[64]

$$\mathrm{DPA} = \frac{A}{V N_A \rho} N_F \tag{3.2}$$

with A being the molar mass in g/mol, V the volume in cm^3, N_A the Avogadro number in mol^{-1} and ρ the mass density in g/cm^3. As it is a dimensionless number, it tells the average fraction of atoms that are displaced, so 0.3 DPA means that 3 out of 10 atoms are displaced. In reality, acceptable values are in the range of 1×10^{-5} DPA/year to 1×10^{-3} DPA/year.

If a recoil with an energy E_a, i.e. the primary knock-on atom (PKA), hits an atom in the lattice, and its energy is higher than the displacement energy E_d, the atom will be displaced and form a vacancy at its former location and end up as an interstitial atom somewhere else in the lattice. The combination of the interstitial atom and the vacancy is also known as a Frenkel pair. The DPA is a calculated value, usually using empirical formulas. The first ones to mathematically describe this phenomenon were Kinchin and Pease (1955)[111] with this simple step function,

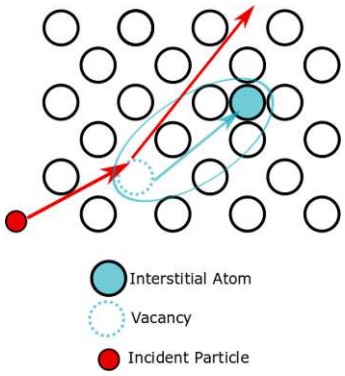

Fig. 3.3. Visualisation of a Frenkel pair. (Figure taken from [61])

$$N(E_a) = \begin{cases} 0 & E_a < E_d \\ 1 & E_d < E_a \leq 2E_d. \end{cases} \tag{3.3}$$

This means that if the energy of the PKA, E_a, is lower than the displacement energy E_d, the number of Frenkel pairs $N(E_a)$ stays 0. If the energy exceeds the displacement energy, a Frenkel pair is generated. There is an upper limit of $2E_d$ since more than one Frenkel pair would be produced if the energy was higher than that value.

By performing BCA (Binary Collision Approximation) simulations, Norgett, Robinson, and Torrens, found a way to describe the physical reality more accurately in 1974[112, 113],

$$N(E_a) = \begin{cases} 0 & E_a < E_d \\ 1 & E_d < E_a < \frac{2E_d}{0.8} \\ \frac{0.8E_a}{2E_d} & E_a > \frac{2E_d}{0.8}. \end{cases} \tag{3.4}$$

The model described in equation 3.4 is also known as DPA-NRT. The factor of 0.8 was obtained by the BCA simulations, which is a factor that describes the displacement efficiency. Differently to the initial description, the displacement energy now also takes into account that a fraction of the energy of the PKA is transferred to the atomic motion, $E_a = E_{\mathrm{PKA}} \times f(E_{\mathrm{PKA}})$. This model is the most used one in radiation damage simulations nowadays. However, it strongly overestimates the actual DPA. The root of the cause is found in the fact that this type of DPA calculation does not take the recombination in cascades into account. In reality, some Frenkel pairs in cascades move back into a correct lattice position, decreasing the number of vacancies.

In 2018 a new model was developed by Nordlund et al.[114], known as Athermal Recombination Corrected DPA (ARC-DPA). Generally, the description,

$$N(E_a) = \begin{cases} 0 & E_a < E_d \\ 1 & E_d < E_a < \frac{2E_d}{0.8} \\ \frac{0.8E_a}{2E_d}\xi(E_d) & E_a > \frac{2E_d}{0.8}, \end{cases} \tag{3.5}$$

looks quite similar to the one for the DPA-NRT, except for a weighting function $\xi(E_d)$. This function gives the relative damage efficiency, meaning the ratio between the actual number of Frenkel pairs and the number of Frenkel pairs calculated by the DPA-NRT model, which after some consideration, gives

$$\xi(E_d) = \frac{1 - c_{\text{arcdpa}}}{(2E_d/0.8)^{b_{\text{arcdpa}}}} E_d^{b_{\text{arcdpa}}} + c_{\text{arcdpa}}. \tag{3.6}$$

The two constants b_{arcdpa} and c_{arcdpa} are either experimentally found or with the help of molecular dynamic (MD) simulations. The advantage of this type of DPA calculation is that it is considerably the most accurate description. However, these coefficients have to be obtained for every material, and often, it is not possible to get an accurate result if a particular, not-so-common material is considered.

The three types of DPA calculation were discussed in detail as the latter two were implemented into FLUKA recently. Over the course of the thesis, studies were performed to understand the differences and gauge the results.

3.6.5 | Long term: Equivalent Fluence Values

In electronics[115, 116], there is a differentiation between cumulative damage and single-event effects (SEE). As the name says, the cumulative effect can lead to a reduced equipment lifetime over time, while SEEs are of stochastic nature and can happen at any time of the operation.

In the case of cumulative effects, ionising and non-ionising effects are distinguished. The ionisation effect, induced by the Total Ionising Dose (TID), was discussed beforehand.

The non-ionising energy losses (NIEL) lead to displacement damage in materials. In the subject of R2E, this quantity is measured by the Silicon 1 MeV neutron equivalent fluence (Si-1MeVN-eq), which is given in cm^{-2}. Depending on the neutron production threshold of the material, this quantity is often dominated by neutrons in the case of high Z materials and dominated by electromagnetic particles for low Z materials.

The other type of effects, SEEs, are stochastic, caused by a single particle impacting a small sensitive volume. The underlying physical effect is either direct or indirect ionisation of the volume. The first mechanism is based on high Linear Energy Transfer (LET), which is associated to heavy ions, which are scarce in a machine like LHC during proton operation. More likely to happen is indirect ionisation, where a nuclear interaction leads to high-LET secondaries. For the latter case, two different quantities are investigated.

These two fluences, both measured in cm^{-2}, are, on the one hand, the High Energy Hadron equivalent fluence (HEH-eq) and, on the other end of the energy scale, the Thermal Neutron equivalent fluence (TheN-eq). High energy hadrons (>20 MeV), which also include neutrons, lead to soft and destructive SEEs through nuclear reactions. For hadrons between 0.2 MeV-20 MeV, a weight function is applied that makes their effect

much smaller. This contribution is expected to be small for a machine like FCC-ee, where high-energy neutrons are scarce.

Thermal neutrons have an energy of around 0.025 eV at room temperature (300 K). Neutrons in this energy range lead to soft SEEs, for example, single-bit flips that lead to a wrong output. Typically, their effect is mediated through a $^{10}B(n,\alpha)$ reaction. This type of radiation usually can be easily shielded with a layer of boron to catch the neutrons outside the electronic component. The thermal neutron equivalent fluence is more relevant with the inverse of the particle velocity, weighing the contribution of higher energy neutrons. Therefore, it is more relevant in a machine like FCC-ee.

Even though this thesis is not a thesis on R2E, it is crucial to assess the R2E levels in the machine to understand where more investigations and optimisation must be done.

4

Fourth Chapter

Positron Production Source

In a lepton collider like FCC-ee, the production of positrons plays a crucial role. One of the design options for the positron production source of this machine features a superconducting solenoid made of high-temperature superconductor coils (HTS) as an adiabatic matching device (AMD). The AMD performs a phase space rotation of the positrons produced in the target before they are accelerated in the capture and positron linac. The superconducting coils allow for a higher magnetic field strength, which improves the positron yield. The considered target is made out of tungsten, which generates a significant electromagnetic shower, possibly implying an unacceptably high radiation load in the superconducting coils and the capture linac downstream. The linac downstream is embedded in normal conducting solenoids that are used to focus the positrons into the forward direction further.

Energy deposition calculations with FLUKA are carried out to assess the feasibility of such a setup, studying the heat load and long-term radiation damage on the structure for the Z-operation mode, which has the highest bunch intensity. The impact of the radiation is studied for the target itself, as a high heat load is expected here, as well as extensive DPA. Furthermore, the radiation load on the HTS coils is evaluated since quenching and degradation of the material have to be avoided. Finally, the distribution of secondaries and power of the electromagnetic shower on the capture linac is investigated to quantify the heat load in the cavities and the dose in the solenoids.

Parts of this chapter have been presented in [117].

4.1 Introduction to the FCC-ee Positron Source

4.1.1 | Positron source: Target and Adiabatic Matching Device

The positron production source consists of several different parts. This section discusses the positron capture system and the positron production target, which is hit by 6 GeV electrons to produce positrons[38]. The capture system, also known as the matching device, matches the positrons and focuses them in the forward direction. Downstream, the positrons are injected into the capture linac, the second part of the positron production source, which is discussed in the following section.

Target Choice: Conventional Scheme versus Hybrid Scheme

Two schemes are under consideration for the target: a conventional scheme and a hybrid one. This thesis explores the conventional scheme, but both schemes are discussed here for completeness.

An amorphous tungsten target is used in the conventional scheme[44], as it is a high-Z material with a high melting point of 3695 K[68]. High-Z materials lead to a positron yield increase since the cross-section of the processes producing the electromagnetic showers, Bremsstrahlung and pair production scale with Z^2. An extensive discussion about the underlying physics is given in Chapter 2. The target has to be long enough longitudinally for the shower to develop enough, which is assumed to be at five radiation lengths, X_0. For tungsten, the radiation length is 0.3504 cm, considering a density of 19.3 g/cm^3[68].

The disadvantage of the conventional scheme is the risk of excessive heat load on the target, meaning unacceptable Peak Energy Deposition Density (PEDD). The limit of PEDD is assumed to be at 35 J/g.[44]

The other option is a crystal-based positron source, where an oriented crystal produces photons efficiently. Electrons impinge on a crystal with a small angle compared to the crystal axis experience a strong electric field originating from the crystal atoms. The coherent interaction of the electrons with the crystal lattice leads to the emission of coherent radiation. If the incoming particles align well with the main axis of the crystal, the particles are channelled, which is the case if the impacting angle is lower than the critical angle, $\Psi = \sqrt{\frac{2U_0}{E}}$, with U_0 being the potential well of the crystal and E is the energy of the impacting beam. In the case of a tungsten crystal at room temperature where 10 GeV electrons impact along the main axis, the critical angle is 0.5 mrad. The radiated power is much higher in this orientation than if the particles had impacted the crystal in a random orientation. Additionally, the radiation length in a crystal is much shorter than in an amorphous material, 0.6 mm compared to 3.5 mm for tungsten.[118]

The hybrid scheme combines the crystal and the amorphous target.[44] If electromagnetic showers develop in a thick crystal, similar issues concerning heat load oc-

cur. Additionally, an increased temperature induces thermal vibrations, leading to a decreased channelling effect. The hybrid scheme is applied to avoid an excessive heat load on the crystal. Here, a thin crystal of around 1 mm-2 mm produces high-power photons that impact a conventional amorphous target downstream[118]. Using a thin crystal prevents significant heat load issues on the crystal, shifting the radiation load to the amorphous target downstream, which has to be thoroughly studied.

Crystal-driven positron production has already been investigated in experiments, like at the WA 103 experiment at CERN[119]. Hybrid targets are still in an early stage of their development, with some tests performed in Orsay[119], and it was considered for KEK target[120].

The advantage of a hybrid scheme is that a higher positron yield can be achieved while obtaining less heat load on the amorphous tungsten target. However, since the hybrid scheme is still experimental, the conventional target is still considered the baseline for FCC-ee.[44]

Adiabatic Matching Device (AMD): High Temperature Superconducting Solenoid versus Flux Concentrator

The production of positrons in the target leads to a large transversal momentum spread of the positrons at the target exit, which is reduced with a matching device while increasing spatial spread of the particles. A matching device is a focusing solenoid with a large axial magnetic field at the target exit and decreasing to around 0.5 T downstream. Generally, two types of matching devices exist - the Adiabatic Matching Device (AMD), with an adiabatically decreasing magnetic field, and the Quarter Wave Transformer (QWT), with an abrupt transformation of the magnetic field, which is generated by DC or pulsed coils.[44] For further context, the AMD is discussed, which is already used in machines like SLAC[121], LAL (Orsay)[44], and SuperKEKB (KEK)[122].

The advantage of the AMD is that it captures positrons within a wide bandwidth. However, it leads to a stronger lengthening of the bunch compared to the QWT, which must be compensated downstream in the RF structure. Mechanically, the AMD is often realised with a Flux Concentrator (FC)[123, 124, 125]. A superconducting solenoid instead of the FC is investigated for the FCC-ee positron source in this thesis, which is still in its R&D phase.

Positrons moving along a magnetic field undergo a periodic motion. The action integral, A, of such a motion is an adiabatic invariant. During a slow variation of an external field, in this case, the magnetic field, $\vec{B}$, the action integral stays constant. For the transverse motion of a particle in a constant magnetic field, the action integral can be described with

$$A = \oint \sum_i p_i dq_i = \frac{\pi p_1^2}{eB}, \tag{4.1}$$

where (p_i, q_i) are the canonical variables, p_1 is the transverse momentum of the particle, and e is the charge.

As the period of motion and the action integral change slowly, in the case of a slowly changing magnetic field, this can improve the acceptance yield.

The magnetic on-axis field is analytically described as

$$B_z = \frac{B_0}{1+\mu z}, \tag{4.2}$$

with $z = 0$ being at the target exit. μ gives the decay rate of the magnetic field. For the FCC-ee positron source, the decay rate is fixed at $50\,\mathrm{m}^{-1}$. The peak magnetic field at $z = 0$ is given with B_0 =12 T[1], while B_z gives the resulting on-axis field decaying adiabatically from B_0 to 0.5 T.[126] Now, the realisation of such a magnetic field is discussed.

In a FC, conically tapered solenoids (see Fig. 4.2) provide the magnetic field for positrons exiting the target. The coils are powered by fast pulses of 25 μs length and a high peak current of 20 kA. The peak magnetic field strength is at 7 T, which results in a cone diameter of 8 mm at the entrance of the FC to 44 mm at the exit downstream. Longitudinally, the cone stretches over 70 mm, while the entire device has a length of 14 cm.[127]

The shape of the magnetic field can be seen in Fig. 4.1. The peak of the magnetic field is slightly downstream of the target exit, as the distance between the target and the field-giving FC is 2 mm apart from each other. After the peak, the magnetic field declines adiabatically.[128]

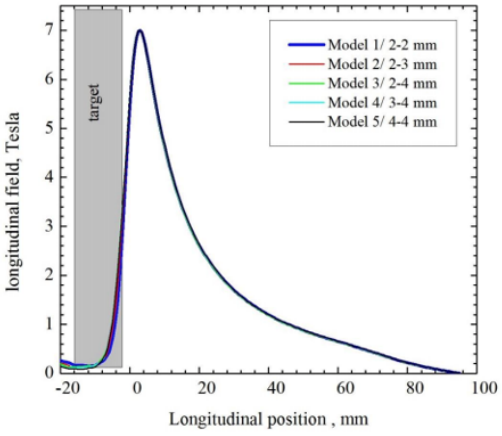

Fig. 4.1. Magnetic field in the Flux concentrator. Plot provided by I. Chaikovska ([129])

Such a FC is installed at the Super KEKB positron source, powered with a 6 μs pulse current of 6 kA. These quantities lead to a peak field of 1.8 T.Around the FC, there are bridge coils that are powered with 600 A and add another 0.5 T, which can be seen in Fig.

[1] 12 T is the on axis peak magnetic field for the HTS solution that is investated in this thesis.

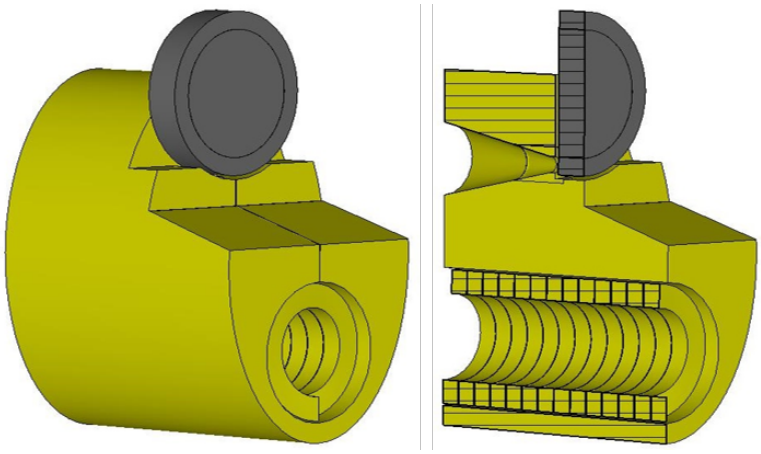

Fig. 4.2. Geometry sketch of the flux concentrator with the beam coming from the right side. The sketch is provided by [127].

4.3. The whole structure is embedded in a vacuum vessel. The target is installed 2 mm upstream of the FC, with a slight offset of the beam axis, as the electron beam also goes through this structure in this machine. If positrons should be produced, the electron beam is steered onto the target. Otherwise, the beam moves through a small hole, all within a 7 mm diameter. [130]

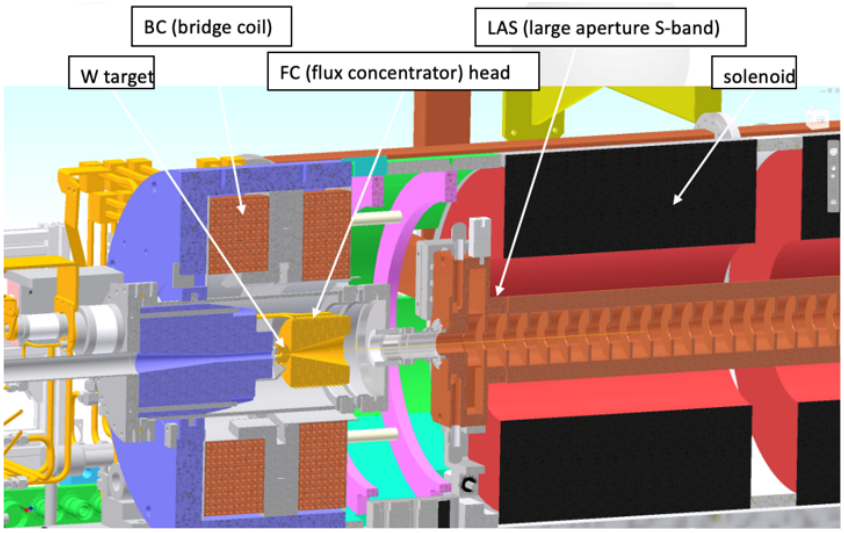

Fig. 4.3. Geometry of the Super KEKB target. The schematic is taken from [44].

A different solution is investigated for the FCC-ee positron source. Instead of a FC, HTS coils should be used to produce the magnetic field. Here, no tapered coils are used, but the coils are all placed at the same radial distance from the beam. Furthermore, the coils are already upstream of the target, which results in the peak of the magnetic field within the length of the target (see Fig. 4.1). With this technology, high magnetic field

strengths can be achieved, which improves the positron yield by a factor of two.[131] HTS coils are preferred over low-temperature superconducting coils, as the cooling can be done with liquid nitrogen instead of liquid helium and higher magnetic field values can be achieved.

4.1.2 | Positron source: Capture and Positron Linac

This part of the accelerator chain captures, transports and accelerates the positrons that exit the matching device with a large transverse emittance and energy spread. The positron linac is split into two parts, the capture linac and the injector linac. The capture linac reduces the energy spread of the positrons exiting the matching device and accelerates them to 200 MeV. Downstream, the positron linac accelerates the positrons to 1.54 GeV. After passing through the system of the two linacs, the positrons are matched to the conditions required to enter the DR.

This thesis quantifies the power deposition and long-term ionising dose in the capture linac and the surrounding solenoid, and the required shielding is designed. A standing wave or a travelling wave RF structure is proposed for this linac, whereas the first is the current baseline. This RF structure is embedded in a normal conducting solenoid that generates a constant magnetic field. The first RF structure is operated in decelerating mode to improve the capture efficiency.[132]

An S-Band and an L-Band structure are studied for the capture linac, where S and L are a reference to the operation frequency band. The S-Band linac would be operated at 3.0 GHz with a solenoid field of around 1.5 T, while for the L-Band version, the frequency is at 2.0 GHz and a magnetic field strength of 0.5 T. A similar structure as the latter was already proposed for the CLIC injector.[128] Depending on the chosen structure, the longitudinal position of the target changes slightly with respect to the coils and the magnetic field. For now, as a baseline, the L-Band linac is chosen.

The normal conducting solenoids around the RF structure provide the magnetic field in the forward direction. They are split into one long solenoid covering nearly all of one structure, with each one shorter solenoid to the side (see Fig. 4.15). In the connectors between two structures, there is also a short solenoid. While the short solenoids are smaller in the longitudinal direction, they have a larger radial extension. The fringe fields and other changes in the magnetic field are not considered for energy deposition studies, as a constant magnetic field is sufficient to simulate a constant magnetic field along the vacuum chamber. Additionally, no time-dependent electric field is implemented, whereas this simplification does not affect the results significantly, as shown later.

4.1.3 | Parameters used for the FCC-ee Positron Source

This thesis investigates two scenarios for the electron drive beam parameters: an optimistic and a pessimistic case. The second scenario is based on the maximum bunch charge the electron can deliver, while the first scenario is expected to be more realistic if the simulated positron yield can be achieved. Depending on the positron production yield and the capture efficiency, the electron beam power for the positron production hence varies about a factor of 4 (see Table 4.1). So far, an electron yield of 1 is assumed, whereas an electron yield of a factor 2 would decrease the bunch charge by a factor 2. It is important to understand the positron yield in order to determine the required bunch population of the drive beam.

However, the required beam parameters are still subject to evolution since the positron transmission efficiency is still unknown. The latter is mainly determined by positron losses in the damping ring, particularly during the injection. The parameters assumed in this thesis are given in Table 4.1, which shows all the parameters used for the simulations done for this part of the machine[133].

	Optimistic	**Pessimistic**
e- drive beam energy	6 GeV	
Beam size (RMS)	0.5 mm	
Bunch length (RMS)	1 mm	
Energy spread (RMS)	0.1 %	
Repetition rate	200 Hz	
Bunches per pulse	2	
Target length	$5X_0$ =17.5 mm	
Bunch intensity	1.8×10^{10} e−	3.47×10^{10} e−
Beam current	1.43 nC	5.56 nC
Beam power	3.43 kW	13.34 kW

Table 4.1. Parameters for the optimistic and pessimistic scenario used for obtaining the results of the positron source simulations.

All results presented in this chapter exhibit a linear dependence on the electron drive beam power. Therefore, the results can be rescaled to the final beam parameters once established.

These parameters correspond to the Z operation mode (45.6 GeV), which has the highest beam intensity of all four operation modes[33]. Even though the final energy will be higher for the other operation modes, the electron drive beam energy for positron production stays the same while having lower beam intensities.

The parameters in Table 4.1 are necessary to calculate instantaneous properties like heat load and power density. The number of electrons that hit the target per year is also required for long-term effects like the dose or DPA, with 185 days assumed to be a year of operation and a duty factor of 0.804[50]. Furthermore, only half of the time, the electron bunches hit the target, as during the other time, the electrons exiting the common linac

enter into the higher energy accelerator chain and the collider ring. Considering these assumptions, for the pessimistic case, one obtains:

$$2\,\text{bunches}\cdot 200\,\text{Hz}\cdot 3600\,\text{s}\cdot 24\,\text{h}\cdot 185\,\text{days}\cdot 0.804\cdot 3.47\times 10^{10}\,\text{e}-/\text{bunch}\cdot 0.5 = 8.9\times 10^{19}\,\text{e}-/\text{year}. \tag{4.3}$$

For the optimistic case with a lower bunch charge, 4.6×10^{19} e−/year impinge on the target. This assumption is conservative, assuming that the same beam intensity is needed during the filling from scratch and the top-up injection.

4.2 Radiation Load Studies for the Target and the AMD

This section discusses the matching device and target in more detail. First, the geometry is discussed, followed by a particle distribution analysis and energy deposition studies. In the appendix, two parts are devoted to this part of the machine. There, the different DPA models implemented in Fluka and their impact on the simulation results are elaborated (see App. A). The second appendix assesses the energy deposition for the P^3 experiment at PSI[134] (see App. B).

4.2.1 | Evolution of the AMD and Target Configuration

The work presented in this section was based on an iterative design approach in close collaboration with magnet engineers from PSI/Switzerland and beam dynamics experts from the BE/ABP group at CERN. The AMD and target configuration evolved over several months, taking into account engineering constraints, radiation shielding requirements and beam dynamics. The coil and cryostat geometry and the magnetic field configuration were developed at PSI, whereas the BE/ABP group performed the positron yield optimisation. In the scope of the thesis, all radiation load calculations for the AMD and target were carried out, and the shielding design was developed.

The project started from scratch, with a basic model to prove the concept and derive the first radiation load estimates. Through several iterations, the layout evolved into a more realistic design. This section highlights the evolution of the AMD and target layout by presenting the corresponding Fluka geometry models. The radiation load results are only presented for the most recent geometry versions.

The material for the cylindrical target is W-Re26, a tungsten alloy that changed to pure tungsten in later stages. Tungsten is often used for targets due to its high Z number, which leads to high positron production efficiency. The radius of the target varies between the different versions, but the length stays nearly the same. Positron yield optimisation studies showed that a target length of about 17.5 mm to 18 mm, corresponding to $5X_0$, is the optimal length.[132] This length allows sufficient shower propagation in the target and achieves the best positron yield.

Dedicated thermo-mechanical studies are needed to develop an engineering solution that copes with the heat load in the target and shielding. These engineering studies are beyond the scope of the thesis. The total heat load and peak power density are significant; therefore, it is unclear if the target can be stationary. It is under study if a moving target is needed, as it is used at SLAC[44]. Also, cooling and installation features are still under investigation.

In the following paragraphs, the different models are discussed. Version 4 is not presented since it was discarded by the group at PSI before energy deposition studies could be performed. An according magnetic field is implemented for each version, representing the field produced by the coils. The materials used for the components of the

positron source are always the same for all different versions, except for a few variations. The components of interest include the coils, the cryostat, the target, the shielding, the mounting structure, and the vacuum chamber.

The material choices are similar in several versions, so they are presented now. As discussed, the target is made from tungsten or a tungsten alloy. The high Z of tungsten is also beneficial for the absorption of secondary showers, and therefore, it is also used for a possible radiation shielding. The vacuum chamber is made of copper, which has good manufacturing and desorption properties. The aluminium vessel for the coils is embedded in a stainless steel cryostat. The mount between the vessel and the cryostat was initially intended to be epoxy and later changed to steel since it is not sensitive to the ionising dose like organic materials. The coils are HTS coils made out of YBCO tape, which has the critical temperature within the range of liquid nitrogen[135].

This study aims to optimise the geometry for an optimal positron yield while keeping the heat load on the components as low as possible.

Version 1

A simple geometry (see Fig. 4.4) was designed for the first model (V1) of the positron production target. The target has a length of 1.6 cm and a diameter of 4 cm. A large coil upstream and eight small coils downstream produce an adiabatically declining magnetic field. All coils are made out ReBCO tape and covered by a 1 mm copper layer. These components are embedded in an iron or Inermet180 cuboid with a length of 21 cm and spreading 20 cm in x and y.

Upstream of the target, the vacuum chamber has a diameter of 2 cm, while downstream, it widens up to 4 cm. A dedicated vacuum chamber was neglected for the first model.

No radiation shielding, cryostat, or vessels were implemented in this model, as it served purely as a proof of concept simulation. Furthermore, cooling the coils would be difficult in this setup, and this amount of tungsten would not be feasible.

Version 2

Version 2 (V2) represented the first realistic setup, which has the most complex geometry (see Fig. 4.5) compared to all other versions. The target has a thickness of 2 cm and extends radially over the full positron production source. Close to the centre, the target produces positrons, while further outside, the absorbing properties of tungsten are used as shielding for the geometry downstream. Furthermore, the target separates the upstream and downstream cryostat. The vacuum chamber has a radius of 2 cm, upstream and downstream of the target. The stainless steel cryostat separates the vacuum from the coils.

Four 1.2 cm wide HTS coils are located upstream at a radius of 5.9 cm, and the length

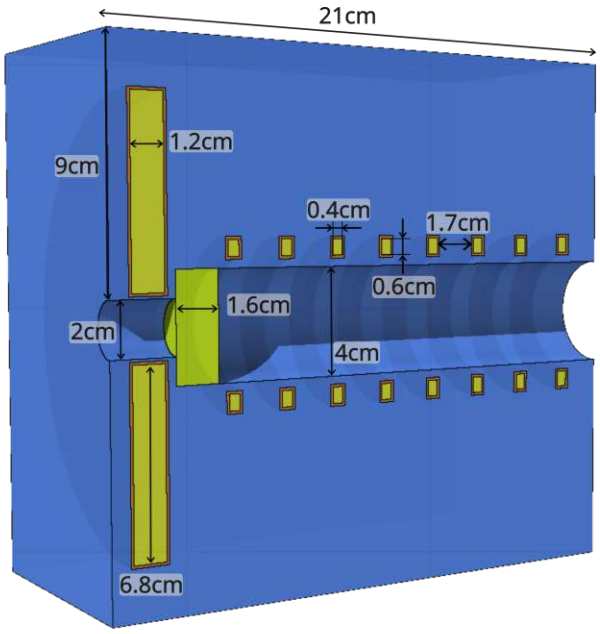

Fig. 4.4. 3D model of target V1. One large coil and eight small coils are embedded in a thin layer of copper, surrounded by a tungsten block. The green centre piece displays the target, with the beam entering from the left side.

is kept for all following versions. They are embedded into an aluminium and copper structure held by organic fibre glass mounts. Organic components should be avoided regarding energy deposition, as they are prone to radiation damage. Outside the aluminium and copper structure is another vessel made out of a layer of copper and iron.

Downstream of the target, a 2 cm thick layer of Intermet180 parallel to the beam acts as shielding, located within the cryostat. Another 3 cm of tungsten shielding is also implemented parallel to the two downstream coils. The coils are different sizes and placed further outside than the upstream coils. Like upstream, these coils are embedded in a structure of aluminium and copper and held in place by fibreglass mounts.

This version is a realistic model, as it contains all the operationally essential parts not included in V1, like the vessel or the cryostat. All the coils are larger than those in V1, essential for producing an adequate magnetic field due to their location further outside.

The shielding is only located downstream, as negligible heat load was expected upstream. The shower produced in the target mainly impacts the components placed downstream, so extensive shielding was added. It turned out that the shielding normal to the beam axis was not needed, as the radiation load was insignificant.

Furthermore, it was remarked that the inorganic mounts would be preferable over organic fibreglass, as it is less prone to radiation damage.

Finally, this version was discarded, as a less complex solution could be envisaged with Version 3.

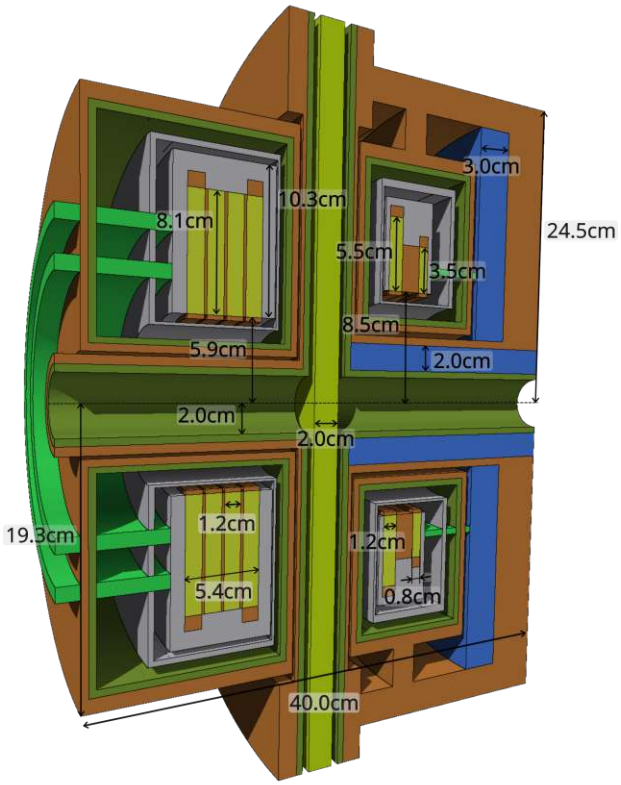

Fig. 4.5. 3D model of target V2. Upstream of the target (light green), four coils are embedded in an aluminium structure. Epoxy mounts (neon green) connect the coils with the cryostat. Downstream, the shielding (blue) protects two coils.

Version 3

In version 3 (V3) (see Fig. 4.6), the main difference compared to V2 is that there is no separation between an upstream and downstream part of the positron production source.

The cylindrical target is embedded in the beam pipe, with a length of 1.8 cm and a radial component of 3 cm, located at the same longitudinal position as the last coil. The target length gets closer to 1.75 cm ($\approx 5X_0$), which is found to be the optimal length. Next to the classic target design, a more complex U-shaped target was also implemented to shield the coils simultaneously. This design was discarded due to its complexity and limited effect.

Contrary to V2, no dedicated shielding is implemented in this version, as the radiation load on the coils was expected to be low due to their position upstream of the target. Seven coils of 7.5 cm are used in this geometry, again embedded in an aluminium and copper structure. As requested, an inorganic material, copper, that withstands radiation better, is now used for the mounts.

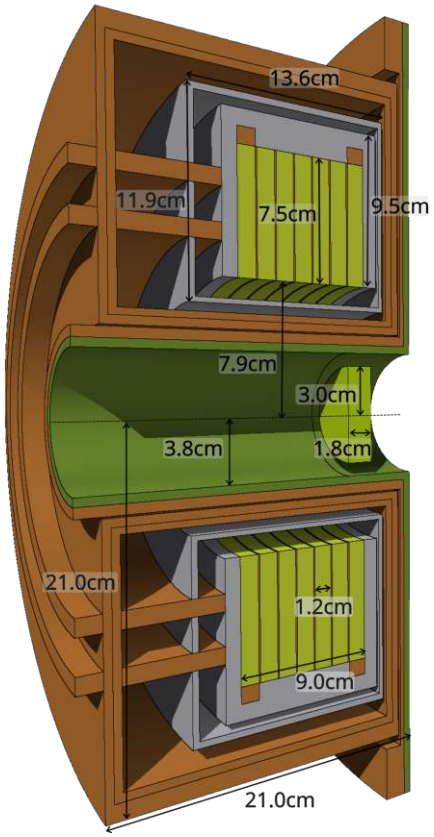

Fig. 4.6. 3D model of target V3, that includes seven coils embedded in an aluminium structure. No shielding between the target and the coils is used in this version.

The geometry of this version was already promising, with an acceptable complexity level and positron yield. However, the radiation load was significant, particularly the integrated dose on the coils. So, a further iteration was performed.

Version 5

Version 5 (V5) is the version that followed V3 after V4 was discarded in the early stages by the PSI group. The complexity level is similar for V3 and V5, but significant changes were introduced, like the number of coils, radiation shielding, and the target size.

The target has a thickness of 1.8 cm and a radius of 4.375 cm, which is larger than in the other presented versions. Increasing the target size should help dissipate the heat and protect components further outside. The target exit is located 1.35 cm downstream of the peak magnetic field (20 T).

Further outside, an Inermet180 shielding with a thickness of 1.8 cm covers the whole geometry longitudinally. This addition was deemed necessary, as the heat load on the

coils in the V3 was too high.

In this version, five coils are installed to produce the magnetic field. The first three coils are upstream of the target, and the last two overlap with the target position. They are located at a radius of 8.2 cm and extend 6.3 cm to the outside. As in the previous versions, they have a thickness of 1.2 cm and are separated by 1 mm of copper.

The coils are embedded in a copper and steel vessel, which encloses the coils. The mount that connects the vessel to the cryostat is now made from iron, compared to copper in V3.

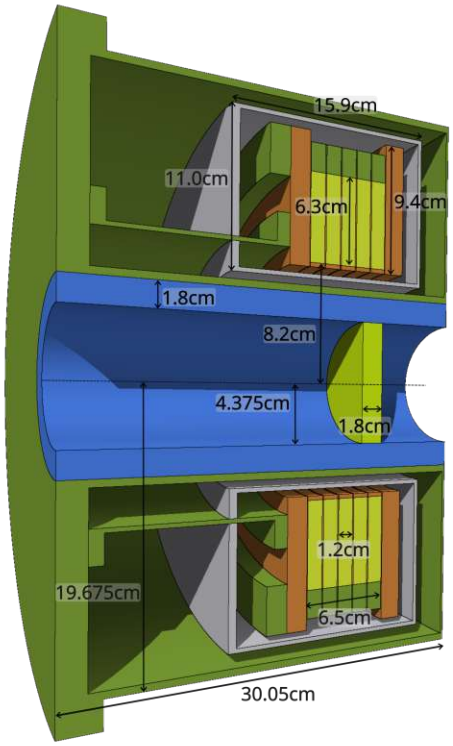

Fig. 4.7. 3D model of target V5, where the target is surrounded by a tungsten shielding. At a position of 8.2 cm radially to the outside, there are five coils of the same size. The coil the furthest downstream overlaps longitudinally with the target position.

Version 6 - S Band & L Band

V6 is the most recent version, where the radiation load for two different target positions is studied. Depending on the RF structure downstream (S-band or L-band), a different target position gives the optimal positron yield. Furthermore, V6 is essential, as the same geometry will be installed in the P^3 experiment at PSI, where no shielding is needed due to the smaller beam power. It would be optimal if the identical layout could also be used at the FCC-ee positron production source with the addition of a tungsten

shielding.

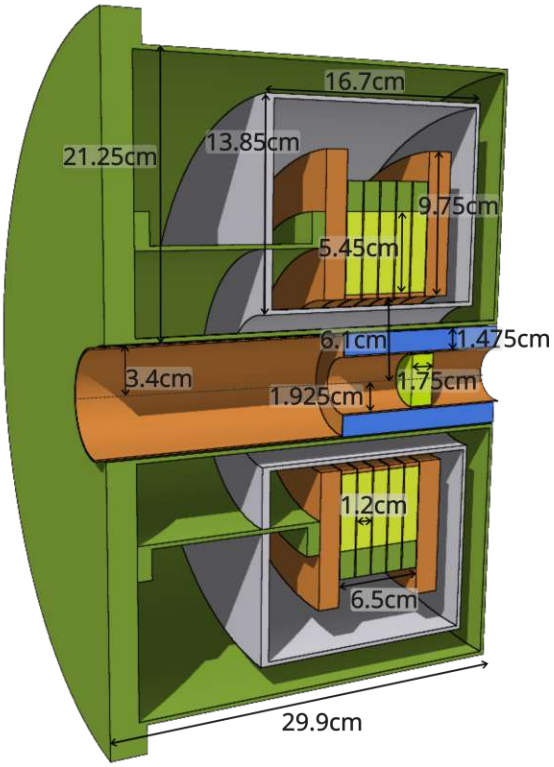

Fig. 4.8. 3D model of target V6, which is the most realistic geometry. The setup of the vessel, the cryostat and the coils is mostly similar to V5, with the difference that the coils are at a radial position of 6.1 cm and extend shorter to the outside. The longitudinal position of the target depends on the type of RF structure downstream. A shielding is located between the coils and the target, but the final design has yet to be established.

Structurally, V5 and V6 are relatively similar, having the same number of coils and an identical setup of the vessel and the mounts. The target size, the location of the coils, and the shielding are realised differently in V6. Additionally, a vacuum chamber with a thickness of 0.5 mm is implemented in this version.

For this version, simulations are performed for the optimistic and the pessimistic case, where the electron beam has different power (see Table 4.1). Additionally, for the optimistic case, there has been a distinction in the target placement between the S-Band version and the L-Band version. Depending on the choice of the capture linac design, S-Band or L-Band, the target must be placed at a different longitudinal position. For the optimistic case, the W-Re26[136] target has a radius of 1.925 cm and for the pessimistic parameter set, the target is pure tungsten with a radius of 1.5 cm. The target radius influences the positron yield, with a larger radius being beneficial[137]. However, for the heat extraction, a target as small as possible improves the efficiency and feasibility of this solution[138]. Therefore, a compromising solution still has to be found.

In the pessimistic case, the target is pure tungsten as it allows to manufacture the target and the shielding from one piece, which is beneficial for the heat extraction. The shielding is 1.9 cm for the pessimistic case, while it is thinner for for the optimistic case (1.475 cm), where the target and the shielding would need to be two separate elements. The shielding longitudinally covers the area from the first coil upstream to the end of the cryostat.

The target length is 17.5 mm, equal to $5X_0$, allowing for sufficient shower development. The target exit varies for all three versions, being at 4.1 cm (Optimistic: L-Band), 2.0 cm (Optimistic: S-Band), or 3.5 cm (Pessimistic), downstream of the peak field.

Finally, the coils are in a slightly different position, compared to V5, being at a radius of 6.1 cm and they have a radial extension of 5.45 cm.

Overview of different studied versions

After introducing the various versions, a summary is given for the versions that will be used in the upcoming section.

		V5	V6 - optimistic		V6 - pessimistic
			L-band	S-band	
Beam power		3.43 kW	3.43 kW		13.37 kW
Target	Thickness	1.8 cm	1.75 cm		1.75 cm
	Radius	4.375 cm	1.925 cm		1.5 cm
	Exit	3.1 cm	2.0 cm	4.1 cm	3.5 cm
Shielding	Thickness	1.8 cm	1.475 cm		1.9 cm
Coils	Radial Position	8.2 cm	6.1 cm		
	Radial extension	6.3 cm	5.45 cm		

Table 4.2. Overview of the various AMD versions that are investigated in detail.

4.2.2 | Secondary Particle Distribution from the Target

As a start to the radiation load assessment, the shower of secondaries is investigated in close detail in different versions and at various points in the machine. In this type of simulation, the energy carried by the particles is analysed, leading to a better understanding of the device and evaluating the plausibility of the results before launching the energy deposition studies.

The distribution is analysed in three critical points in and around the matching device. The first location is the target exit, where the solenoid field of the HTS coils has not influenced the particle trajectories strongly yet. The second time, the particles are dumped at the exit of the AMD, which is around 10 cm downstream of the peak magnetic field strength. At this point in the setup, a substantial fraction of particles is already lost, which exited the target with a large angle and impacted the AMD. Finally, the distribution at the entrance to the capture linac is examined around 30 cm downstream.

As mentioned, in this type of simulation, the energy carried by particles is determined rather than the energy deposition in the components. These simulations are also run in FLUKA, including a user-routine (`mgdraw_exbkg.f`[106]), where the particles are dumped as soon as they enter a dedicated region, which is indicated in the Fortran file. The dumped particles and their properties are written into an ASCII file.

The output files are manipulated, including adding a necessary time structure, as the beam optics group further uses them as input files for studies in the capture linac.

First, the data for V5 and V6 is compared in Table 4.3. The electrons that impact the target have an energy of 6 GeV. One third of the original beam is deposited in the target and surrounding AMD. V5 and V6 have different magnetic fields implemented, and additionally, the V6 results are produced using a pure tungsten target. For this comparison, the data is given for the location of the AMD exit.

		V5	**V6**
r <1.5 cm	GeV pp (e-)	0.70	0.72
	GeV pp (e+)	0.67	0.69
	GeV pp (γ)	2.53	2.54
r <0.5 cm	GeV pp (e-)	0.47	0.51
	GeV pp (e+)	0.44	0.49
	GeV pp (γ)	1.75	1.92

Table 4.3. Energy carried by electrons (e-), positrons (e+) and photons (γ) at the AMD exit in V5 and V6. The results are given in GeV per primary electron impacting on the target. The results are given for a radius limitation of 1.5 cm and 0.5 cm.

The total amount of particles leaving the AMD within a radius of 1.5 cm has an energy of around 65% for both versions compared to the drive beam power of 6 GeV. This evaluation includes all particle types, leaving the target downstream, mostly electrons,

positrons and photons. A percentage lower than 0.3% are other particles, primarily neutrons.

If the total amount of particles is split into different particle types, it is seen that around two-thirds of the energy is carried by photons. The rest of the energy is evenly split between electrons and positrons. For V6 and a radius smaller than 0.5 cm, the electrons and positrons carry more energy than the ones observed with V5, which indicates a better efficiency in terms of positron production for V6 than V5.

Now, the energy per primary is compared for the different positions in the positron production source for V6 (see Table 4.4). The energy is expected to decrease when moving further away from the target as energy is deposited on the AMD, which can be seen in all cases. For photons, a significant amount of energy is lost within the few centimetres between the target exit and the AMD exit. The photons leaving the target do not interact with the solenoid field and often impact the AMD structure and lose energy. At the same time, the electrons and positrons are pushed into the forward direction with this magnetic field.

		Target Exit	**AMD Exit**	**RF Entrance**
r <1.5 cm	GeV pp (all part.)	4.55	3.99	3.29
	GeV pp (e-)	0.75	0.73	0.64
	GeV pp (e+)	0.72	0.70	0.61
	GeV pp (γ)	3.08	2.55	2.04
r <0.5 cm	GeV pp (e-)	0.75	0.51	0.23
	GeV pp (e+)	0.72	0.49	0.23
	GeV pp (γ)	3.00	1.92	1.13

Table 4.4. Energy per primary at various places (the exit of the target, the exit of the AMD and the entry into the Capture Linac) in the positron target in V6.

At the target exit, all particles are strongly centred, where most energy is carried within a radius of 0.5 cm. Moving downstream to the RF entrance, it becomes evident that the electrons and positrons carry relatively more energy than the photons. However, a rapid decrease in GeV per primary is seen when comparing the data for electrons and positrons within at a 1.5 cm radius and the 0.5 cm radius between the AMD exit and the RF entrance. This change leads to the conclusion that the electrons and positrons are spread more at the RF entrance than at the target exit.

Finally, the actual numbers of particles that are produced per primary are analysed (see Table 4.5). For one impacting electron, 328 particles are leaving the target. Photons are more abundant as bremsstrahlung events are more probable than pair production. Furthermore, if the emitted photon in a bremsstrahlung event is below the pair production threshold, it enters the regime of Compton scattering. This interaction scales with

Z, making interactions less likely. Therefore, the photons can travel further, eventually producing a high abundance of photons.

The total amount of particles decreases when moving further downstream as particles are lost in the components. However, the percentage of positrons and electrons increases as they adhere to the magnetic field, while the neutral photons are quickly lost. This part of the machine aims to produce positrons, which makes the loss of photons generally subsidiary in terms of positron production efficiency. However, for radiation load studies, the particles lost in the structure are the ones causing the radiation load impact, which is the topic of the next section.

	Target Exit	**AMD Exit**	**RF Entrance**
Total pp	328	170	164
e- pp	5.8%	11.8%	14%
e+ pp	4.6%	8.8%	9.8%
γ pp	89.6%	79.4%	76.2%

Table 4.5. Number of produced particles per primary and the relative contribution. (The transport threshold is set at 100 keV.)

4.2.3 | Power Deposition in the AMD, Target, and Shielding

In this and the upcoming sections, the power deposition in the different components of the AMD is discussed. The results are presented for the optimistic and pessimistic beam parameters to highlight the differences caused by the different beam power. The optimistic case has a beam power of 3.43 kW, while the beam power is to be found at 13.34 kW for the pessimistic case, nearly a factor 4 higher (see Table 4.1). The relevant geometries are V5, V6 L-Band, and V6 S-Band$_{opt}$ for the optimistic case. For the pessimistic case, a slight variation of V6 S-Band$_{opt}$ is studied, where the target exit is located at 3.5 cm downstream of the peak magnetic field, meaning 1.5 cm further downstream than in the optimistic case. The V6 S-Band$_{pes}$ geometry is the one that will be implemented in the P^3 experiment (see Table 4.2).

First, the total power impacting the AMD for the optimistic and the pessimistic case is discussed. This quantity gives an insight into how the power is distributed on the geometry and leads to a first overview of the beam impact.

Optimistic Scenario - Version 5 & 6

V5, V6 S-Band, and V6 L-Band are discussed for the optimistic scenario. For the latter two, the target is located at different longitudinal positions regarding the peak magnetic field, depending on the choice of RF structure downstream.

	V5	**V6 L-band**	**V6 S-band**
Target	906 W	862 W	869 W
Shielding	69 W	149 W	209 W
Cryostat and coil supports	3.3 W	8.1 W	11.8 W
Coils (1-5)	0.09 W to 0.18 W	0.15 W to 0.68 W	0.27 W to 1.25 W
Total	980 W	1030 W	1126 W

Table 4.6. Absorbed power in different components in V5 and V6.

Table 4.6 gives the absorbed power in the different versions for the optimistic case with a beam power of 3.43 kW. The total power on the AMD, the target and the shielding, and, therefore, the power escaping the device depends on the geometry and the target location in the AMD. V6 generally absorbs slightly more power than V5 due to the components being closer to the beam axis, which leads to a higher impact on V6. Assuming a beam power of 3.43 kW, around ≈ 30% of the beam power is deposited in the AMD and target, while the remaining ≈ 70% escapes the structure. Of these 2.3 kW to 2.5 kW escaping the AMD, around 2 kW are carried by photons and electrons located. The positrons

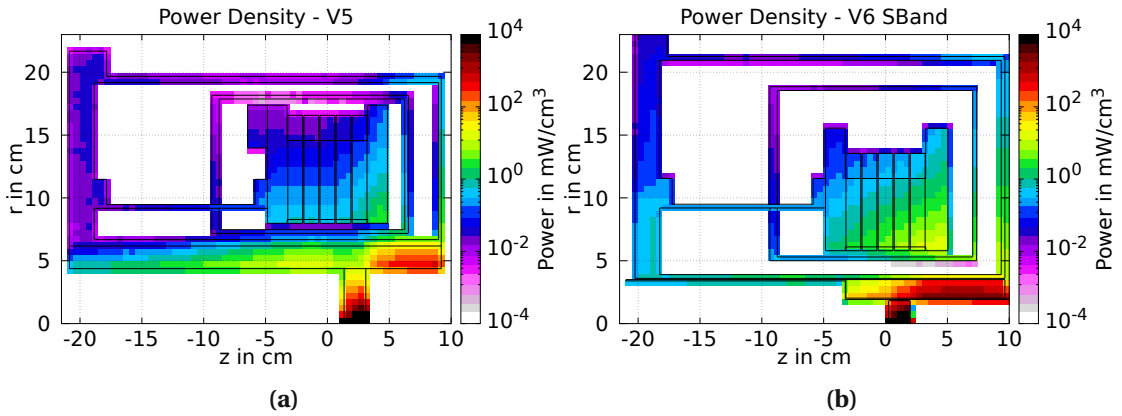

Fig. 4.9. Power density for (a) V5 and for the (b) V6 S-Band.

carry around 0.3 kW to 0.5 kW, which are then accelerated in the RF structure.

Around 25% (906 W for V5, ≈865 W for both V6) of the electron beam power is dissipated on the target (see Fig. 4.9). The target of V5 absorbs slightly more power due to its larger radial size, which means there is more material to absorb the power, leading to the conclusion that the target itself has a shielding effect. If more power is deposited the target, less power is deposited the surrounding components.

The impact on the shielding is around two to three times higher for V6 than V5, which is caused by two main factors. In V6, the shielding is closer to the beam, and the target is smaller in this version, so it absorbs slightly less.

Pessimistic Scenario - Version 6

In the case of 13.34 kW beam power, 3100 W are deposited on the target, 3.5 times as much as with the optimistic settings for the S-Band version of V6. A similar picture can be seen in the behaviour of the shielding, which is thicker for the pessimistic scenario (see Table 4.2. Comparing the difference in deposited power (a factor of 3.5) with the difference in impacting beam power (a factor of 4), it becomes evident that the relatively small changes in the target design impact the deposited power significantly. In this pessimistic scenario the target shrinks and the shielding becomes larger, so the target is relatively less impacted, and the impact on the shielding is higher. However, the total amount of energy scales as expected.

The total power on the coils increases only by around 2.2 for the pessimistic case. While the power ranges from 0.27 W to 1.25 W for the beam power of 3.43 kW, the coils are impacted by 0.6 W to 2.9 W for 13.34 kW of beam power. The smaller power increase on the coils is explained by the changes in geometry between the two versions, including the target position further downstream and the thicker shielding that protects the coils better in the pessimistic case.

	Pessimistic	Optimistic
Target	3100 W	869 W
Shielding	1040 W	209 W
Coils (1-5)	0.6 W-2.9 W	0.27 W-1.25 W

Table 4.7. Absorbed Power in V6 comparing two different beam powers and different shielding configurations.

4.2.4 | DPA and Energy Density in the Target

The following section discusses the radiation load on the target, which includes the energy deposition density for the instantaneous effects and the DPA for the long-term effects. Once again, the optimistic case is treated separately from the pessimistic one.

The target has to sustain several challenges, and the aim is to find a solution that allows the use of a static target, which can stay in the matching device for the entire operating time of FCC-ee[24]. The heat load should not be too high so efficient cooling is possible. Cooling should be facilitated by having the target and the shielding made of one piece, where it is easier to place cooling tubes in the combined structure.

Optimistic Scenario - Version 5 & 6

The maximum power density reached on the target is similar for V5 and V6 with around 21 kW/cm^3, an acceptable value for cooling and material strain. Additionally, a strong temperature gradient is visible in the target. The peak values are expected to be similar for V5 and V6, as the targets are similar for both cases. The different longitudinal position does not impact the power density values, as there is no interaction before the target.

Regarding long-term effects, DPA is a more critical property for the target than the ionising dose due to the choice of inorganic material. If the DPA is too high it results in swelling of the material[139], which could lead to a decrease in positron yield that has to be avoided. Furthermore, such a DPA value leads to degradation of the material which impacts its properties, such as the thermal conductivity. This eventually affects the cooling efficiency. On the target, values of around 3 DPA/year are obtained, assuming a damage threshold of 90 eV and a beam power of 3.43 kW. Considering an electron beam, this is a high value as the DPA is usually caused by hadronic particles. A DPA of this value possibly leads to the degradation of the material and needs further investigation.

Pessimistic Scenario - Version 6

For the pessimistic case, the maximum power density is found at around 80 kW/cm^3, which is located at the downstream face of the target centred around the beam axis (see Fig. 4.10). The peak on the exiting face increases the challenge of cooling the device,

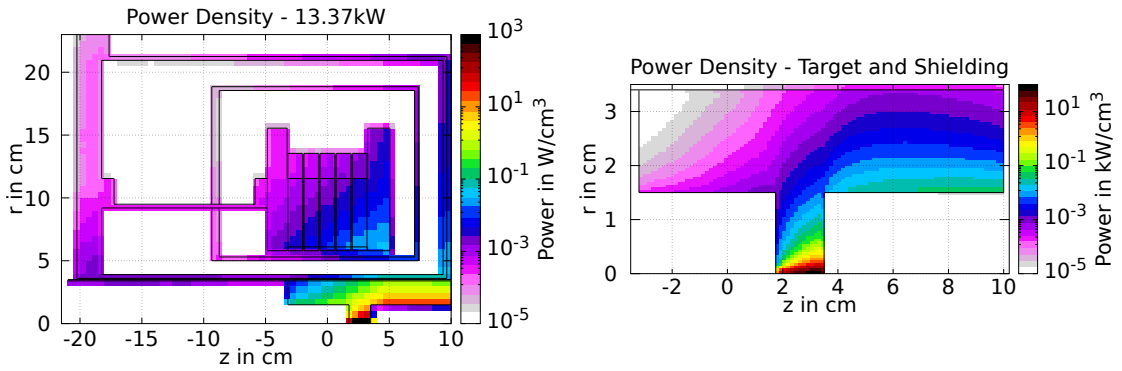

(a) (b)

Fig. 4.10. Power density on the (a) full AMD and (b) a zoom onto the target and shielding with a 13.37 kW beam. Mind the different scales for (a) and (b).

compared to a situation where a heat load peak was found in the longitudinal central part of the target[140]. Colleagues from SY-STI-TCD study this problem in greater detail and try to find a solution to mitigate the issue. While 80 kW/cm^3 is a high value and it is challenging to have sufficient cooling, the temperature of the tungsten stays below its melting point[68].

The main concern in this scenario is that the DPA reaches a maximum of 8 DPA/year on the exiting surface, which is not acceptable. Numbers that high would require several target exchanges per year. If not possible differently, the target-shielding structure could be exchanged once a year. Due to the highly radiative environment, this exchange must be performed by a remote setup already done in different institutes and setups. Another possibility could be a larger incoming beam that would spread out the peak DPA value over a larger area and lower the maximum value[138]. Another proposed mitigation strategy is to move the beam and paint a broader target spot, which would also spread the DPA[141]. However, at the moment, an electron yield of 1 is assumed, meaning that one positron is produced for every electron of the electron drive beam. As this assumption is highly conservative, the yield could go up 3-4 times, requiring an electron drive beam with a third or a quarter of the current bunch charge. Since the DPA scales linearly with the bunch charge, this would also improve the situation significantly[142].

4.2.5 | Heat Load, Ionising Dose and DPA in the Coils

Three different properties, the power density, ionising dose, and DPA, are investigated for the HTS coils. If the power density is too high, the magnet quenches, i.e., makes a transition to the normal-conducting state. As HTS coils are used in this part of the machine, the limits for quenching are much higher than for superconducting magnets made of NbTi or Nb_3Sn. Nevertheless, it is essential to investigate the power density

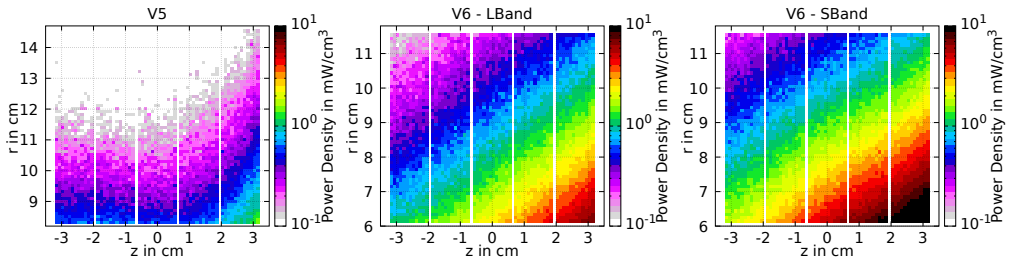

(a) **(b)** **(c)**

Fig. 4.11. Power density on the coils of (a) V5, (b) V6 L-Band and (c) V6 S-Band.

to spot unexpected showstoppers. For the long-term effects, the dose and the DPA are investigated. If the dose exceeds a limit of 30 MGy[109], organic materials are deteriorated, often used as insulators in the coils. A priori, no organic insulation is foreseen in the coils, but the dose is still evaluated. The DPA levels are assessed for completeness, which are expected to be low due to the beam properties and coil locations[2].

Optimistic Scenario - Version 5 & 6

For all geometries, the furthest downstream coil (Coil 5) is impacted the most. In terms of absolute power, Coil 5 absorbs 0.2 W in V5, and 0.7 W and 1.25 W for V6 for L-Band and S-Band$_{\text{opt}}$, respectively, while the other coils absorb significantly less power. This pattern is visible for the power density and ionising dose as well.

The low value in V5 is due to the coils that are located further outside, at a radial position of 8.2 cm compared to a radial position of 6.1 cm for V6. Furthermore, the shielding is slightly thicker for V5 than for V6.

The difference in power density between the L-Band and S-Band$_{\text{opt}}$ shows that the longitudinal position of the target with respect to the peak magnetic field leads to significantly different values. A peak power density of 16 mW/cm^3 is obtained in the S-Band$_{\text{opt}}$ case and 8 mW/cm^3 in the L-Band case, which means that the peak power density doubles by a target shift of 2 cm (see Fig. 4.11). The obtained values are sustainable for the heat evacuation and the risk of quenching is negligible.

Like the power density, the dose has the highest impact on Coil 5. For V5, a maximum of 2 MGy/year is reached. In the S-Band$_{\text{opt}}$ version of V6, an ionising dose of 22 MGy/year is reached, while the maximum in the V6 coils is at 8 MGy/year (see Fig. 4.12). As mentioned, these are the values given for one year of operation. For obtaining the values for the entire operational time, a factor of 10^3 has to be applied, which leads to

[2]The long-term values are given for one year of operation. Depending on the project's aim, the numbers must be multiplied with different factors to reach the dose over the project's entire lifetime.

[3]A factor of 10 is a conservative assumption as the Z mode will not be operating for this time-span. Assuming that the other operation modes are less severe for the positron production target, this factor is taken as an

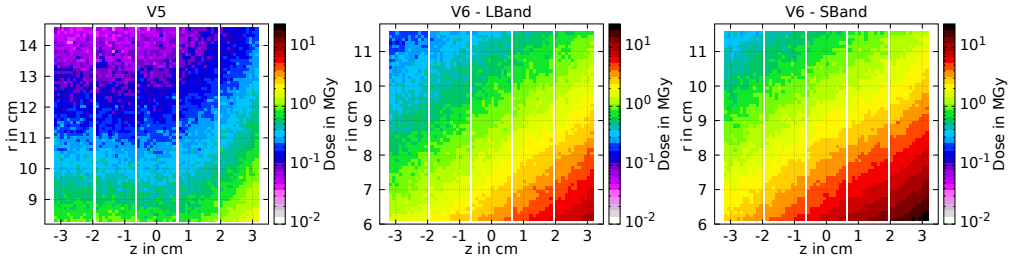

Fig. 4.12. Dose on the coils of (a) V5, (b) V6 L-Band and (c) V6 S-Band.

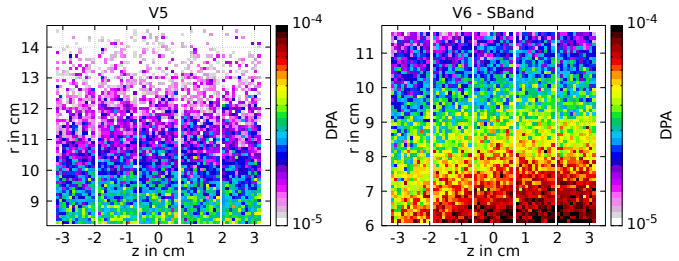

Fig. 4.13. DPA on the coils of (a) V5 and (b) V6 S-Band.

high values of up to 220 MGy in the coils for the S-Band version. Unlike low-temperature superconductors, no organic material, usually the showstopper, is foreseen in the HTS coils. Research must still be performed, but the obtained values possibly are acceptable for the YBCO tapes.

With an electron beam impacting the target, the DPA values on the coils are expected to be low as they are dominated by neutron interactions. The DPA in the coils of V5 is around 3-4 $\times 10^{-5}$ DPA, while it is around a factor 3 higher for the S-Band$_{\text{opt}}$ version of V6 (see Fig. 4.13). These levels suggest a DPA of around 1×10^{-3} DPA for the entire operational time, which should be feasible.

Pessimistic Scenario - Version 6

In the pessimistic scenario, the peak power density is found to be around 30 mW/cm^3 in Coil 5, as seen in Fig. 4.14, while in the optimistic version, the power density peaks at 16 mW/cm^3.

While the beam power differs by nearly a factor of 4, the peak power density is twice as high for the pessimistic case. This difference is due to the target position further downstream and the significantly thicker shielding in the pessimistic case. The farther

assumption for the entire operational time of FCC-ee.

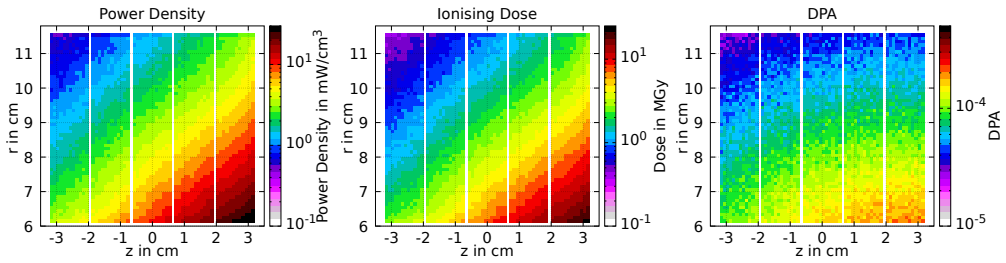

Fig. 4.14. (a) Power Density, (b) Dose and (c) DPA on the HTS coils using a 13.37 kW beam.

downstream target results in the shower development being moved downstream and, therefore, less impact on the coils. Using HTS coils is considered safe with the obtained values in the pessimistic and optimistic cases. Additionally, the strong gradient of power density in the coils supports heat transport and hence improves the situation of the coils even further.

The values of the long-term radiation effects are more delicate to understand. Generally, the dose distribution is identical to the power density distribution as the quantities are related. Up to 22 MGy/year are observed for the ionising dose, leading up to 220 MGy for the entire operational time. This dose value would be too high if superconducting coils with organic insulation were used as there is a threshold of 30 MGy. As mentioned, HTS coils free from organic materials are used in the AMD, most likely increasing the range of acceptable doses. Again, the question about the dose limit for the actual HTS coils appears, where no clear values could be found in the literature. Further research for the thresholds has to be performed.

This DPA distribution looks different to the dose and power density distribution, which is more evenly spread over the five coils. The DPA reaches up to 2×10^{-4} DPA/year, leading up to 2×10^{-3} DPA for the entire operational time. It has to be assured that these values are feasible.

4.2.6 | Summary of the Energy Deposition for the Optimistic and the Pessimistic Case

The energy deposition studies were performed for two different beam parameter sets, the optimistic (3.34 kW) and the pessimistic (13.37 kW) case. Furthermore, several versions of the geometry (V5, V6 S-Band$_{opt}$, V6 S-Band$_{pess}$, and V6 L-Band) were analysed to see the impact of different shielding thicknesses, longitudinal target placements, and radial coil locations.

The heat load and power density on the AMD and target were studied for instantaneous effects. The total power that can be translated to the heat load is assumed to be acceptable in all cases. The use of HTS coils can withstand the power density values that are obtained in all versions. However, the peak power density value seen on

the downstream face of the target for the pessimistic beam parameters is critically high, considering the location of the peak that makes cooling challenging.

Regarding long-term effects, the ionising dose and the DPA were investigated. In the case of the pessimistic beam parameter set, up to 8 DPA/year are reached in the target, which is too high to sustain and would require several changes of the target per year. The DPA is acceptable in the solenoid coils of the AMD. The ionising dose is particularly high on the HTS coils, as it can lead to the degradation of organic material. The most significant differences between the various geometries were seen in the coils. As expected, a location further outside and thicker shielding reduces the impact on the dose. Generally, the furthest downstream coil has the highest dose load, as it is impacted by the particle shower generated in the target. Therefore, the longitudinal placement of the target is also crucial, as a location further downstream decreases the maximum dose on the coils. In the pessimistic case, up to 22 MGy/year are obtained on the coils, which leads to extreme values for the full operational time. As HTS is still a new technology, research has to be done to evaluate the thresholds for the onset of material degradation.

4.3 Radiation Load Studies for the Positron Linac

The second part of the positron production source section is the positron linac, which captures the positrons and creates a bunched beam before the particles enter the damping ring (DR)[38]. This thesis investigates the first part of this accelerating structure, as possibly high power losses are expected from the particles entering the RF cavities with a large angular spread. The RF structure is surrounded by a normal-conducting solenoid, which provides a magnetic field of 0.5 T to focus the positrons in the forward direction[143].

In an RF structure, a time-dependent electric field accelerates the particles. With this electric field and the magnetic field from the solenoid, two fields impact the particles moving through the RF structure. However, in FLUKA, it is not possible to implement a magnetic field at the same time as an electric field, which is necessary for an accurate design of the FCC-ee positron source setup. Before performing power deposition studies, evaluating how much the electric field impacts the energy deposition results is essential.

4.3.1 | Layout and FLUKA Model

The positron linac is located 26.6 cm downstream of the peak magnetic field downstream of the AMD, which leads to a 16 cm gap between the AMD and the RF structure.

The RF structure comprises five similar cells with 44 cavities and a beam pipe radius of 3 cm (see Fig. 4.15). Each cavity has a length of 6.75 cm and a maximal radius of 6.5 cm. [4] The length of one cell is 324 cm, with the cavities taking up 297 cm, which leaves 13.5 cm of drift space on each side of the cavities. The complete capture linac has a length of 16.2 m.[28, 144, 145]

Copper waveguides pointing in the vertical direction are implemented at each cell's first and last cavity, with a thickness of 2 mm. The waveguides are filled with a vacuum, similar to the cells and the vacuum chambers. Vacuum chambers with a thickness of 2 mm are present as connections between the cells.

Outside the RF structure, the solenoids provide a magnetic field in the longitudinal direction, focusing the positrons that have a large angular spread when entering the capture linac. At the same time, the positrons are accelerated to 200 MeV in the capture linac.

The current baseline foresees a long solenoid of 221.4 cm length for each cell to cover the cavities. Like the short solenoids, the long solenoid is located at a radial position of 13 cm. The long solenoids extend 16.2 cm to the outside, and the short ones 27 cm. These short solenoids have a length of 20 cm, placed left and right of the long solenoid while covering cavities. An additional short solenoid is placed around the flanges between

[4] Creating the torus of a cavity is a challenging task in FLUKA since no equivalent body exists in FLUKA. The best solution to approximate this particular shape is to use truncated cones. For this linac, the circular shape was approximated with seven truncated cones on each side of the centre, with a cylinder for the central part. The measures of the truncated cones were obtained using the coordinates of a perfect circle. The truncated cones overlap and cut apart with vertical planes to reduce accuracy issues at boundaries.

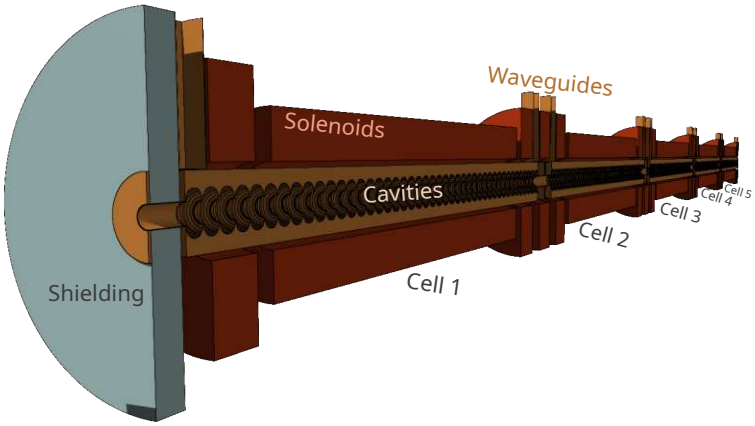

Fig. 4.15. 3D model of the capture linac, where the particles enter from the left side. The grey plate is the tungsten shield. The red cylinders enclosing the cells are the solenoids, and the rectangular shapes pointing in the vertical direction are the waveguides.

two cells to minimise the effect of magnetic fringe fields. For the FLUKA simulations, a tungsten shielding is implemented around the first flange that connects the vacuum chamber from the AMD with the capture linac.

The solenoids are made from copper, but in FLUKA, the material density is slightly adapted to account for the actual structure of the solenoids, which are wound cables with water-cooling holes. The cables have side lengths of 8 mm with a circular space for the water cooling with a diameter of 3.5 mm.[145] Implementing the correct material density is crucial as the energy deposition properties depend strongly on the material density.

The tungsten shielding is implemented in FLUKA, anticipating substantial energy deposition in the first cell. The shielding is directly attached to the vacuum chamber and ranges from 3.2 cm to 50 cm. Longitudinally, it extends 10.55 cm downstream from 27.6 cm downstream of the peak magnetic field in the AMD. A shielding with these dimensions covers the whole space between the first flange and the waveguide on the first cell. This implementation of the shielding is only used as proof of concept since, in a realistic design, gaps are necessary for the mechanical design.

The RF structure is combined with the AMD to simulate the entire geometry in one step. In this set of simulations, the pessimistic set of beam parameters is used, and the according geometry of V6 S-Band$_{\text{pess}}$ geometry of the AMD is implemented. The shielding in the AMD downstream of the target extends from a radius of 2 cm to the outside. The target exit is at a longitudinal position of 35 mm downstream of the maximum magnetic field strength value. As discussed previously, the target and shielding are pure tungsten and one piece, which facilitates the cooling.

In the space between the AMD and the RF structure, the vacuum chamber has a radius of 3.4 cm and a thickness of 1 mm.

4.3.2 | Particle Losses in the Linac - FLUKA vs RF Track

The characteristic feature of the positron linac is the co-existing electrical and magnetic field. This setup leads to several challenges in FLUKA. Firstly, it is highly cumbersome to implement a time-dependent electric field, which is the case for the positron linac. Furthermore, it is presently not possible to have two types of fields in the same simulation, which would be necessary with the solenoid field and electric field. With these restrictions, the FLUKA simulation is left with the constant 0.5 T solenoid field missing the time-dependent electric field.

It has to be evaluated if FLUKA simulations, where no electric field is present, provide representative results. If not, multi-step simulations collaborating with the RF group would be necessary, where RF Track[146] is used to accurately track the particles with a magnetic and electrical field. As this tracking tool cannot evaluate the energy deposition and heat load, FLUKA simulations are inevitable[132].

This type of simulation is used to compare the impacting power, which must not be confused with the deposited energy in the components. As soon as a particle touches the copper cavity, leaving the vacuum region, it is dumped. A user-routine routine retrieves particle information, including energy, type, and position, and saves it in an ASCII file. The power distribution can be understood from this file.

The present particles are photons, electrons and positrons. The minuscule amount of other particles, such as neutrons, is neglected. The photon power distribution is expected to be similar for all simulations and codes as they are not impacted by any field. However, these fields affect the movement of charged particles, like electrons and positrons, which makes it necessary to study the power loss on the cavities for the different setups. Three configurations are tested, with two configurations in FLUKA, with and without solenoid field, and one RF Track simulation, including both fields.

	Electrons		**Positrons**		**Photons**		**Total**	
	No MF	MF	No MF	MF	No MF	MF	No MF	MF
Total	1536W	1126W	1467W	1061W	4815W	4822W	7829W	7015W
Cell 1	1457W	1026W	1380W	967W	3719W	3721W	6564W	5721W
Cell 2	58.2W	71W	63.5W	62.8W	616W	607W	737W	741W
Cell 3	12.8W	16W	15.4W	19.7W	263W	261W	291W	297W
Cell 4	5.1W	9.1W	5.5W	6.6W	125W	148W	146W	163W
Cell 5	3.1W	3.4W	0.8W	4.1W	91W	83W	91W	90W

Table 4.8. Dumped Power in the RF structure: FLUKA dump simulation data comparing simulations without a magnetic field (MF) and simulations with a magnetic field of 0.5 T implemented. The row named "Total" takes all the dumped power into account.

Table 4.8 compares the power loss for the FLUKA simulations with and without a magnetic field implemented. Next to the total numbers, a detailed breakdown for each particle species and cell is given. All numbers are normalised for the pessimistic case of

V6, meaning a beam power of 13.34 kW.

The power distribution for the photons is similar for both cases, as expected. The impact on the first cell with about 3.7 kW is more than six times higher than the power on the second cell and magnitudes higher than on cells 3-5. The first cell takes around 77% of the power deposited on the positron linac by photons, regardless of the field.

For electrons and positrons, the magnetic field impacts the power loss distribution. The impact on cells 2-5 is relatively similar, but significant differences are visible for cell 1. Without a magnetic field, around 1.4 times more power is lost on the first cell due to the lack of the forward-directing field that focuses the particles. Therefore, the particles have a larger angular spread and are easier lost on the cavities. The difference in power loss caused by electrons and positrons also shows in the total power lost on the RF structure, which is around 12% higher if no magnetic field is implemented. Around 58% of the initial beam power of 13.34 kW is lost on the RF structure.

	Electrons		**Positrons**		**Photons**		**Total**	
	RF Track	FLUKA	RF Track	FLUKA	RF Track	FLUKA	RF Track	FLUKA
Total	1154 W	1126 W	1037 W	1061 W	4830 W	4822 W	7021 W	7015 W
Cell 1	1015 W	1026 W	913 W	967 W	3722 W	3721 W	5650 W	5721 W
Cell 2	84.96 W	71 W	79.5 W	62.8 W	631 W	607 W	796 W	741 W
Cell 3	24.2 W	16 W	23.5 W	19.7 W	265 W	261 W	313 W	297 W
Cell 4	21.23 W	9.1 W	12.8 W	6.6 W	140 W	148 W	174 W	163 W
Cell 5	8.8 W	3.4 W	7.9 W	4.1 W	71 W	83 W	88 W	90 W

Table 4.9. Dumped Power in the RF structure: FLUKA dump simulation data with the magnetic field set at 0.5 T comparing the data received from RF Track. The row named "Total" takes all the dumped power into account.

Table 4.9 compares the power losses from the FLUKA simulation with a magnetic field and the data provided by RF Track. This comparison aims to understand how the time-dependent electric field impacts the power loss of the particles in the positron linac. Again, the power loss for the photons is almost identical for both cases. Furthermore, it shows that the electric field considered in RF track does not significantly impact the power loss of the charged particles. The agreement of the data is beneficial, as this leads to the conclusion that a simple FLUKA simulation can provide reliable results and no multi-step simulations are required.

For a final check, the Fluka and RF Track data is plotted as a histogram (see Fig. 4.16), which gives a longitudinal resolution to the deposited power. The plot on the left side shows an overview of the total length, including all three particle types. The data agree well, except for the peak at the end, where the power leaving the RF structure downstream is given for the Fluka simulation but not for RF track. This spike is not included in the Tables 4.8 and 4.9, so obtain comparable values for both codes, FLUKA and RFTrack.

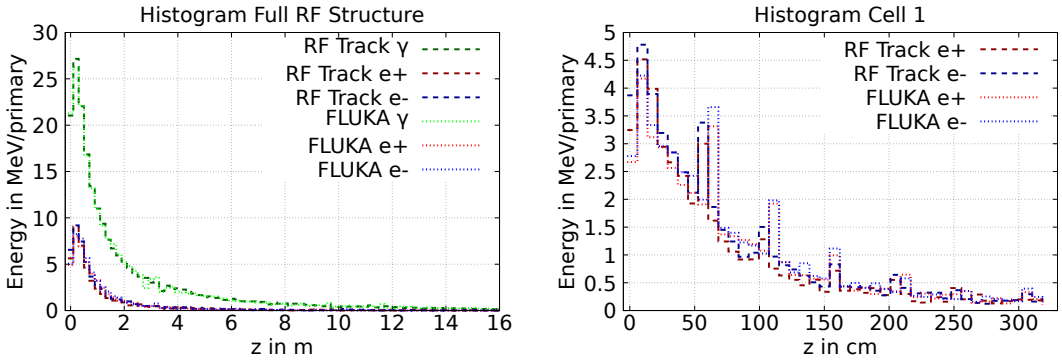

(a) **(b)**

Fig. 4.16. Energy histogram for (a) the full RF structure and (b) the first cell of the RF structure, showing the contributions from the different particles in different simulation setups. Taking the whole geometry of AMD and RF structure into account, the RF structure would start at a z of 26.6 cm, but for simplicity reasons, in these histograms, $z = 0$ is set at the entrance of the RF structure.

The histogram on the right shows the power loss of the electrons and positrons in the first cell. As previously discussed, the power loss is in good agreement, which these histograms support. This data confirms the approach of using standalone FLUKA simulations for the energy deposition studies.

4.3.3 | Energy deposition in the RF structure

Having confirmed that the FLUKA simulations provide loss patterns for the positron linac, energy deposition can be studied. Two different cavity designs are under investigation, with the cavities extending radially to 7 cm [144] and 11 cm[147], respectively. Thinner cavities do not absorb as much power, but thicker cavities provide a better shielding effect for the solenoids located radially at 13 cm. A cylindrical, 10.5 cm long tungsten shielding is placed upstream of the first cell to protect the linac[5]. Except for the shielding, which was only designed in FLUKA, the other geometry was designed by the RF groups of CERN and PSI.

The discussion of the energy distribution will follow a similar pattern as in the previous AMD chapter. First, the total absorbed power by each element is discussed. Then, a detailed discussion of power density, ionising dose, and DPA follows for the first cell, which is the most impacted. The results are presented for the pessimistic beam power case of 13.34 kW. However, if the beam power changes but the geometry stays identical, the deposited energy scales linearly.

[5]Different shielding structures were initially implemented as well, but they are not discussed here as they did not prove to be more efficient.

Absorbed Power in the RF Structure

The total absorbed power is shown in Table 4.10. No significant difference is visible for the shielding and the flanges, as the cavity thickness does not impact these components because they are located further inside. The shielding absorbs more than 1 kW, which is significant, considering that the most energetic particles are close to the centre. This amount of power confirms that this shielding is necessary, as this power otherwise would impact the RF structure. The flange connecting the AMD with the RF structure absorbs around 140 W, which is substantial considering the small size. This heat load should be sustainable as this component is warm. The flanges connecting the different cells are less impacted the further downstream they are, ranging from 51.6 W to 3.6 W, a pattern visible for all the components of the RF structure.

The solenoids in this part of the machine are meant to be normal conducting magnets. Therefore, the situation is less critical compared to the solenoids in the AMD. The main contributors to the magnetic field are the large solenoids, where the first solenoid is the most impacted. For these components, a significant difference between the 7 cm and 11 cm thick cavities is visible, particularly in the first cell. For the thinner cells, the large solenoid absorbs 607 W, nearly an order of magnitude more power than for the thicker cavities (68 W). With this, it becomes evident that thicker cavities are preferable if the heat load per cavity is bearable, as cooling the coils is much easier at lower absorbed power. For the long coils downstream, the effect of the thicker coils is not as significant, as they absorb 12.66 W in the worst case.

For the short coils and the coils used in the space connecting two cells, the absorbed power differs by a maximum of a factor of 3, depending on the cavity thickness. It has to be remarked that in the case of the short solenoids, the second solenoid absorbs most as the shielding well protects the first one. However, the power numbers obtained on these components are easy to handle.

	7cm cells	**11cm cells**
Shield RF	1049 W	1070 W
Flanges AMD/RF	132 W	155 W
Flanges Cells	43 W-3.6 W	51.6 W-4.5 W
Solenoid short	68 W*-3.6 W	25 W*-1.9 W
Solenoid long	607 W-12.66 W	78.5 W-1.4 W
Solenoid connect	53 W-4.3 W	28.5 W-3.2 W

Table 4.10. Absorbed Power in the RF structure comparing two different thicknesses of the cells. The * refers to the fact that the highest value is obtained not at the first short solenoid but at the second one.

Next, the absorbed power on the cavities should be discussed. As there is a large gradient in the impact on the cavities (see Fig. 4.17), it is not suitable to give an average number, but the power load should be assessed individually for each cavity.

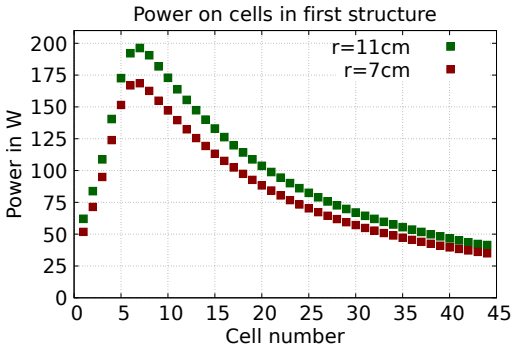

Fig. 4.17. Power on RF cavities in the first structure, comparing different radial extensions of the cells. The extension of the cell (7 cm or 11 cm), influences the radiation load on the solenoids further outside.

Up to cavity 7, the absorbed power per cavity rises strongly. This behaviour is explained by the shower still developing at the first cavity and reaching its maximum downstream around cavity 7. Within the distance of the first seven cavities, the power rises from 60 W/cavity to 200 W/cavity, assuming the thick cavities. A maximum of around 170 W is reached for the thinner cavities. These results are promising as even for the thicker cavities, the power does not exceed the RF power [148], and therefore, these numbers are sustainable, which should make them the new baseline. Further downstream, the power difference decreases for the two cavity thicknesses and can be found at around 40 W/cavity. In the cells downstream, the impact decreases even further.

Power Density, Ionising Dose and DPA in the RF Structure

After having elaborated the total absorbed power on the various parts of the capture linac, the discussion of the localised hotspots follows. Figure 4.18 shows the power density of the AMD and the whole RF structure. On the beam level ($r = 0$), hotspots can be seen at $z = 0$, where the target is located. For the cavities and the solenoids, it shows that the highest impact is on the first cells and then strongly declines. Due to this behaviour, only the impact on the first cell is explored in greater detail.

The particle shower coming from the AMD first impacts the flange connecting the AMD with the capture linac. A power density of 3.8 W/cm^3 is obtained in the hottest spot in the upstream corner. So far, no concerns have been raised regarding cooling, as copper is conducting heat well. If the power density is translated to the dose, 2800 MGy/year impact the flange. As the flange is purely inorganic, this value is acceptable. Around 1×10^{-3} DPA/year are seen on the same spot, which is also sustainable.

Further downstream, the cavities are heavily impacted, as discussed for the absorbed power. While the highest total power in the cavities is seen in cavity 7, the highest local values are obtained between cavities 2 and 3. These values are slightly higher than what is seen on the flange, 5 W/cm^3, 3500 MGy/year, and 1.2×10^{-3} DPA/year. Arguing the same

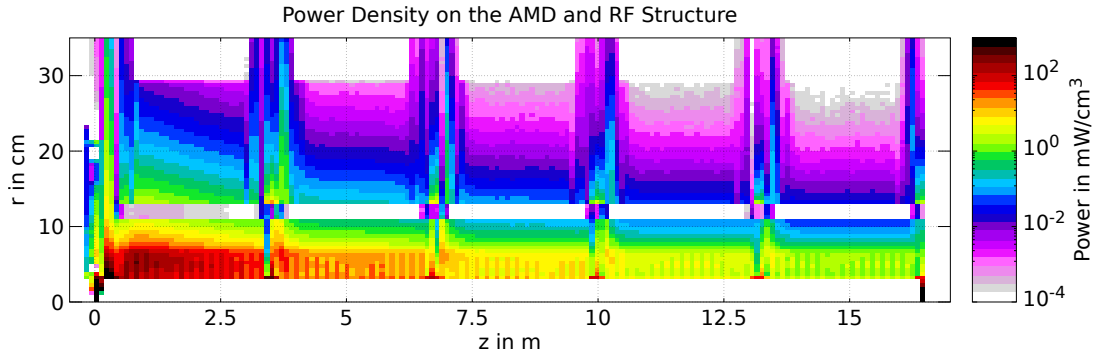

Fig. 4.18. Power Density on the AMD and the Capture Linac. A strong gradient from the first structure to the last structure is visible, so the first structure is a matter of interest for closer investigation.

way as it was just done previously, it can be concluded that the obtained power density and dose are feasible. If the DPA levels exceed a certain level, this leads to swelling of material and changes the shape of the cavity, which can influence the operation of an RF structure. It has been confirmed that the obtained DPA levels are viable[148].

For the discussion of the solenoids that enclose the cavities, one has to distinguish the 7 cm and 11 cm thick cavities. As seen in Fig. 4.19 and Fig. 4.20, the power density declines radically, moving further outside or downstream. Therefore, the worst impact is discussed, which is found around 100 cm downstream of the magnetic peak field in the AMD. This location is further downstream than the peak on the cavities, which the longitudinal component of the secondary particles can explain. These solenoids are normal conducting coils made from copper, with organic materials used as insulators. With reaching 250 mW/cm^3, 35 MGy/year, and 3.5×10^{-5} DPA/year in the case of the thin cavities, and 2.4 mW/cm^3, 2.8 MGy/year, and 1.2×10^{-5} DPA/year for the thicker cavities, the obtained values are acceptable for second. The thicker cavities shield the solenoids more efficiently, which leads to significantly lower impact and facilitates cooling considerably. Therefore, the latter solution is preferred.

Finally, it should be remarked that the hot spot of the dose in the connecting solenoid (65 MGy for 7 cm, 50 MGy for 11 cm) is due to the geometry design, which lacks shielding in this specific location. It was assured that in the final design, additional material would be placed there to protect the solenoids, so this value should eventually be acceptable.

Finally, it can be stated that the energy deposition results obtained on the positron production capture linac are promising, and no showstoppers have been detected.

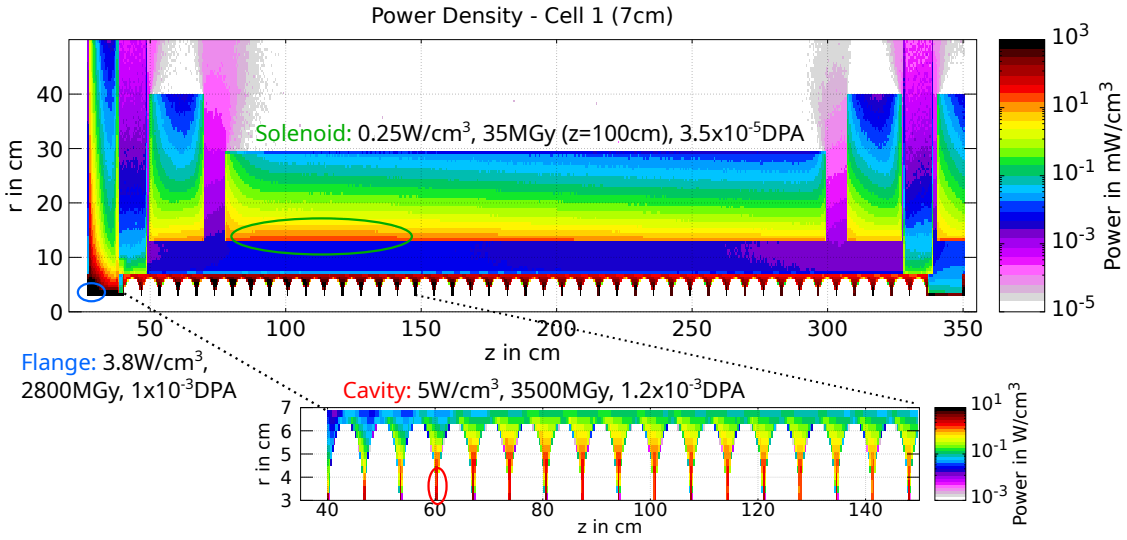

Fig. 4.19. Power on RF cells in first structure with 7 cm thick cavities. A different scale is used to amplify the peak. The values highlighted for the cavities and the flanges are also true for the 11 cm cavities.

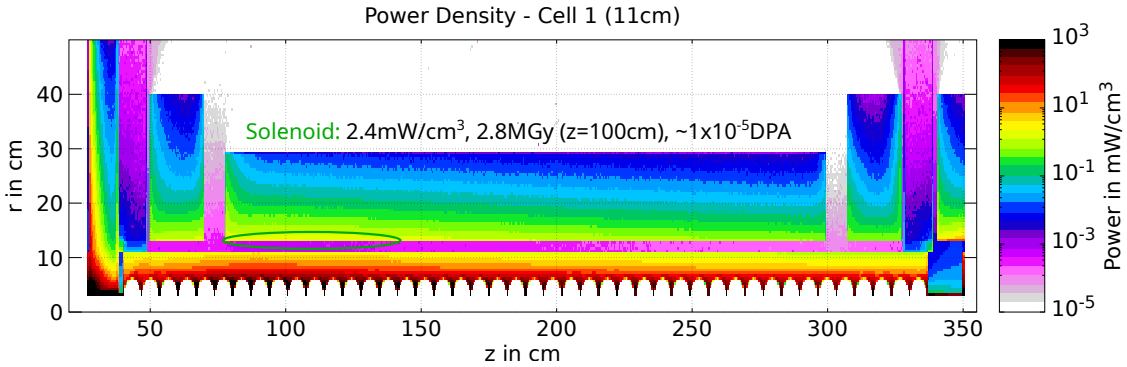

Fig. 4.20. Power on RF cells in first structure with 11 cm thick cavities. Comparing this plot with Fig. 4.19 that uses the same scale, the smaller impact on the solenoids is evident.

5

Fifth Chapter

Arcs

This chapter discusses the energy deposition on the FCC-ee arcs due to various physical processes. First, synchrotron radiation effects on the tunnel and the accelerator components are investigated for the $t\bar{t}$ mode. Later, beam-gas bremsstrahlung phenomena are studied, where the Z operation mode is more relevant.

Parts of this chapter have been presented in [149].

5.1 Synchrotron radiation

Synchrotron radiation (SR) is emitted by charged particles moving along a bent trajectory. As already discussed in Chapter 2, the energy loss per turn[56, Part IX] of a circulating particle is

$$\Delta E \propto \frac{E^4}{m_0^4 \rho}. \tag{5.1}$$

Therefore, SR is a severe problem for electron-positron colliders at high energies due to their low mass. A large machine radius (ρ =12.24 km[32]) decreases energy loss per turn and further the impact of SR on the machine. At FCC-ee, the energy loss per turn ranges from 0.031 GeV/turn for the Z operation mode at 45.6 GeV up to 8 GeV/turn at 182.5 GeV, the $t\bar{t}$ operation mode.

The critical energy, E_C, that splits the photon spectrum into two parts of equal deposited power is approximated by[150]

$$E_c[\text{MeV}] = 2.21 \cdot \frac{E^3[\text{GeV}]}{\rho[\text{km}]}, \tag{5.2}$$

leading to 1.1 MeV ($t\bar{t}$ mode) and 17 keV (Z mode), respectively. The operational energy differs by a factor of 4, while the difference in the critical energy is found at a factor of 65 (see Fig. 5.1). In the $t\bar{t}$ mode, half of the power is carried by photons with an energy higher than 1.25 MeV. When these photons interact with matter, they are in an energy range where the Compton effect is the main process, while for lower energy ranges, the photoelectric effect dominates (see Fig. 2.5).

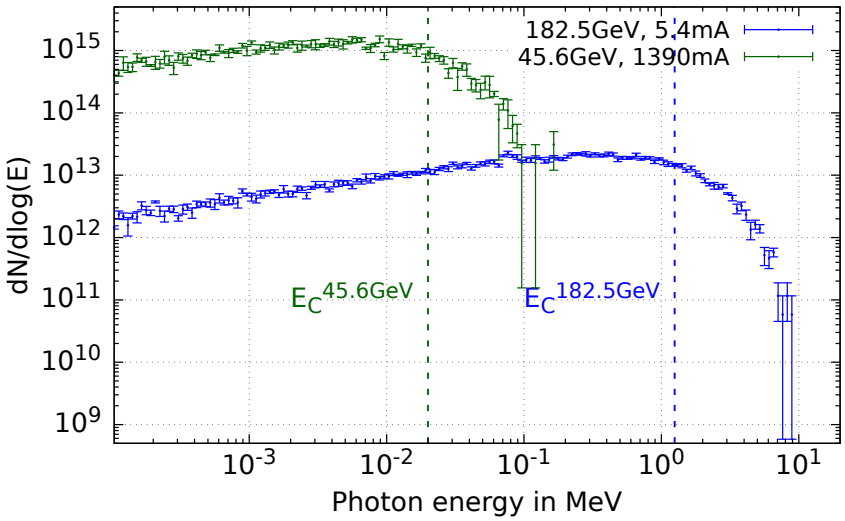

Fig. 5.1. SR Spectrum displayed for the highest and lowest energy operation mode. The vertical lines indicate the critical energy. (The same plot has been shown already in Chapter 2 but is used again here for educative reasons)

In FCC-ee, the emitted SR power is by design constant for all four operation modes at 50 MW/beam. The power is obtained with $P = \Delta E \cdot I$, which requires higher currents for lower beam energies and vice versa. This condition is achieved by using a current of 5.0 mA for the $t\bar{t}$ mode and a current of 1.28 A for the Z operation mode[1] [33]. Due to the higher beam currents, the achievable luminosity is higher for operation modes at lower energies.

5.1.1 | Simulation design

In this section, the simulation layout is established. The magnets of the beamline are introduced, and their placement along the arc is presented. Furthermore, the geometry and the peculiarities of the different photon absorber schemes are discussed.

A representative periodic arc cell of 141 m with two circulating beams, one for electrons and one for positrons, is implemented in FLUKA (see Fig. 5.2)[151]. The final

[1] Since the publication of the CDR these values are regularly changing. The SR power and beam energy are always held constant, but due to changes in the bending radius and hence the energy loss per turn in the FCC-ee arcs, the beam currents must be ajusted accordingly.

beam optics still needs to be established, so the energy deposition studies are performed with a representative cell that allows for assessing the general radiation load in the tunnel. At a later stage of the project, the precise cell shall be implemented, including all the critical systems.

The setup consists of five dipoles (MB), five quadrupoles (MQ) and four sextupoles (MS), with a beam separation of 30 cm. These are warm magnets operated at room temperature. The vacuum chambers (VC) are made out of copper and have a diameter of 7 cm with 2.5 cm long winglets attached on the sides, which should reduce the risk of back-scattered electrons interacting with the beam particles[152]. Copper is chosen as it is easy to manufacture and has favourable radiation absorption and vacuum properties.[29, 153]

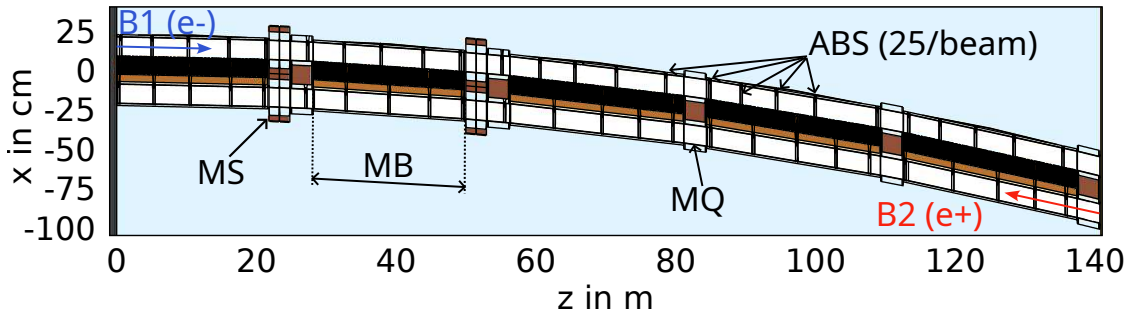

Fig. 5.2. Top view of the geometry at beam level with the different types of magnets indicated, as well as the beam directions and the absorber (ABS) placements. The first two dipoles are the longer ones, followed by the three shorter ones

The dipole (see Fig. 5.3) is implemented with two different lengths, namely 24.64 m for the long version and 21.44 m for the short version. The long version is used two times and the short one three times. Eventually, the long model was discarded due to a lack of mechanical stability and issues of transporting the magnet[154]. In the FLUKA simulation, both models were kept as no significant changes in the radiation load are expected on the tunnel and the magnet level.

The magnetic field is found at 56.6 mT for 182.5 GeV[24], provided through two iron plates acting as the yoke and copper busbars used as coils[155]. The top plate is mounted on the other plate with aluminium columns of a 10 cm diameter. These columns were the design baseline in the CDR, but eventually, this idea was discarded[156]. Continuous bars will be implemented instead, providing better mechanical stability. If simple copper busbars are implemented as coils, these components are expected to withstand high radiation load well due to the lack of organic material. However, if organic insulator material is inevitable, the coils are immediately much more prone to radiation damage. Due to the immense impact of the design, it should be decided at an early stage whether organic material is present or not.

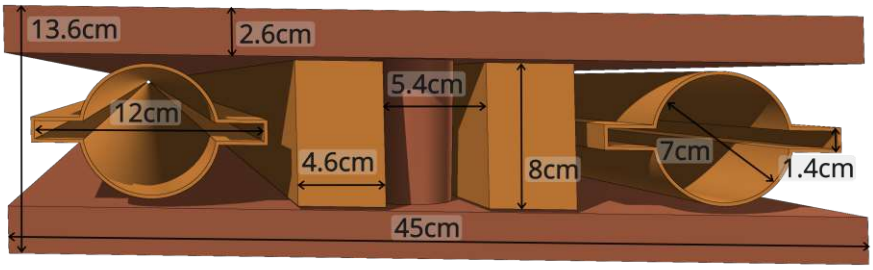

Fig. 5.3. Model of a dipole implemented in FLUKA. The top and the bottom plate form the yoke, held together by the columns. Next to the columns, there are copper busbars as coils. On the sides, the VC with the winglets is visible.

The quadrupoles (see Fig. 5.4) have a magnetic length of 2.9 m and a maximum gradient of 10.0 T/m. A generic quadrupole field is implemented in the simulations without considering the fringe fields. The model is symmetric around the x- and the y-axis, and a middle-spacer holds the upper and lower parts together.[155]

Similarly to the dipoles, the yoke is made of iron. The shape of the poles is optimised, so the yoke comes as close as possible to the vacuum chamber. Simultaneously, this leaves little space for possible shielding in the quadrupoles.

The four coils are located above and below the vacuum chambers. Furthermore, as SR is emitted tangentially, the location of the coils and the large amounts of iron around protect the coils from excessive radiation load. Prototypes for the dipoles and the quadrupoles have already been manufactured.[155]

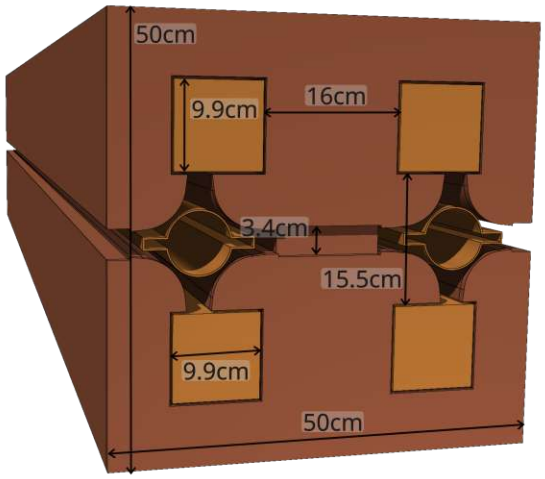

Fig. 5.4. Model of a quadrupole implemented in FLUKA. The vacuum chambers are surrounded by the yoke, which consists of a similar upper and lower part. The coils are located below and above the vacuum chamber and well protected by a large amount of iron from the yoke.

For the sextupoles, no technical drawing or prototype exists so far. The design (see Fig. 5.5) was implemented using half of a yoke-coil combination as seeh in the CDR[24] and extending it to the full sextupole by symmetric rotations and translations. Contrary to the MQ and MB, no coil endings are included for the 1.4 m long magnets. No magnetic field is implemented in the FLUKA simulation, as its effects on the energy deposition are expected to be minor. It is still relevant to include these magnets, as they absorb SR power emitted from magnets upstream and are therefore protecting magnets downstream. Furthermore, it has to be understood if the load on these magnets is sustainable. Four sextupoles are used, appearing in pairs after the first and the second dipole (see Fig. 5.2).

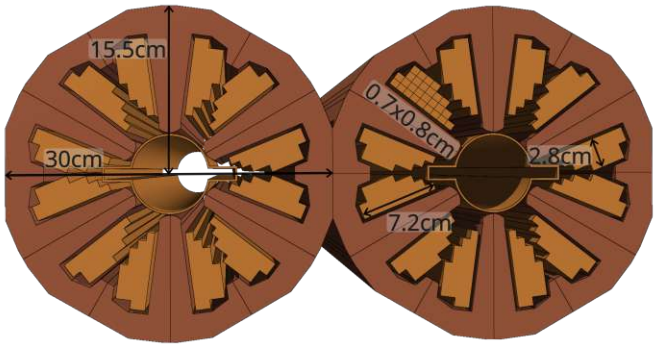

Fig. 5.5. Model of a sextupole implemented in FLUKA. The coils, which consist of 0.7 cm×0.8 cm wide copper strings, come particularly close to the vacuum chamber in the horizontal plane.

Shielding Design

Two different SR protection layouts were tested, one using the photon absorbers and another using continuous shielding. For the continuous shielding layout, extensive experience exists as this scheme was used for LEP[157]. The localised absorber scheme provides other advantages, such as lower material consumption and integrability in the vacuum system.

For the local photon absorber scheme, 25 absorbers per beam are placed along the 140 m long cell, which results in an absorber every 5 m-6 m. Placing the 30 cm long absorbers in such a manner, the SR fan is completely intercepted over the entire length of the arc[29]. Placing the absorbers in the dipoles, with few geometrical space restrictions, is uncomplicated. Up to five absorbers per beam are implemented in each dipole. In the MQ and MS, the space between the yoke, the coils and the VC is tight, which increases the difficulty of implementing an absorber there. Even if space was found, installing the vacuum chamber with the absorbers is significantly more straightforward in the dipoles due to the simple geometry and lateral accessibility. However, no solution could be found where the entire SR fan is covered by absorbers in the dipoles, which leads to a design

where one absorber per beam is found in the first two quadrupoles. Due to this fact, there are geometry restrictions in the absorber design.

The absorbers have angled surfaces to distribute the impacting power evenly (see Fig. 5.6/5.7). Due to the nature of SR, the highest impact is expected at $y = 0$, the beam level. The volume of the absorbers is limited by the yokes of the quadrupoles that come close to the winglets of the vacuum chamber, which leaves no room for larger absorbers. Larger absorbers could be envisaged if a placement solution is found where no absorbers are located in the quadrupoles. So far, using two different absorber sizes is discouraged due to increased complexity.

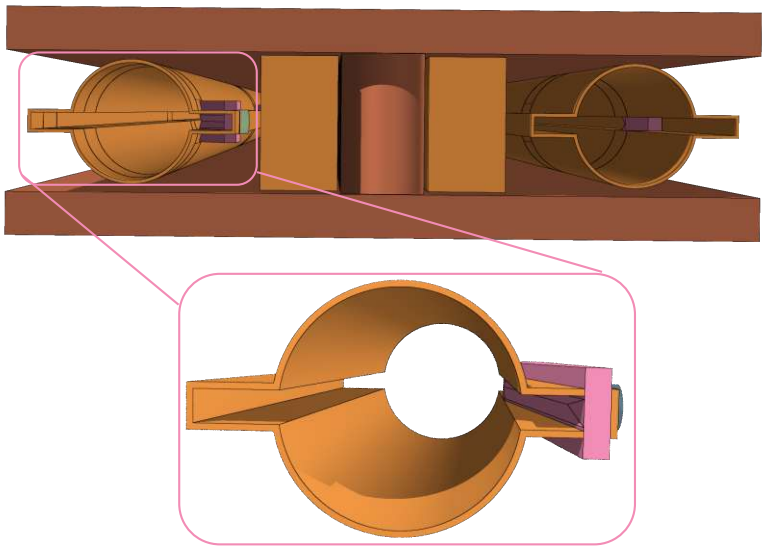

Fig. 5.6. The photon absorbers are located on the external winglet of the vacuum chamber. The surface moves closer to the beam under a small angle, so the impact is distributed over a longer distance. The water cooling will be attached to the external part of the absorber.

For the water-cooled absorbers, two different materials were tested. The first choice is a copper alloy, CuCrZr (Copper-Chromium-Zirconium), which is easy to manufacture[29]. These absorbers are heated substantially due to the SR, which makes good heat transfer properties essential, which is the case for CuCrZr as the VC consists of a similar material. Finally, CuCrZr has favourable properties in terms of vacuum desorption, which improves the vacuum quality.

Secondly, Inermet180®, a tungsten alloy well known for its excellent absorption properties, is used. However, manufacturing this brittle material is challenging. Additionally, the heat transfer in tungsten is less efficient, providing challenging cooling conditions. Finally, Inermet180® [158]is significantly more expensive than copper[159][2], which has to be considered with around 30,000 absorbers used in the entire machine.

[2]Next to the raw material cost, manufacturing is another big driver for cost, which is easier for a copper than a brittle material like tungsten.

The absorbers are designed in such a way that they do not enter the circular part of the vacuum chamber not to excessively increase the impedance. For the $t\bar{t}$ mode, photons in the MeV range carry a substantial amount of power and they undergo Compton scattering when interacting with the material. In this type of scattering, photons can be backscattered from the absorber surface. Depending on the internal or external beam, the backscattered particles impact the tunnel or the magnet, respectivley (see Fig. 5.7).

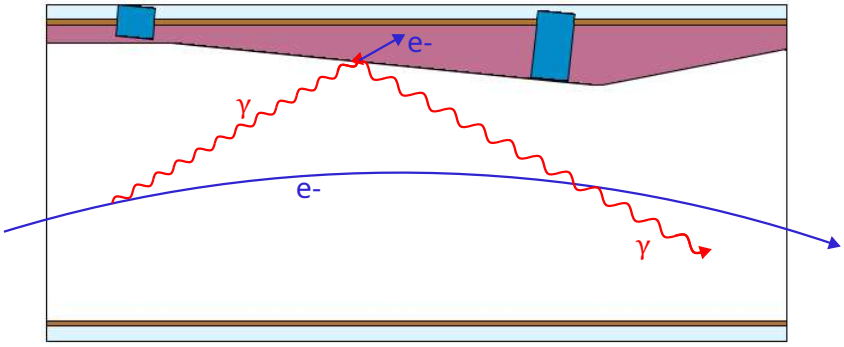

Fig. 5.7. Visualisation of the Compton scattering on the absorbers. A SR photon in the MeV range impacts the absorber, where it undergoes Compton scattering, which leads to the emission of an electron and a photon. The electron stays deposits its energy in the electron and the photon is backscattered. Depending on the internal or external beam, these photons impact the magnet or the tunnel environment. The two blue parts indicate cooling pipes.

The second absorption scheme is equivalent to the LEP shielding design. In LEP, a continuous layer of lead was attached to the vacuum chamber to absorb the SR[157]. For FCC-ee, a 1 cm Inermet180® layer was assumed to be attached externally to the winglets (see Fig. 5.8) in the dipoles. Compared to lead, its absorption properties are superior because of the larger density. Due to the tight design of the quadrupole and sextupole yokes and coils, these magnets have no space to install continuous shielding.

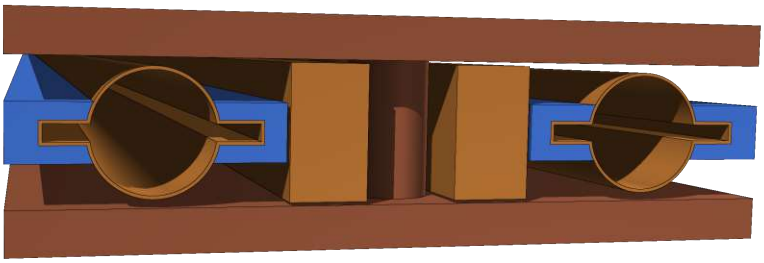

Fig. 5.8. The continuous shielding is attached to the outside of the winglet. It extends over the full length of the dipole and is maximised to come as close as possible to the dipole coils. No tungsten is added on the circular part of the VC, as the SR impact is highly concentrated in the horizontal plane.

The advantage of this system is that there is shielding on both winglets, reducing

the effects of backscattering and, therefore, lowering the radiation load in the tunnel. Furthermore, it is already an established technology. On the contrary, implementing continuous shielding around all the arcs would require several tons of costly tungsten, which is also a neutron source that induces to the activation of the material. Finally, the shielding is only present in the dipoles, which leads to high radiation impact in the locations of the other magnets.

This accelerator structure is embedded in a realistic tunnel geometry (see Fig. 5.9). As these are the first studies, only the layout and the collider are implemented in FLUKA. More details will be implemented later for in-depth studies of the radiation load on the different systems. In Fig. 5.9, (a) shows the tunnel layout, the main layout used for the FLUKA studies[24]. The collider is visible in the tunnel centre, with the booster ring on top of it. In the FLUKA version (c), no booster is included. Version (b) shows the most recent development in the Tunnel design (July 2023, [160]), where a concrete floor is added, creating a protected trench for the cables.

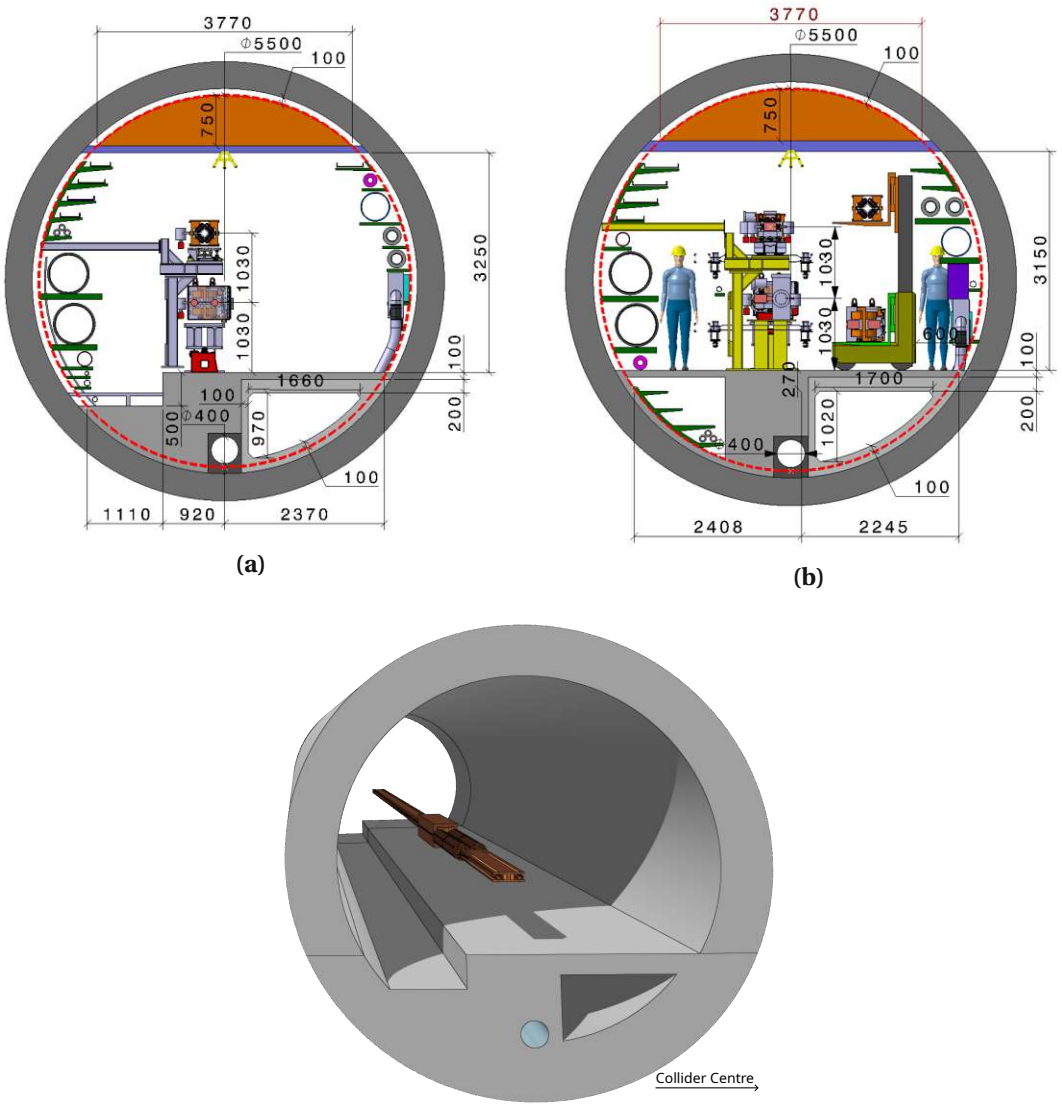

Fig. 5.9. Cross section of the tunnel design. (a) and (b) show the cross as it is received from the infrastructure group , (c) shows the implementation of (a) in FLUKA. So far, no other element than the collider is added to the FLUKA models as the general radiation load investigated. (a) is the cross section that was used for the majority of the studies, while (b) is a newer development, including a concrete floor below which there is a trench for cables. The graphics (a) and (b) are kindly offered from F. Valchkova-Georgieva.

5.1.2 | Simulation Methods & Settings

One of the challenges for this study has been to find an efficient and reliable way to simulate the effects of SR. Historically, FLUKA focuses on hadron machines, where SR is less crucial. Therefore, simulating SR was only possible when working with a special source card, which is a tedious process, as it is discussed in this section. Within the scope of this thesis, the simulation of SR in FLUKA has been substantially improved by colleagues in the section. The current version is more user-friendly and leads to higher accuracy of the physical results. An introduction is given to the underlying background of the SR sources.

Initially, a special source (SPECSOUR)[161] needed to be implemented in FLUKA to generate SR events in FLUKA. With this method, SR photons are randomly sampled along the dipole, and the resulting energy deposition is tracked. In the SPECSOUR card (see Fig. 5.10), the user indicates the beam energy, the particle type, the magnetic field strength and the magnetic length of the dipole. Furthermore, it is also possible to indicate the position and the angle of a second identical dipole that follows downstream. In one simulation, generating the SR showers from a maximum of two dipoles is possible. With the SPECSOUR approach, three simulations per beam are necessary to cover the entire representative FCC-ee cell. As two beams are present, six simulations are required for a complete evaluation of the line. The results of these six simulations must be merged in the post-processing, a lengthy and error-prone process. Furthermore, no SR is emitted in any other present magnetic field, like in quadrupoles, as with this method, only SR photons along dipoles are sampled.

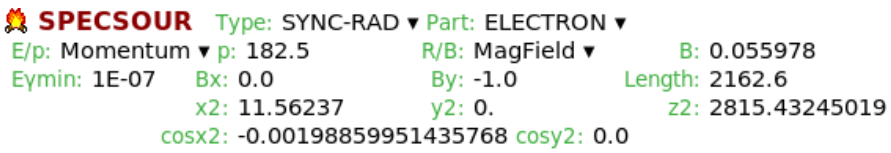

Fig. 5.10. Example of the source card (SPECSOUR) for creating SR photons in the first two dipoles of the line. As these two magnets must be identical and the dipole length must be identical. Additionally, the momentum and the photon production minimum energy (Eγmin) are valid for both magnets. In the fourth and fifth lines, the position and the angle of the second dipole are given, which is located further downstream, possibly with an angle if the beamline is bent.

Due to the several inconveniences that have just been discussed, the development of a new SR source for FLUKA was triggered. The beam is conventionally launched at the start of the line, and no special source card is needed with this new method. If the new SYRASTEP card[162] is included in the input file, charged particles moving through a magnetic field emit SR, covering all magnet types. The main advantage is the need for only one simulation per beam, which decreases the workload substantially while resulting in more reliable results. For this thesis, simulations were performed with both methods to validate the new method and establish any issues if there were any[3].

[3]As no significant issues could be found, the results presented in the following sections are obtained with the

In this thesis, the SR for the FCC-ee arcs is investigated, but implementing the full arcs into FLUKA is not efficient or practicable. The fact that the arcs are composed of FODO cells that are repeated periodically, is used to find a smart simulation setup. With this, good statistics can be achieved without time-consuming simulations.

In the case of the FCC-ee arcs, a strategy of a periodic cell where particles undergo reinsertion from the beginning as soon as they reach the end of the cell is chosen. The transformation in FLUKA is achieved by using a user routine (`usrmed.f`[107]). This routine is activated as soon as a particle reaches a pre-defined material. In this simulation, the region downstream[4] of the beamline has uniquely assigned gold. With this routine, the particles are brought back to the start of the cell with a transformation in the position and direction of the particle. The transformation includes a translation in longitudinal direction and a rotation of the direction, to align the particle with the position and direction of the tunnel at the cell entrance. If the energy of the particle touching gold is higher than a specific threshold energy (182 GeV in the case of the $t\bar{t}$ mode), the particle is dumped as it is the primary electron. Dumping the primary electron is justified, as the goal is to analyse the SR shower produced by going through the cell once. The secondary particles are tracked until they reach the low transport thresholds. Reinsertion is crucial for taking into account SR photons emitted far upstream of the cell under a low angle as these particles move far.

In the simulations for this study, the electrons are in the external beam moving clockwise, and the positrons move counter clockwise in the internal beam pipe. Considering the entire ring, the beams are crossing twice, and the length of the two trajectories is eventually the same.

The goal of the simulation is to achieve reliable results using the least time. Energy thresholds are introduced, below which particles are not tracked or produced anymore. These cuts are justified as the energy deposition contribution of these low-energy particles happens in reality within the desired spatial resolution. The transport (`EMF-CUT`) and the production (`PROD-CUT`) thresholds for electromagnetic particles are set at 1 keV for electrons and positrons, and at 100 eV for photons, which is the lowest possible in FLUKA[163]. For neutron studies, these electromagnetic thresholds are raised to 10 MeV for electrons and positrons and 1 MeV for photons. Neutron production is physically possible only above a given threshold depending on the material, being 2.2 MeV on its lowest value (Deuterium)[164]. Furthermore, in this case, the activation of the `PHOTONUC` card[165] is essential in FLUKA, allowing gamma interactions with nuclei.

FLUKA provides the energy density and dose values in units of GeV/cm^3 and GeV/g, per beam and primary, respectively. These values are normalised to W/cm^3 or MGy, using the beam current of 5.0 mA for the $t\bar{t}$ mode (182.5 GeV)[32]. For the long-term radiation

newer method.

[4] For the simulation of the positrons, where the beam moves in the opposite direction, the region next to the origin is assigned gold.

effects, the dose results are normalised to one year of operation, which is assumed to be 1×10^7 s or 116 days.

5.1.3 | Power Deposition on the Collider Elements

As stated in a previous part, 50 MW/beam are emitted due to SR for the full FCC-ee ring[24]. For a cell with a length of 140 m, 77.5 kW/beam are deposited, resulting in 155 kW for both beams. First, the absorbed power per element has to be understood. So far, it has always been stated that during the $t\bar{t}$ operation, the elements and components are impacted the most. Table 5.1 lists the absorbed power in the magnets for all four operation modes, where it shows that the total power is the same, which is expected as the SR power is constant for all operation modes.

While the total power is identical for all four operation modes, the distribution of the power varies strongly. The lower the energy of the operation mode, the more power is caught by the absorbers. For the Z operation mode, more than 99% of the SR power stays in the absorbers as the energy of the majority of impacting SR photons is below the Compton scattering threshold[59]. The remaining power is so little that no issues are expected for this operation mode. The same is most likely true for the W operation mode. However, as the values show for the H operation mode, still a significant amount of power escapes from the absorbers. Therefore, detailed studies could be beneficial to understand the impact.

	tt̄	**H**	**W**	**Z**
ABS	119.2 kW	127 kW	145.2 kW	154.6 kW
MB	22.5 kW	18.8 kW	7.14 kW	0.4 kW
MQ	2.45 kW	1.9 kW	0.7 kW	0.04 kW
MS	0.09 kW	0.05 kW	0.02 kW	0.002 kW
Tunnel	10.7 kW	7.2 kW	1.9 kW	0.02 kW
Total	155 kW	155 kW	155 kW	155 kW

Table 5.1. Absorbed power per element type for the different operation modes for the copper absorber layout. The most recent current values ([32]) are used.
($t\bar{t}$: 0.005 A; H: 0.0267 A; W: 0.135 A; Z: 1.28 A)

Table 5.2 shows the power going onto the different elements for the different layouts for the $t\bar{t}$ operation mode that has been studied in detail.

In all three cases, the same total amount of absorbed power is 155 kW, but the distribution of the power on the components differs. The tungsten[5] absorbers catch around 93% of the total power (143.8 kW). In contrast, the copper absorbers only catch 119.2 kW due to the worse absorption properties of copper. On average, an absorber catches 2.38 kW in the copper case and 2.88 kW in the tungsten case, assuming a total of 50 absorbers in the cell.

[5] In the following sections, the absorber material refers to the main component of the alloy. Therefore the CuCrZr absorbers are indicated as copper absorbers, while the Inermet180 absorbers are referred to as tungsten absorbers.

	Tungsten	Copper	Continuous
ABS or Shield	143.8 kW	119.2 kW	125 kW
MB	7.2 kW	22.5 kW	3.3 kW
MQ	0.8 kW	2.45 kW	16.2 kW
MS	0.05 kW	0.09 kW	6.7 kW
Tunnel	3.8 kW	10.7 kW	3.3 kW
Total	155 kW	155 kW	155 kW

Table 5.2. Absorbed power per element type for the $t\bar{t}$ operation mode with the different absorber (ABS) layouts and the continuous shielding (Shield). The first two columns show the data for the two different absorber material cases.

The continuous tungsten shielding catches 125 kW, which is slightly more than the copper absorbers. As copper has worse absorption properties but nearly absorbs the same amount of power as the tungsten-based continuous shielding, the better efficiency of the absorber layout is proven. Additionally, it has to be remarked, that of these 125 kW, 79.8 kW are absorbed by the vacuum chamber which is enclosed by the tungsten and the tungsten itself only absorbs 45.2 kW.

The dipoles are most impacted in the case of the copper absorbers, where they catch in total 22.5 kW, which is at 4.2 kW per short dipole and 4.75 kW per long dipole.[6] If tungsten absorbers are implemented, the power on the dipoles is significantly lower (7.2 kW), which is explained by the better absorption properties. In the case of the localised copper absorbers, more power is reflected back into the coils for the external beam. The lowest power on the dipoles is seen with the continuous shielding with about 3.3 kW. Here, the magnets profit from the shielding that encloses the winglets on the internal and external sides, effectively protecting the dipole coils from.

The power distribution concerning the quadrupoles is significantly different. The highest values are obtained for the quadrupoles in the continuous shielding case with 16.1 kW. In the case of the copper and tungsten absorbers, the quadrupoles are impacted by 2.45 kW and 0.8 kW, respectively. The significant difference originates from the fact that the localised absorbers cover by design the SR fan over the entire cell. Contrarily, the continuous shielding is only present in the dipoles and does not protect the quadrupoles and sextupoles. Due to geometrical restrictions, it is impossible to add continuous shielding to other magnet types than dipoles.

The same effect applies to the sextupoles. While the two absorber cases take 0.05 kW (tungsten) and 0.09 kW (copper), the sextupoles absorb 6.7 kW in the continuous shielding case. In the sextupoles, the space restrictions are even tighter, not allowing additional material to be inserted around the vacuum chamber.

[6] In this breakdown, the magnets include all components except the shielding (absorbers or continuous tungsten layer.).

Finally, the absorbed power on the tunnel structure has to be evaluated, which is of the same order of magnitude for all shielding schemes but with significant differences. In the continuous shielding case, the power is found at 3.2 kW, while it is at 3.8 kW for the tungsten absorbers and 10.7 kW for the copper absorbers.

The impact on the tunnel is higher for the localized scheme, especially for the copper absorbers. It has to be evaluated how the power is distributed along the tunnel and if additional mitigation measures must be implemented.

5.1.4 | Radiation Load on the Magnets and their Components

In a warm machine, like the FCC-ee arcs, the magnet components can sustain higher energy deposition levels than in a machine with superconducting magnets[59]. Evaluating the radiation load is still necessary to spot possible showstoppers especially for lifetime issues, and it allows a more profound understanding of the impact on the magnets and the surroundings.

This section is split into three parts, each focusing on a different quantity. First, the absorbed power on the magnet components is discussed, focusing on the benefits and disadvantages of the different setups. Then, the ionising dose impacting in the dipole coils is elaborated, followed by a discussion of the observed energy density in the vacuum chamber. The energy deposition is discussed for the copper absorber layout and the continuous shielding. The version using the localised tungsten absorbers had been discarded due to its disadvantages, mainly the higher cost for material and manufacturing, as well as the negative impacts on the vacuum quality. The continuous shielding is still kept as proof of concept.

Absorbed Power on the Magnet Components

As discussed in the previous section, the distribution of absorbed power differs between the layouts due to the different absorption properties of tungsten and copper and the geometrical differences. In the previous section, the absorbed power was discussed per magnet type. Here, the absorbed power on the different magnet components is presented.

The magnets have different lengths and sizes, so analysing the power per unit length is more insightful than the total power on the component.

For the dipoles, more than 139 W/m impact the yoke for the absorber case, while the yoke absorbs 23 W/m for the continuous shielding case. The same pattern is seen for the coils, but the difference is much smaller with 27.8 W/m and 9.2 W/m. At the level of the vacuum chamber, the the ratio is inverted. For the continuous shielding, the vacuum chamber catches 350 W/m and around 9.2 W/m for the absorber layout. It has to be evaluated if the vacuum chamber could sustain such high values as seen for the continuous shielding. Problematic outcomes could be the excessive outgassing from the vacuum chamber[166] or the mechanical deformation of the vacuum chamber if no suitable cool-

ing system is implemented[167]. Contrarily to the constant shielding, the absorbers are placed in the winglets inside the vacuum chamber (see Fig. 5.6). As mentioned, they are located in such a way that the absorbers catch all the SR fan. The continuous shielding is attached to the outside of the vacuum chamber. The copper vacuum chamber is not transparent for the photons, which leads to a significant absorption of the impacting energy. The constant shielding mounted on the outside of the vacuum chamber absorbs around 198 W/m[7]. So, the vacuum chamber has a substantial shielding effect.

The same behaviour of the power impact on the vacuum chamber is seen in the quadrupoles and sextupoles. Considering the data presented in the previous section, the energy deposition changes as expected in the yoke. When the continuous shielding scheme is implemented, the sextupole yoke catches 192 W/m and up to 338 W/m for the quadrupoles. The yoke is much less impacted if the localised absorbers are used, with 9 W/m for the MS and 12 W/m for the MQs without absorbers. In the MQs where absorbers are present, the power per unit length is found at 323 W/m, because of the backscattering of particles on the absorbers. These results prove the efficiency of the localised absorbers in protecting these magnets, even if no absorber is located in the MQs and MSs.

For the absorber scheme, the dipole coils absorb around 14 W/m, while it is found at 4.9 W/m for the continuous scheme. In the next section, it will be discussed, that the average value is not representative for the localised absorber scheme, as there are peaks with high power density that skew the average value.

The coils in the quadrupoles are only slightly impacted, due to the geometry of the quadrupoles, where the coils are far above and below the beam. Additionally, they are well protected by a thick layer of iron from the magnet yoke. In the continuous layout they absorb 6 W/m, while for the absorber scheme it is again necessary to have a distinction between the MQs that have an absorber (Power on coils: 17.8 W/m) and the ones without (Power on coils: 1.6 W/m).

In the case of the sextupoles, the power on the coils is much higher in the case of the continuous layout (231 W/m vs 4.6 W/m) as the coils are close to the vacuum chamber, nearly touching it. Due to the lack of shielding, the absorbed power is much higher in the continuous shielding case than in the localised absorber case, where the absorbers in the dipoles catch the SR photons that would impact the sextupoles.

Dose Levels on the Dipoles Coils

In this section, the dose levels on the dipole coils are established. Whatever shielding solution is chosen, the coils of the quadrupoles are considered to be safe. For the sextupoles, the dose levels on the coils are negligible if the localised absorber layout is chosen. The coils of the dipoles are exposed to high radiation load, which needs to be

[7] The total absorbed power for the continuous shielding case is obtained in this way:
$2(198\,\mathrm{W/m} + 350\,\mathrm{W/m}) \cdot (3 \cdot 24\,\mathrm{m} + 2 \cdot 21\,\mathrm{m}) * 10^{-3} = 125\,\mathrm{kW}$

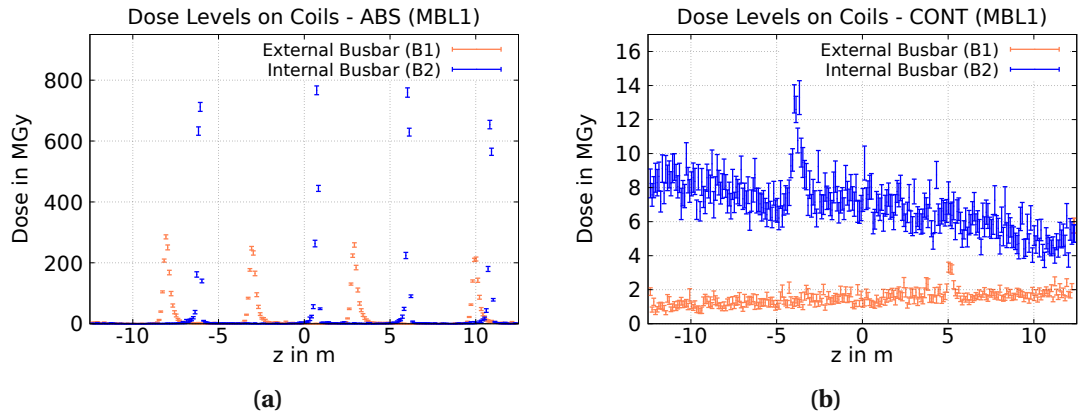

(a) **(b)**

Fig. 5.11. Dose levels on the dipole coils for (a) the copper absorber layout and (b) the continuous shielding considering 116 days of operation at $t\bar{t}$ mode. Mind the different scales on the y-axis, showing different orders of magnitude. The plots are produced for the MBL1 magnet, which is representative for all other magnets.

investigated more closely. So far, it is unclear which insulator material will be used and if it is organic.

For this part of the study, the coils are impacted mainly by the beam next to them. The contribution from the other beam is negligible, as the coils and the yokes in0between nearly entirely dampen the radiation load. The highest impact is always on the surface of the coils and the values given in this section are for one year of operation at $t\bar{t}$ mode.

In Fig. 5.11, the dose levels on the external and internal coils are compared. For the localised absorber scheme, strongly pronounced peaks are visible. These peaks are always found in the location of the absorbers in the corresponding beam. As the absorbers are not located in the same longitudinal positions, different positions for the peaks are obtained. Between the peaks of the absorbers, the dose levels fall below 1 MGy. Even, assuming a threshold of 30 MGy for current organic materials[109], the levels outside the peaks are sustainable for the entire runtime of FCC-ee.

The peaks, which reach 750 MGy for the internal coils and 250 MGy for the external coils, are not sustainable. Particle showers developing in the absorbers in the internal beam are causing the peaks on the internal coils. In contrast, the impact on the outside coil is due to backscattered particles from the absorbers. Further mitigation measures must be implemented to reduce the dose load. A possible solution could include additional localised shielding around the internal winglet for the external beam or attached to the absorber in case of the internal beam.

The dose maximum levels are much lower in the continuous scheme. Interestingly, the peaks are found slightly above and below the beam level. These peaks align well with the area where the continuous shielding is not present anymore, as it only covers the winglets. For the internal beam, the dose levels are found between 5 GeV and10 GeV.

The visible higher peak is due to the lack of shielding in the quadrupole upstream, which shows its effect further downstream the beamline. The dose levels are at about 1-2 GeV for the external beam, due to backscattered particles from the external shielding.

Energy Density on the Vacuum Chamber

Next, the power density on the vacuum chamber and the absorbers is discussed, a quantity essential for finding hot spots and assessing if cooling is possible.

As this quantity is closely related to the ionising dose, a similar pattern as in the previous section is observed. In the absorber layout, distinct peaks occur at the absorber positions with values up to 350 W/cm^3, but otherwise, low power densities in the range of 10 mW/cm^3 are seen. For the continuous shielding, a power density of around 30 W/cm^3 is obtained in the hottest spots.

Figure 5.12 shows the power density distribution for the different layouts. The hotspot in the localised absorber scheme is in the absorber at the beam level. This will require an effective cooling system, but generally, the heat transfer properties of copper alloys are suitable. Dedicated thermodynamic studies are still necessary to assess the severity of the issue and to develop the cooling system.

For the continuous shielding, the peak power density is obtained on the vacuum chamber, surrounded by the tungsten shielding. Tungsten has worse heat conductivity properties than copper[168], which makes cooling more of a challenge. The difficulty is increased by the brittleness of tungsten, which makes manipulating the material challenging.

Generally, the results of the localised absorber scheme are promising, especially considering that FCC-ee is a warm machine. As stated above, studies regarding the cooling system should be performed in the next step.

5.1.5 | Dose levels in the tunnel

In this section, the dose levels in the tunnel environment are evaluated. All three absorption schemes are examined for a complete overview of the situation. Additionally, due to the nature of SR, which is emitted tangentially at the beam level, an assessment of the vertical dose gradient is required.

First, the dose levels at the beam level are discussed (Fig. 5.13), where the highest values would naively be expected on the external side of the accelerator. However, a different behaviour is observed in the case of the localised absorbers, where higher dose values are obtained on the inside of the ring. As briefly discussed in the introduction to this chapter, this effect is caused by particles backscattering on the absorbers when undergoing Compton scattering. The backscattered particles impact the dipole coils for the external beam, while the impact is moved onto the tunnel environment for the internal beam due to the lack of shielding on the internal winglet.

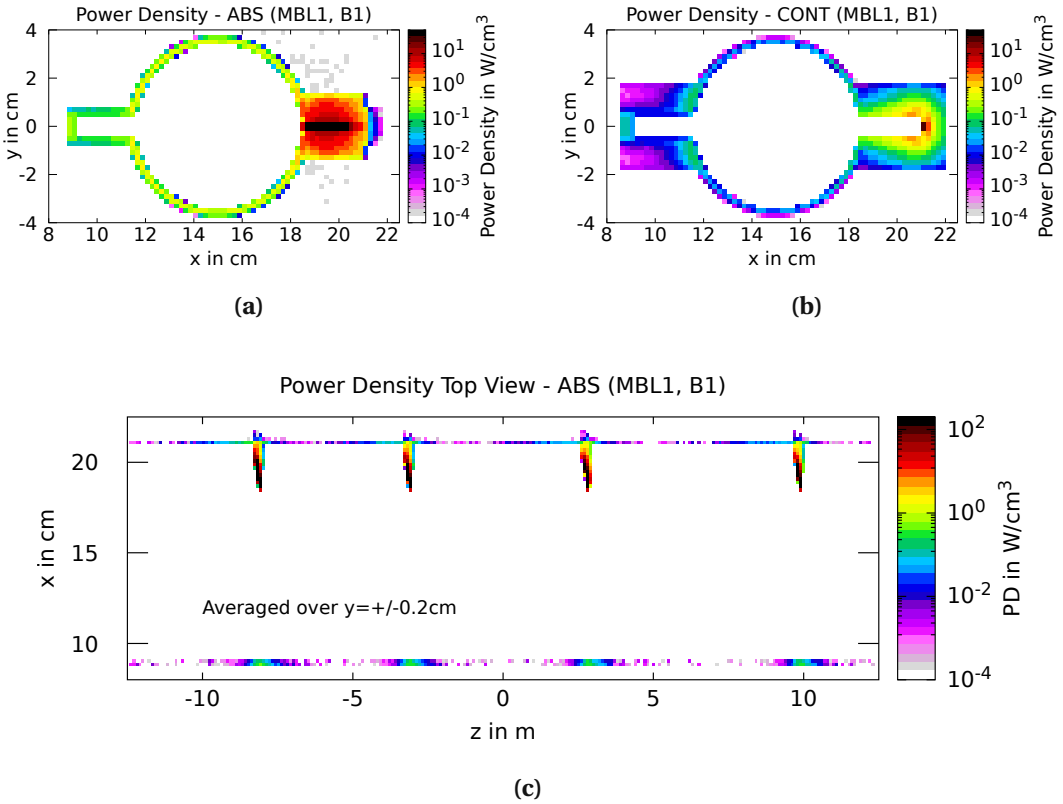

Fig. 5.12. Power Density on the VC and the absorber material for (a) the position of a localised absorber and (b) the continuous shielding. (c) shows the top view of the power density for the absorber layout at the beam level, where the large difference in power density between the areas with absorbers and the rest of the beamline becomes evident.

Internally, around 1 m next to the collider, the dose levels are at around 460 kGy for the tungsten absorbers and 930 kGy for the copper absorbers (see Table 5.3). On the outside of the collider ring, the difference between the values is relatively larger, where in the case of tungsten absorbers, 90 kGy are obtained, and 555 kGy for the copper absorbers. The better absorption properties of tungsten than copper lead to lower dose values in the tunnel, a quantity dominated by electromagnetic particles.

For the continuous scheme, the dose levels around the dipoles on the internal and external sides are similar at around 185 kGy. In the locations of the quadrupoles, high dose peaks up to 1.1 MGy are obtained due to the open space next to the winglets without shielding. If a continuous shielding scheme is foreseen, additional mitigation measures for the quadrupoles must be considered. The longitudinal dose distribution for the absorber layouts is more homogeneous, proving the efficiency of the scheme for the entire cell.

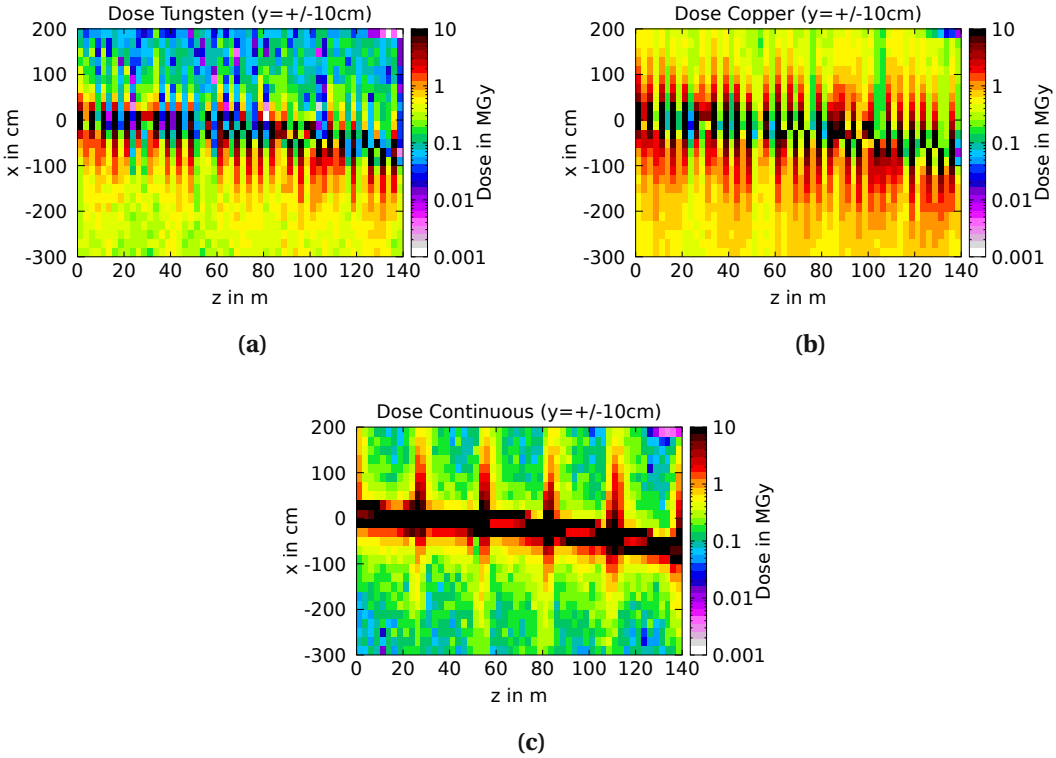

Fig. 5.13. Dose levels at the beam level for (a) Tungsten absorbers, (b) copper absorbers and (c) the continuous shielding (116 days, $t\bar{t}$ mode).

Now, the dose levels more than 1 m above the beam, where they are expected to be lower, are investigated. No major difference between the internal and external sides can be seen for all three cases, with the dose being rather homogeneously distributed (see Fig. 5.14). This behaviour is expected as no direct radiation reaches this region of the machine. The lowest values are obtained for the tungsten absorber case with around 90 kGy. As expected, higher dose levels are obtained for the copper absorber case, going up to 280 kGy. Two spots of lower dose are observed at around 30 m and 55 m, which are explained by the quadrupoles that include absorbers. The combination of the absorbers and the geometry of the quadrupoles, where the yoke comes close to the vacuum chamber, provides better protection than seen elsewhere.

In the continuous scheme, the average dose levels reach up to 110 kGy. Due to the lack of shielding in the five quadrupoles, an equal amount of spots with higher dose levels occur along the line.

These studies are a valuable asset in evaluating the optimal placement of the booster in the tunnel. So far, two options have been considered: either next to the collider on its inside or above it[169]. The first option was chosen as lower dose values were expected on the inside, which has been proven wrong in these studies. Preferably, the booster shall be mounted on top of the collider machine, as the lowest dose levels are obtained

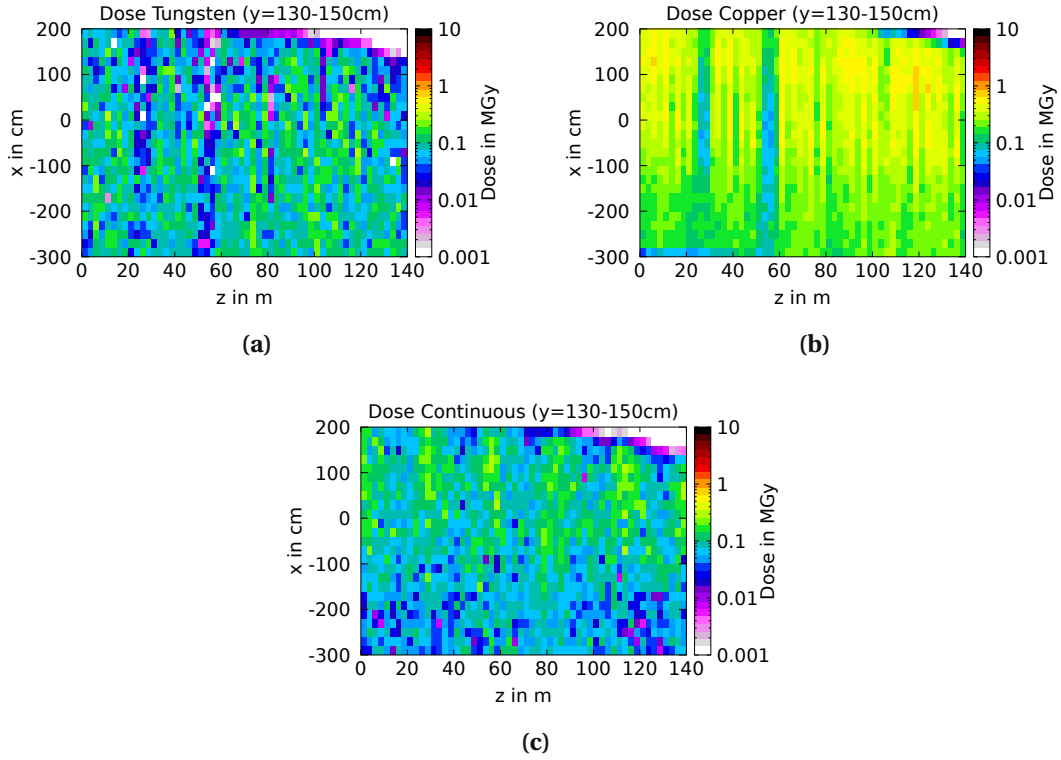

Fig. 5.14. Dose levels above beam level for (a) Tungsten absorbers, (b) copper absorbers and (c) the continuous shielding (116 days, $t\bar{t}$ mode).

there.[8]

	Tungsten	Copper	Continuous
Beam level, ext.	90 kGy	555 kGy	185 kGy
Beam level, int.	460 kGy	930 kGy	185 kGy
Above beam	90 kGy	280 kGy	110 kGy

Table 5.3. Annual dose levels in the tunnel for the different absorber schemes. For the beam level, data is given for the external (ext.) and internal (int.) sides of the collider around 1 m next to the collider ring (116 days, $t\bar{t}$ mode).

As an example, in HL-LHC, the reference R2E limit in the arcs is 1.4 Gy[110]. This discrepancy of several orders of magnitude indicates that the values obtained for FCC-ee are too high for any electronics to be installed in the tunnel at the current state. Therefore, further shielding in the tunnels is necessary to protect the electronics.

[8] In this thesis, the impact of the booster on the collider and the tunnel environment has not been studied. As the particles will reach the top energy in the booster, a dose contribution is also expected from this machine, critically depending on its operation time structure.

A new layout for the tunnel has been distributed towards the end of this thesis work. In the new layout, a trench is foreseen to be closed by a false floor made from concrete. In this trench cable trays should be placed. Preliminary studies have shown that this 10 cm layer of concrete reduces the ionising dose in the covered trench to a maximum of 60 kGy/year for the copper absorber layout. Regular cables usually can withstand a few 100 kGy[170], so the obtained dose levels are still too high if the cables should be kept in place for several years. However, sustainable dose values should be achievable with a slightly thicker concrete floor, adding around 2 cm of concrete but studies have to be performed.

5.1.6 | Neutron Equivalent Fluences

Next to the total ionising dose, neutron equivalent fluences are pivotal in assessing if a machine environment is sustainable for the electronics, as discussed in 3. Generally, due to the nature of leptons, a lower contribution in neutron-dominated effects is expected for FCC-ee compared to a hadron machine. Nevertheless, high beam energy and SR power require a thorough evaluation of the situation.

Three different equivalent fluences are evaluated: the Si-1MeV neutron equivalent fluence, the high energy hadron equivalent fluence, and the thermal neutron equivalent fluence. All these quantities are usually dominated by neutrons. For these simulations, the photonuclear reactions are activated the thresholds are raised to 1 MeV for photons, 10 MeV for electrons and positrons.

For the SR studies in FCC-ee, the Si-1MeV neutron equivalent fluence must also be evaluated for the purely electromagnetic contribution. It should be recalled that this quantity expresses the silicon damage potential of any radiation field in terms of the theoretical 1 MeV neutron fluence producing the same effect. The high abundance of electromagnetic particles eventually leads to notable Si-1MeV neutron equivalent fluences independently of the actual neutron contribution.

The obtained Si-1MeV neutron equivalent fluence levels are relatively similar in all three cases, in a range of several $1 \times 10^{12}\,\mathrm{cm}^{-2}$ per year of operation (see Fig. 5.15). While the total equivalent fluence is similar, the contribution of electrons and neutrons differs strongly in the three cases, depending on the absorber material.

For the copper absorbers, the electromagnetic contribution is much larger ($5.6 \times 10^{12}\,\mathrm{cm}^{-2}$) than the contribution from neutrons ($1.85 \times 10^{11}\,\mathrm{cm}^{-2}$). For copper, the threshold of neutron production is at a photon energy of 10 MeV[171]. In FCC-ee, the critical energy is at 1.2 MeV, and the photon spectrum decreases quickly for higher energies. Therefore, SR photons with energies higher than 10 MeV are scarce, which leads to a relatively low amount of neutrons that could impact the machine and its environment if copper shielding is used.

A shift in the ratio of neutron and electromagnetic contribution is observed for the tungsten absorbers due to the different neutron production threshold in the very material. The tungsten threshold energy for a photon being able to remove a neutron from the nucleus is found at 6-8 MeV, depending on the stable tungsten isotope. That values are significantly lower compared to the threshold of 10 MeV for copper. With the SR spectrum falling rapidly above the critical energy of 1.2 MeV, a moderate difference of 2-4 MeV in the production threshold leads to a significant difference in the amount of the produced neutrons. The electromagnetic contribution is well attenuated for the tungsten shielding schemes, unlike what is seen for the copper absorbers. However, summing up the neutron and the electromagnetic contribution, the same level is reached for all three versions.

For comparison, in HL-LHC[110], the values reach $1.5 \times 10^{10}\,\mathrm{cm}^{-2}$, which is significantly lower than what is obtained in FCC-ee. If the localised copper absorber layout is

assumed as the baseline, the obtained Si-1MeV neutron equivalent fluence values are still less concerning than what is observed for the total ionising dose. The electromagnetic contribution dominates both quantities, which leads to the conclusion that a reduction in the dose levels by several orders of magnitude will automatically decrease the Si-1MeV neutron equivalent fluence to a sustainable level.

Thermal neutrons are found on the lower end of the energy spectrum with a neutron energy of about 0.025 eV at 300 K[172]. The thermal neutron equivalent fluence, including the contribution of higher energy neutrons with a weight as their capture cross section ($\propto 1/v$), is homogeneous and at 2×10^{11} cm^{-2} for the copper absorber layout, only one order of magnitude higher than what is expected in HL-LHC (1.2×10^{10} cm^{-2}).

The high energy hadron equivalent fluence is lower in FCC-ee (copper absorbers: 0.9×10^{8} cm^{-2}, continuous shielding: 1.8×10^{8} cm^{-2}) than what in HL-LHC (2.4×10^{9} cm^{-2}). This difference is caused by the spectrum of the neutrons, which has much more energetic neutrons in HL-LHC compared to FCC-ee. Therefore, it will not pose a problem in FCC-ee.

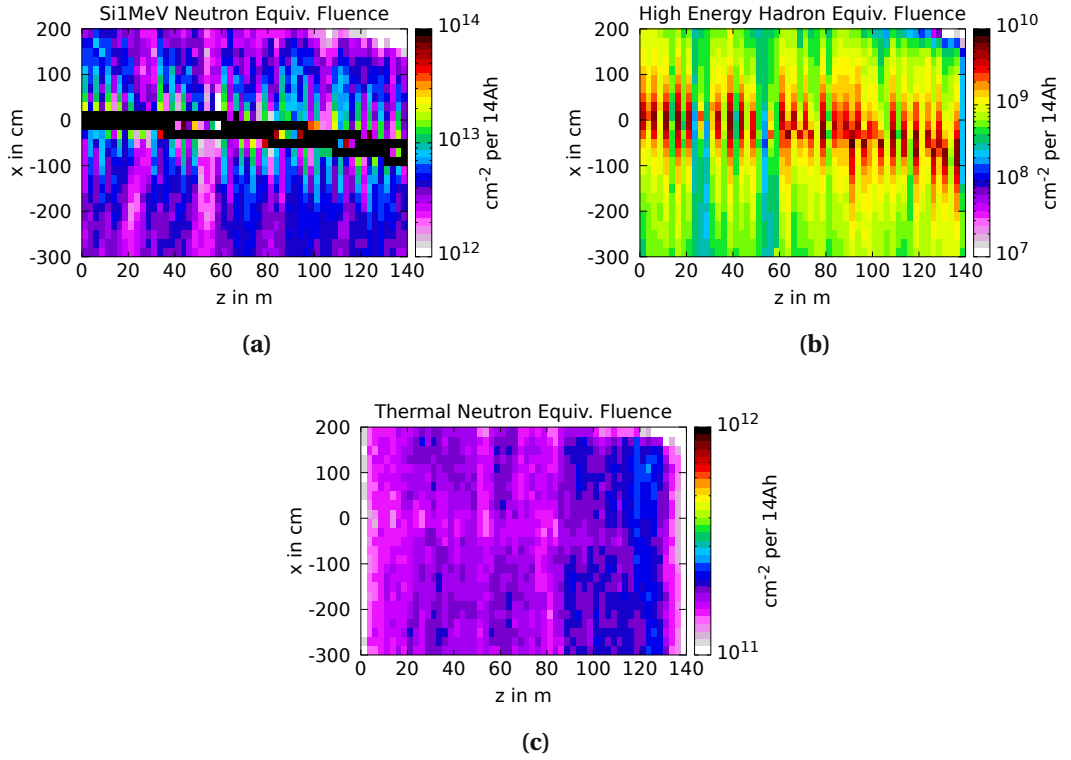

Fig. 5.15. Neutron and hadron equivalent fluences for the copper absorber case. The other shielding layouts result in similar levels and distributions. Therefore, only one set is shown, where the values are averaged over the full tunnel height and normalised to 116 days of operation at the $t\bar{t}$ mode. ((a) Si-1 MeV neutron equivalent fluence, (b) high energy hadron equivalent fluence and (c) thermal neutron equivalent fluence.)

5.1.7 | Electronics Shielding Scheme

As seen in the previous sections, the dose levels are too high for the electronics to withstand without getting damaged. Therefore, dedicated shielding for these delicate components is needed.

Typical shielding materials like concrete and lead[173] are tested, with different thicknesses, ranging from 1 cm over 3 cm to 10 cm. As these simulations are first and foremost conceptual studies, the location is chosen to be in the bottom corner of the tunnel as this is the place with the lowest dose levels. Furthermore, there could be room to install the electronic racks. These studies investigate how much shielding material is needed to achieve acceptable dose levels in critical places.

Particle spectra are used for determining the efficiency of the shielding in three different regions. Firstly, there is a region called "Tunnel", which is next to the collider on the external side (see Fig. 5.16). No physical equipment is placed there, but this location is used for having reference values. Another spectrum is scored in the shielding, and a last one is obtained in the region where the electronics would be placed.

In order to be comparable, the results obtained from FLUKA have to be normalised to the volume of the scoring region. Depending on the shielding thickness, changing the scoring region, different normalisation factors have to be applied. These simulations are performed for the localised copper absorber layout only to keep this part of the study concise.

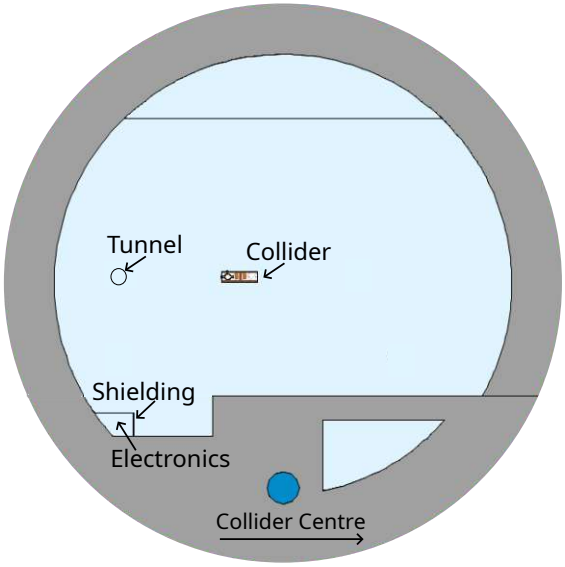

Fig. 5.16. Tunnel cross section for R2E simulations with different scoring regions indicated. The shielding has been implemented with three different thicknesses (1 cm, 3 cm and 10 cm) and for two materials (lead and concrete).

Spectra in Different (R2E) Regions

For the spectra, two different contributions must be considered: the electromagnetic contribution with electrons, positrons and photons and the contribution from neutrons. They are produced in different processes and impact the machine differently.

SR photons above 10 MeV produce MeV neutrons up to around 20 MeV in copper[171]. Some of these thermalise down to 0.025 eV (see Fig. 5.17). Generally, the magnets and shielding are transparent to the neutrons to a certain degree, which is observed for all types of implemented shielding. If the spectrum for different locations in the tunnel is compared, its order of magnitude is everywhere the same, including different shielding materials and thicknesses. In the high energy range, large statistical errors appear due to the low abundance of neutrons of this energy.

As only minor differences in the neutron spectrums are observed in various locations of the tunnel for the different materials and shielding thicknesses, it leads to the conclusion that this type of shielding is insufficient to protect the electronics from neutron damage. This result incentivises further studies to investigate more elaborate shielding designs that could provide a sustainable solution. An option could be to attach a few cm

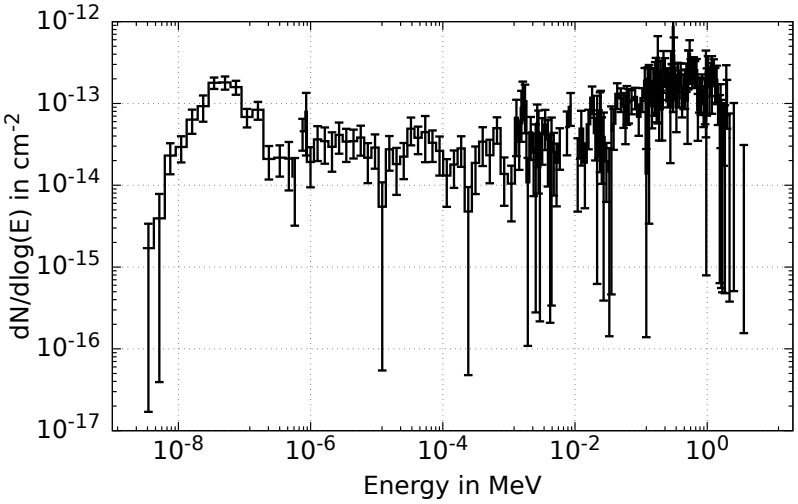

Fig. 5.17. Neutron spectrum in the FCC-ee due to SR 1 m next to the collider (116 days, $t\bar{t}$ operation mode).

thick layer of borated polyethene to the outside of the lead layer. As a hydrogenated material, it slows the neutrons down, which are then captured by boron[174]. This process generates photons that are then stopped in the lead layer that follows.

The shielding is efficient for electromagnetic particles, as shown in the following. Four particular cases are discussed, including the spectrum of the electrons moving through lead and concrete(see Fig. 5.18), and secondly, the spectra for the attenuation of photons (see Fig. 5.19). There are differences in the attenuation depending on the material and the particle type. For both, electrons and photons, the attenuation is more significant in lead than in concrete, comparing the same thicknesses.

For a 1 cm lead shielding, higher values in the low energy range are surprisingly visible in the shielding compared to the tunnel. This increase is likely caused by the photoelectric effect happening in the shielding layer. Less of the same effect can be seen for the 3 cm lead shielding. For the thickest lead shielding layer, the electron fluence values remain lower than in the tunnel at any energy. As foreseen, the spectra in the electronics region show a decrease with increasing shielding thickness. In the case of a 10 cm lead shielding, no spectrum is obtained in the electronics region as it is below statistics reach.

No significant attenuation is obtained for 1 cm of concrete shielding. Comparing the lead and the concrete spectra, one can see that the shielding efficiency is better for 3 cm of lead than for 10 cm of concrete.

The spectra for the photons are different from those for the electrons. The low-energy part is cut in the electronics region with the implemented shielding for both materials. The attenuation is once again significantly stronger for the lead shielding. The attenuation of the photons is at almost four orders of magnitude between the maximum

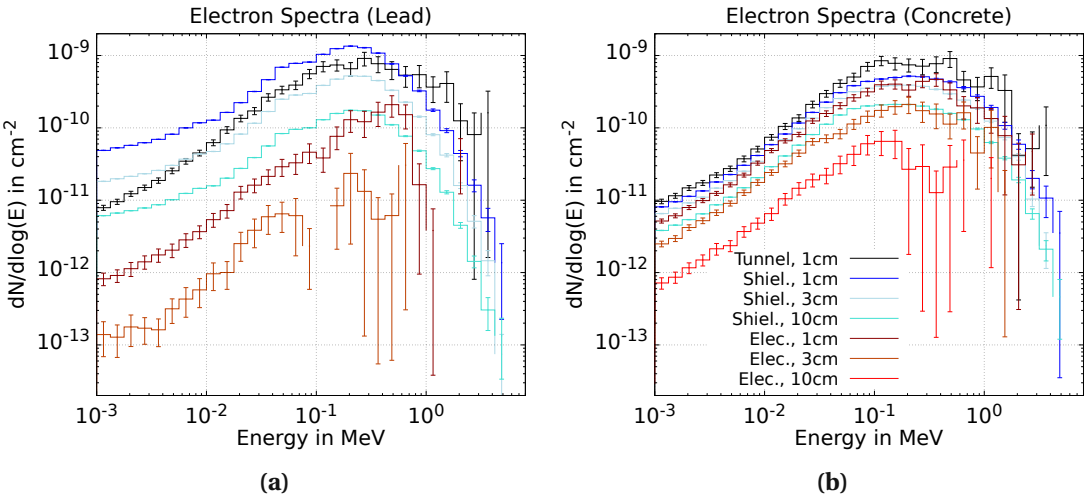

Fig. 5.18. Electron spectrum for (a) lead shielding and (b) concrete shielding. (116 days, $t\bar{t}$ operation mode)

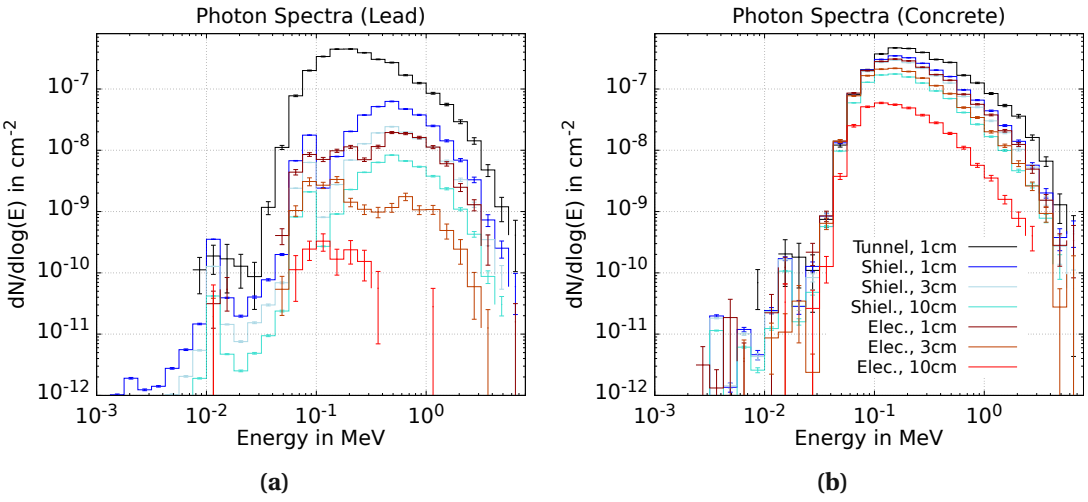

Fig. 5.19. Photon spectrum for (a) lead shielding and (b) concrete shielding. (116 days, $t\bar{t}$ operation mode)

in the tunnel and the minimum in the electronics region for 10 cm of lead. For the same thickness but using concrete instead of lead, in the spectrum decrease by only one order of magnitude.

R2E Levels in the Electronics Area

This section discusses the R2E values in the electronics area (see Table 5.4). The values were averaged over the volume of the electronics area over 15 m in z, and normalised to one year of operation at the $t\bar{t}$ mode.

LEAD	Dose	Si-1MeV	HeH	The. Neu
1 cm	92 kGy	2.8×10^{11} cm^{-2}	5×10^{7}–5×10^{8} cm^{-2}	2.1×10^{11} cm^{-2}
3 cm	46 kGy	9×10^{10} cm^{-2}	5×10^{7}–5×10^{8} cm^{-2}	1.9×10^{11} cm^{-2}
10 cm	<1 kGy	5×10^{8} cm^{-2}	5×10^{7}–5×10^{8} cm^{-2}	1.4×10^{11} cm^{-2}
CONCRETE				
10 cm	28 kGy	4.6×10^{10} cm^{-2}	5×10^{7}–5×10^{8} cm^{-2}	2.8×10^{11} cm^{-2}

Table 5.4. R2E Levels in the electronics area for 116 days of operation at $t\bar{t}$ operation mode. No values for 1 cm and 3 cm of concrete shielding are provided, as the shielding effect of these setups is negligible. The dose levels at this region in the tunnel, without any shielding is at 250 kGy (HeH ... High energy hadron equivalent fluence, The. Neu ... Thermal neutron equivalent fluence)

The ionising dose, mainly caused by the electromagnetic part, decreases significantly with increasing shielding thickness (see Table 5.4). This behaviour has already been observed in the spectra and is now confirmed. Lead is significantly more efficient than concrete, with no detectable dose for 10 cm of lead in the current simulation setup. Even aggressive biasing did not a dose evaluation in the case of the thick lead shielding. These results lead to the conclusion that this shielding thickness may be excessive and not needed. Additionally, implementing such a large amount of lead would not be approved due to the hazards of this material.

A shielding of 10 cm of concrete reduces the ionising dose to below 30 kGy if the shielding is placed in the bottom corner. This would be a promising improvement for cables, but it must decrease much further for electronics.

As stated in the previous section, with the copper absorbers, the Si-1MeV neutron equivalent fluence is dominated by the electromagnetic part of the radiation field. Therefore, this quantity decreases with increasing shielding thickness as well. Compared it with the acceptable HL-LHC values, these Si-1MeV neutron equivalent fluence should be acceptable.

As already discussed for the spectra, the shielding does not substantially affect neutron-dominated quantities, meaning the high energy hadron equivalent fluence and the thermal neutron equivalent fluence. The high energy hadron equivalent fluence values are

similar in all the cases. The values stay within a factor of two for the thermal neutron equivalent fluence.

These studies have been implemented as a proof of concept. It has been shown that additional localised shielding can reduce the radiation load on critical systems. However, further studies should be performed to find a sustainable solution for the various systems in close collaboration with the respective experts .

5.2 Bremsstrahlung

Another phenomenon that needs to be evaluated regarding energy deposition in the arcs is the gas bremsstrahlung. In this case, the beam particles undergo bremsstrahlung events due to residual gas molecules in the vacuum chamber. This problem is pressing for the Z operation mode at 45.6 GeV, as there is the highest bunch charge, which implies the highest amounts of such events happening.

The simulation itself is split into three different steps. In the first step, the gas density profile is established and transferred into a file with the atom density (atoms/m^3) as a function of the s-coordinate for the gas constituents.

For the FCC-ee arc gas bremsstrahlung simulation, the gas pressure is set at 5×10^{-10} mbar (UHV)[175] for room temperature, which translates to 1.147×10^{14} mol/m^3 of CO at room temperature. This is an assumption is highly conservative, as most likely the pressure can be higher.[176]. So far, a uniform distribution is implemented, and for

The second step is a trajectory run, which uses the gas profile file from the previous step, and provides the ideal lepton (e-/e+) trajectory through the line together with the bremsstrahlung probability function.

For the last step, no beam is used, but bremsstrahlung products are sampled based on the probability function from the file produced in the previous step and then tracked for the energy deposition studies. One of the output files provides noteworthy information for normalising the results, like the cumulative bremsstrahlung probability. The latter strongly depends on the low photon production threshold selected by the user. First, the beam depopulation rate due to gas bemsstrahlung events. For this purpose, it is assumed that an event generating a photon below threshold does not lead to primary particle loss, since its energy loss is compensated for by the RF system.

γ **prod. thres.**	**Int. prob.**	**BLT**
100MeV	1.495×10^{-11}	8h24min
27MeV	1.828×10^{-11}	7h01min
10MeV	2.121×10^{-11}	6h05min
1MeV	2.748×10^{-11}	4h40min
333keV	3.047×10^{-11}	4h12min
100keV	3.374×10^{-11}	3h48min
10keV	4.001×10^{-11}	3h12min
1keV	4.628×10^{-11}	2h45min
100eV	5.224×10^{-11}	2h27min

Table 5.5. Beam lifetime (BLT) and gas interaction probability (Int. prob.) depending on the low photon production threshold (γ prod. thres.).

Table 5.5 shows that for the indicated gas density the beam lifetime due to gas

bremsstrahlung events ranges from around 2.5 h up to 8.5 h, depending on the aforementioned threshold. The BLT is calculated using the given cumulative bremsstrahlung probability and the revolution frequency of 3.286 kHz for a length of the whole ring of 91.1 km.

The beam lifetime and the gas interaction probability are directly related to each other. The FLUKA simulation provides the gas interaction probability for the length of the 140 m long cell. For obtaining the BLT, this value first has to be re-scaled for the full length of the ring, which results in the interaction probability for one full turn. If this value is now multiplied by the revolution frequency, the interaction probability per second is obtained. Taking the inverse of this value, eventually results in the BLT.

In FCC-ee, the beam lifetime due to Bhabha scattering and beamstrahlung is expected at 68 min and >200 min, respectively. For higher energy operation modes, the beam lifetime reduces to 18 min.[24]. Taking these effects into account, the contribution of the bremsstrahlung losses seems to be negligible, for the reference gas density considering its mild variation over the wide photon threshold range that was explored.

Furthermore, the deposited power should be evaluated to assess the severity of energy deposition issues. For a low photon threshold of 333 keV and a beam current of 1.39 A, 1.275 kW are deposited over the length of the entire ring, which relates to 14 mW/m per beam. SR leads to 600 W/m, which makes the power due to gas bremsstrahlung negligible. To calculate the beam power, first the beam energy for the 45.6 GeV operation mode has to be found:

$$\frac{1.39}{1.602\times10^{-19}}\frac{A}{C}\cdot\frac{1}{3.286\times10^{3}}\mathrm{s}\cdot45.6\frac{\mathrm{GeV}}{\mathrm{e}-}\cdot1.602\times10^{-10}=19.29\,\mathrm{MJ}. \tag{5.3}$$

The beam energy is divided by the BLT, which results in a power loss of 1.275 kW for the photon threshold at 333 keV (see Table 5.5). The actual beam lifetime is higher for the other operation modes due to smaller bunch charges. The lower current leads to lower emitted power due to gas bremsstrahlung in the other three cases.

The machine is characterised by the maximum acceptable momentum loss, which is assumed to be at 1.3% for the current settings[24]. This percentage accounts mainly for losses in the interaction region. Several energy simulations are performed with differently high energy cuts in the user routine to evaluate how much power impacts the cell geometry depending on the acceptable momentum loss. If a beam particle with an energy higher than the cut-off energy results from a bremsstrahlung event, the code assumes that this particle stays in the beam, as its energy loss can be compensated for, and does not further track it. A particle with a lower energy beyond the acceptable momentum loss and, therefore, is lost somewhere in the machine where it deposits energy. With the cut-off energy getting closer to the beam energy, i.e. the maximum acceptable momentum loss becoming smaller, the impact on the machine increases (see Table 5.6). However, as discussed above, even if the bremsstrahlung power impacts the geometry, the effect is several orders of magnitude smaller than what is seen by SR. These stud-

ies conclude that the radiation load in the FCC-ee arcs due to gas bremsstrahlung is negligible for the assumed gas density.

$\Delta p_{max}/E_{min}$	**Deposited energy**	**Missing percentage**
10% / 41.04 GeV	7.668 GeV/pr	83%
5% / 43.32 GeV	10.07 GeV/pr	78%
1% / 45.144 GeV	16.37 GeV/pr	64%
0.1% / 45.5544 GeV	25.75 GeV/pr	43%

Table 5.6. Deposited energy per bremsstrahlung event, depending on the high acceptable momentum loss cut-off energy in the `usrmed.f`[107] routine. The first column gives the maximum acceptable momentum loss, which is also translated into the minimum acceptable beam particle energy.The third column indicates the percentage of power that does not impact the machine. A lower cut-off leads less losses.

6

Sixth Chapter

Conclusion

The FCC-ee machine is one of the possible future accelerators, which is currently in the state of a feasibility study. The collider ring will have a circumference of 91 km, colliding electrons and positrons at energies up to 182.5 GeV. The radiation load in a machine with such high beam energies and intensities is significant and needs to be assessed. This thesis investigated the radiation load in two parts of the machine that are strongly impacted: the radiation load in the positron production target and the radiation load due to synchrotron radiation (SR) in the collider arcs.

The radiation load studies were performed with the Monte Carlo code FLUKA. This tool allows the determination of macroscopic quantities, like power density, ionising dose and DPA, in the accelerator structure by simulating the transport of the particles and its multiplication in the material. Furthermore, it is also possible to obtain particle spectra, which allows for the characterisation of the radiation field and its distribution in energy. Another benefit of FLUKA is the possibility of implementing a realistic geometry using the user interface Flair, which leads to accurate predictions.

Before the particles enter the collider ring at the top energy, they are accelerated through several stages. First, electrons are produced by an electron gun and accelerated to 6 GeV. At this energy, the electrons can be transferred to two different paths. If the electrons are required in the collider ring, they are transferred into the higher energy acceleration stages. Otherwise, the electrons are used for positron production. The positrons are produced with an amorphous tungsten target embedded in a structure that contains high-temperature superconducting (HTS) coils that provide a solenoid field, which is used to increase the positron yield. In a capture linac that follows downstream, the positrons are shaped into a bunched beam at 200 MeV. Then they are further accelerated to 1.54 GeV, where they enter the common linac to be accelerated to 6 GeV. This common linac is also used to accelerate the electrons. From that point, the leptons move

into the next stage of acceleration, either a high energy linac (up to 20 GeV) or the SPS that serves as the pre-booster ring (PBR) (up to 16 GeV). Which machine will eventually be put into place still has to be decided. After this stage, the particles are transferred into the booster ring, located on top of the collider machine, where particles are accelerated up to top energy, which depends on the operation mode (45.6 GeV, 80 GeV, 120 GeV or182.5 GeV).

In the arcs of the collider ring, electrons and positrons lose a significant amount of energy due to SR. For the $t\bar{t}$ operation mode (182.5 GeV), the energy loss per turn due to SR is close to 10 GeV, which is the energy that has to be given by the RF system in every turn. Further physical effects, like Bhaba scattering or beamstrahlung, lead to a beam lifetime of a few minutes. Therefore, a top-up injection is foreseen, which means a constant filling from the booster.

One of the main topics of this thesis is the radiation load on the positron production target. The question was if the novel technology using HTS coils to produce the solenoid field is feasible. The advantage of using HTS coils instead of a more common Flux Concentrator (FC) lies in the magnitude of the magnetic field that can be reached, which is significantly higher if HTS coils are used (up to 20 T). A higher magnetic field is beneficial as it increases the positron yield. However, such a solution is only possible if the radiation load on the coils is below the acceptable thresholds, avoiding solenoid quenching or the long-term damage of organic insulator material. It could be shown that the power density on all coils is below the quench threshold and that the longitudinal position of the target significantly impacts the ionising dose levels of the coils. A position of the target further downstream decreases the impact on the coils. In the final, most realistic scenario, the coils absorb at most 22 MGy/year. Adding a factor of 10 to reach the full operational time, 220 MGy are obtained. It still has to be evaluated if these dose levels are bearable. If organic materials should be used, these dose levels are a showstopper, as the limit is given at around 30 MGy. If such a setup is foreseen, further mitigation measures like a thicker shielding or a placement of the coils further outside must be implemented.

The target is impacted by a 6 GeV electron beam of 13.34 kW, which puts a high strain on that component. The highest impact is strongly localised and results in 80 kW/cm^3 and 8 DPA/year. These results indicate that an elaborate cooling system has to be developed. However, the main issue is the reached DPA level that is not sustainable as it would require the change of the target once per year. It has to be remarked that for the time being, conservatively, a positron yield of 1 is assumed, while most likely is much higher, up to a factor of four. Considering a higher positron yield, this accordingly would decrease the beam power by a factor of four and the levels seen on the target, implying that they become acceptable. With the current knowledge, it can be assumed that a stationary target can be used, which should be made in one piece with the shielding to facilitate the cooling and manufacturing.

The second part of the study focused on the impact of SR in the FCC-ee arcs. The emitted power of SR is proportional to $(E/m)^4$, so this is an issue especially prevalent in electron-positron machines with high energies. In FCC-ee, 50 MW of SR per beam is emitted and deposited somewhere in the accelerator. Especially for the highest energy mode, this power is particularly penetrating as the energy of the SR photons is in the Compton scattering range. The SR power is the same for the lower energies due to much higher currents. However, the power deposition is less critical as most of the power is deposited by particle with energies and, therefore, is immediately absorbed in the dedicated photon absorbers.

As it is not feasible to simulate the entire arcs, a representative 140 m long half cell was implemented, containing five dipoles, five quadrupoles, and four sextupoles, all warm magnets. The collider geometry was embedded in a realistic tunnel layout. Over the length of the cell, 25 copper alloy absorbers per beam were placed on the external side of the vacuum chamber with a spacing of around 5 m-6 m between each of them. The simulations were mainly performed for the operation mode of 182.5 GeV, showing that the absorbers take up around 75% of the power. The impact on the magnets is not negligible, but as these are warm magnets, their functionality is not expected to be jeopardised. It only has to be assessed if organic insulator material will eventually be used in the dipole busbars. If so, further mitigation measures have to be implemented.

Even though SR is tangentially emitted to the outside, higher dose levels are seen on the inside of the collider due to the backscattering of particles on the absorbers. Contrarily, the dose levels 1 m above the collider are significantly lower. These results led to the decision that the booster ring should be placed on top of the collider ring rather than next to it. Nevertheless, the dose levels in the tunnel, which are in the range of several hundreds of kGy per year of $t\bar{t}$ operation, are too high for the electronic components. Therefore, the effects of localised shielding have been studied, investigating different thicknesses of lead and concrete in the bottom corner of the tunnel. It was shown that such a measure damps the electromagnetic part of the spectrum. For the neutrons, a suitable layer should be implemented as well. A recent change in the tunnel geometry foresees a 10 cm thick concrete floor, below which cable trays should be installed. The outcome of these simulations is positive, showing that the dose levels can be reduced to an extent that would allow using commercial cables.

Summarising, it can be said that no major showstoppers have been found. Particular problems, like the dose levels in the tunnel or the radiation load on the positron target, can be mitigated if additional measures are implemented. This study gathered different results showing that a project like FCC-ee is feasible regarding radiation load.

However, as it is a large and complex machine, several open questions are to be investigated from the energy deposition standpoint. These open points include the radiation load in the collider tunnel due to the booster, which strongly depends on the filling pattern of the booster. Another open point is the collimation system which is by design a critical area regarding radiation load. So far, the positron production target has been

thoroughly studied, leaving the transfer lines between the different accelerator stages to be investigated. Finally, the MDI region also poses energy deposition challenges.

Long story short: a lot has been successfully done, but more work is still to come. It will not get boring.

Appendix A

Comparison of the DPA, DPA-NRT and ARCDPA in the AMD

In this part, three different models to simulate the DPA are discussed. The model, implemented initially in FLUKA, is based on the model of Kinchin and Pease (1955), where there is either a displacement happening or not. In the 20 following years, Norgett, Robinson, and Torrens performed binary collision approximation simulations to find a model that better describes the DPA's behaviour.

This model is now known as the DPA-NRT and is the standard for calculating primary radiation damage nowadays. However, comparing the results to experimental data, DPA-NRT significantly overestimates the DPA by up to a factor of 3, mainly caused by recombinations in the cascade that DPA-NRT does not consider.

In 2018, Nordlund et al. published a more accurate way of calculating the DPA, the ARC-DPA (Athermal Recombination Corrected) model that considers recombinations. The disadvantage of this model is the constants needed to calculate the ARC-DPA that must be obtained experimentally for each material and compound. Without experimental data, no reliable results can be produced.

Recently[1], the option for scoring DPA-NRT and ARC-DPA was implemented in FLUKA. With the well-understood DPA data available for the FCC-ee AMD, there was the opportunity to use this geometry for DPA benchmarking simulations.

The different versions of DPA were compared for the coils and the target. While the target is made of pure tungsten, the coils are a compound of many different materials. The coefficients a_{ARC} and b_{ARC} are well known for pure tungsten, but they are unknown for the compound of the coils. Therefore, a visible difference between the three DPAs for the target is expected. Due to the unknown coefficients, the DPA-NRT and ARC-DPA values on the coils are expected to be similar.

[1] 2022

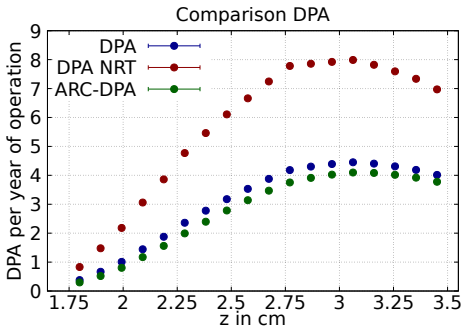

Fig. A.1. Comparison of the different DPA models on the target. The NRT-DPA is much higher than the Kinchin-Pease DPA model. Taking the recombination of atoms into account in the ARC-DPA leads again to much lower values.

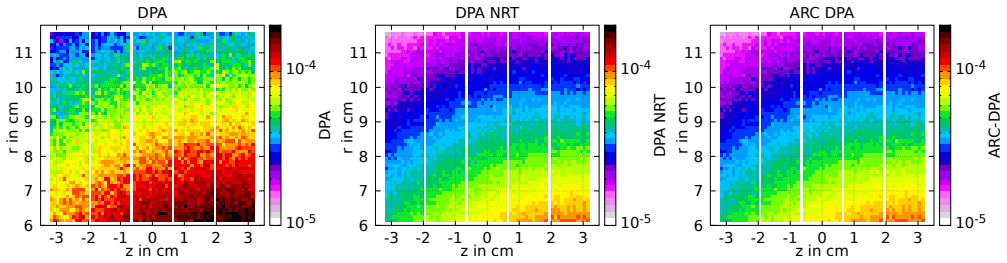

(a) **(b)** **(c)**

Fig. A.2. Comparison of the (a) DPA, (b) DPA-NRT and (c) ARCDPA on the HTS coils. The coil material is a compound with unknown coefficients, so the latter two give the same result.

As expected, the differences in DPA are significant on the target (see Fig. A.1). The DPA-NRT values are nearly a factor of two higher than the initial DPA study. The values for the ARC-DPA, where the recombinations are considered, are generally lower than in the initial DPA study due to the well-known coefficients a_{ARC} and b_{ARC}. The maximum DPA is obtained at the same longitudinal position, as the behaviour is similar and only the magnitude changes.

Compared to the target, the coil material is a compound for which the coefficients a_{ARC} and b_{ARC} have yet to be evaluated. As these coefficients are unknown, the values between DPA-NRT and ARC-DPA do not vary, as shown in Fig. A.2. Interestingly, the original DPA is higher than what is obtained with the newer models.

After performing the different simulations, it is recommended to use ARC-DPA if experimental data is available to use the correct coefficients and if this is not, use DPA-NRT.

B

Appendix B

Energy Deposition Studies for the P3 AMD

In a proof of concept experiment, the same geometry of the AMD is implemented at the P^3 experiment[134] at PSI, Villingen. The beam energy and the beam spot size, as well as the geometry, are identical to V6 S-Band$_{\text{Pess}}$, where no shielding is foreseen due to a lower beam power of 1.2 W. This power is obtained by an electron beam with an energy of 6 GeV, similar to the one of FCC-ee. The other parameters are much smaller, with the repetition rate at 1 Hz with one bunch of 1.2489×10^9 electrons relating to 200 pC. The experiment is operated for one month, which is essential information for long-term radiation effects like the ionizing dose and the DPA.

In total, 308.5 mW are deposited on the AMD, while around 0.9 W leave the device downstream. Of the 308.5 mW impacting the AMD, 280 mW are impacting the target itself.

A relatively higher impact is expected on the coils as no shielding is implemented. The highest obtained values of power density are found at 0.005 mW/cm^3, which is negligible (see Fig. B.1). The dose values peak at 1.5 kGy for 1 month of operation, which is feasible. Similarly, positive results are found for the DPA with the highest values around 1×10^{-9} DPA. The highest power density and dose values are located in the downstream corner of the most downstream coil, a behaviour already known from the FCC-ee simulations. No distinct maximum can be found for the DPA, and the values constantly decrease, moving further outside radially.

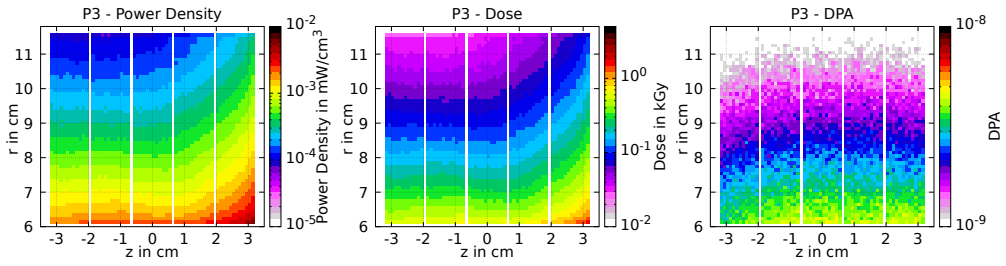

(a) **(b)** **(c)**

Fig. B.1. P3 Coils: (a) Power Density, (b) Dose and (c) DPA.

BIBLIOGRAPHY

[1] *FCC*. https://fcc.web.cern.ch/. accessed: 10.9.2023.

[2] J.D. Cockroft and E.T.S Walton. "Experiments with high velocity positive ions". In: *Proc. R. Soc. Lond. A* 129 (1930), pp. 477–489.

[3] *The Nobel Prize in Physics 1951*. https://www.nobelprize.org/prizes/physics/1951/summary/. accessed: 10.9.2023.

[4] E.O. Lawrence and M.S. Livingston. "The Production of High Speed Light Ions Without the Use of High Voltages". In: *Phys. Rev.* 40 (1 Apr. 1932), pp. 19–35. DOI: 10.1103/PhysRev.40.19.

[5] O. Brüning et al. *LHC Design Report*. CERN Yellow Reports: Monographs. Geneva: CERN, 2004. DOI: 10.5170/CERN-2004-003-V-1. URL: https://cds.cern.ch/record/782076.

[6] *CERN*. https://home.cern/. accessed: 10.9.2023.

[7] J.P. Burnet et al. *Fifty years of the CERN Proton Synchrotron: Volume 1*. CERN Yellow Reports: Monographs. Geneva: CERN, 2011. DOI: 10.5170/CERN-2011-004. URL: https://cds.cern.ch/record/1359959.

[8] CMS Collaboration. *CMS Physics: Technical Design Report Volume 1: Detector Performance and Software*. Technical design report. CMS. Geneva: CERN, 2006. URL: http://cds.cern.ch/record/922757.

[9] ATLAS Collaboration. *ATLAS: technical proposal for a general-purpose pp experiment at the Large Hadron Collider at CERN*. LHC technical proposal. Geneva: CERN, 1994. DOI: 10.17181/CERN.NR4P.BG9K. URL: http://cds.cern.ch/record/290968.

[10] ALICE Collaboration. *ALICE: Physics Performance Report*. Tech. rep. Geneva: CERN, 2004. DOI: 10.1088/0954-3899/30/11/001. URL: http://cds.cern.ch/record/643556.

[11] LHCb Collaboration. *LHCb : Technical Proposal*. Geneva: CERN, 1998. URL: https://cds.cern.ch/record/622031.

[12] *The Nobel Prize in Physics 2013*. https://www.nobelprize.org/prizes/physics/2013/summary/. accessed: 10.9.2023.

[13] M. Mangano et al. *FCC Physics Opportunities: Future Circular Collider Conceptual Design Report Volume 1. Future Circular Collider*. Tech. rep. CERN-ACC-2018-0056. Geneva: CERN, 2019. DOI: 10.1140/epjc/s10052-019-6904-3.

[14] E. Gschwendtner. "AWAKE, A Particle-driven Plasma Wakefield Acceleration Experiment". In: (2016), pp. 271–288. DOI: 10.5170/CERN-2016-001.271. arXiv: 1705.10573. URL: https://cds.cern.ch/record/2203638.

[15] P Schmüser. "Free-electron lasers". In: (2006). DOI: 10.5170/CERN-2006-002.477. URL: https://cds.cern.ch/record/941330.

[16] C. Accettura et al. *Towards a Muon Collider*. 2023. arXiv: 2303.08533 [physics.acc-ph].

[17] A. Robson et al. *The Compact Linear e^+e^- Collider (CLIC): Accelerator and Detector*. 2018. arXiv: 1812.07987 [physics.acc-ph].

[18] The CEPC Study Group. *CEPC Conceptual Design Report: Volume 1 - Accelerator*. 2018. arXiv: 1809.00285 [physics.acc-ph].

[19] H. Yamamoto. "The International Linear Collider Project—Its Physics and Status". In: *Symmetry* 13.4 (2021). ISSN: 2073-8994. DOI: 10.3390/sym13040674. URL: https://www.mdpi.com/2073-8994/13/4/674.

[20] The European Strategy Group. *Deliberation document on the 2020 Update of the European Strategy for Particle Physics*. Tech. rep. CERN-ESU-014. Geneva, 2020. DOI: 10.17181/ESU2020Deliberation. URL: http://cds.cern.ch/record/2720131.

[21] "FCC Feasibility Study: plans and deliverables for the 2023 mid-term review. Restricted Council - Two-Hundred-and-Ninth Session". In: (2022). URL: https://cds.cern.ch/record/2838409.

[22] *LEP design report*. Report. Geneva: CERN, 1984. URL: https://cds.cern.ch/record/102083.

[23] F. Gianotti. *Introductory Remarks*. presented at the FCC Week 2023. accessed: 10.9.2023. URL: https://videos.cern.ch/record/2298130.

[24] M. Benedikt et al. *FCC-ee: The Lepton Collider: Future Circular Collider Conceptual Design Report Volume 2. Future Circular Collider*. Tech. rep. CERN-ACC-2018-0057. Geneva: CERN, 2019. DOI: 10.1140/epjst/e2019-900045-4.

[25] M. Benedikt et al. *FCC-hh: The Hadron Collider: Future Circular Collider Conceptual Design Report Volume 3. Future Circular Collider*. Tech. rep. CERN-ACC-2018-0058. Geneva: CERN, 2019. DOI: 10.1140/epjst/e2019-900087-0.

[26] *FCC Aerial View*. http://cds.cern.ch/record/2653532. accessed: 10.9.2023.

[27] O. Aberle et al. *High-Luminosity Large Hadron Collider (HL-LHC): Technical design report*. CERN Yellow Reports: Monographs. Geneva: CERN, 2020. DOI: 10.23731/CYRM-2020-0010.

[28] H. Pommerenke et al. "RF Design of Traveling-Wave Accelerating Structures for the FCC-ee Pre-injector Complex". In: *JACoW LINAC* 2022 (2022), pp. 707–710. DOI: 10.18429/JACoW-LINAC2022-THPOJO08. URL: https://cds.cern.ch/record/2844845.

[29] R. Kersevan. "Vacuum System of the FCC-ee". In: *JACoW* eeFACT2022 (2023), pp. 244–246. DOI: 10.18429/JACoW-eeFACT2022-THXAS0104.

[30] F. Peauger et al. "SWELL and Other SRF Split Cavity Development". In: *JACoW* LINAC2022 (2022), pp. 300–304. DOI: 10.18429/JACoW-LINAC2022-TU1AA04.

[31] D. Tommasini. "Nb3Sn Accelerator Dipole Magnet Needs for a Future Circular Collider". In: *Nb3Sn Accelerator Magnets: Designs, Technologies and Performance*. Ed. by D. Schoerling and A.V. Zlobin. Cham: Springer International Publishing, 2019, pp. 427–439. ISBN: 978-3-030-16118-7. DOI: 10.1007/978-3-030-16118-7_16.

[32] M. Benedikt. *FCC Feasibility Study*. presented at the FCC Week 2023. accessed: 10.9.2023. URL: https://indico.cern.ch/event/1202105/contributions/5423504/.

[33] T. Raubenheimer. *FCC Accelerator*. presented at the FCC Week 2023. accessed: 10.9.2023. URL: https://indico.cern.ch/event/1202105/contributions/5423512/.

[34] I. Agapov et al. *Future Circular Lepton Collider FCC-ee: Overview and Status*. 2022. arXiv: 2203.08310 [physics.acc-ph].

[35] P. Craievich et al. *FCC-ee Injector Study and the P3 Project at PSI*. Tech. rep. accessed: 10.9.2023. CHART Collaboration, 2022. URL: https://chart.ch/wp-content/uploads/2022/05/Chart-Scientific-Report-2021-FCCee-Injector.pdf.

[36] H. Bartosik. *SPS Pre-Booster Option*. presented at the FCC Week 2023. accessed: 10.9.2023. URL: https://indico.cern.ch/event/1202105/contributions/5390936/.

[37] M. Aiba et al. "Top-up injection schemes for future circular lepton collider". In: *Nuclear Instruments and Methods in Physics Research Section A: Accelerators, Spectrometers, Detectors and Associated Equipment* 880 (2018), pp. 98–106. ISSN: 0168-9002. DOI: https://doi.org/10.1016/j.nima.2017.10.075. URL: https://www.sciencedirect.com/science/article/pii/S0168900217311646.

[38] P. Craievich et al. "The FCCee Pre-Injector Complex". In: *JACoW* IPAC2022 (2022), pp. 2007–2010. DOI: 10.18429/JACoW-IPAC2022-WEPOPT063.

[39] R. Bayley, ed. *Proceedings, CAS - CERN Accelerator School: Free Electron Lasers and Energy Recovery Linacs: Hamburg, Germany, May 31 - June 10, 2016*. Vol. 1/2018. CERN Yellow Reports: School Proceedings. Geneva: CERN, 2018. Chap. Bunch Length Compressors. DOI: 10.23730/CYRSP-2018-001.

[40] P. Craievich et al. *Pre-Injector baseline and options*. presented at the FCC Week 2023. accessed: 10.9.2023. URL: https://indico.cern.ch/event/1202105/contributions/5384834/.

[41] V. Zdenek. *Electron Source*. presented at the FCC-ee Pre-Injector: CHART Collaboration Meeting. accessed: 10.9.2023. URL: https://agenda.infn.it/event/34369/contributions/194461/.

[42] S. Bettoni. *Linac Design*. presented at the FCC-ee Injector Studies Mini-Workshop (24.-25.11.2022). accessed: 10.9.2023. URL: https://indico.ijclab.in2p3.fr/event/8920/contributions/28003/.

[43] S. Bettoni. *Electron, common and High-Energy Linacs*. presented at the FCC-ee Pre-Injector: CHART Collaboration Meeting. accessed: 10.9.2023. URL: https://agenda.infn.it/event/34369/sessions/25445/\#20230420.

[44] I. Chaikovska et al. “Positron sources: from conventional to advanced accelerator concepts-based colliders”. In: *Journal of Instrumentation* 17.05 (May 2022), P05015. DOI: 10.1088/1748-0221/17/05/p05015. URL: https://doi.org/10.1088%2F1748-0221%2F17%2F05%2Fp05015.

[45] M. Schaer. *Positron Linac Design*. presented at the FCC-ee Pre-Injector: CHART Collaboration Meeting. accessed: 10.9.2023. URL: https://agenda.infn.it/event/34369/sessions/25445/\#20230420.

[46] S. Spampinanti. *Energy Compressor*. presented at the FCC-ee Pre-Injector: CHART Collaboration Meeting. accessed: 10.9.2023. URL: https://agenda.infn.it/event/34369/sessions/25447/\#20230421.

[47] A. Wolski. *The Accelerator Physics of Linear Collider Damping Rings*. Notes for USPAS Course on Linear Colliders. accessed: 10.9.2023. Santa Barbara, 2003. URL: https://www.desy.de/~njwalker/uspas/coursemat/notes/unit_4_notes.pdf.

[48] A. De Santis. *DR Status Summary*. presented at the FCC-ee Injector Studies Mini-Workshop (24.-25.11.2022). accessed: 10.9.2023. URL: https://indico.ijclab.in2p3.fr/event/8920/contributions/28007/.

[49] O. Etisken. *Considerations About New Damping Ring Layout*. presented at the FCC-ee Injector Studies Mini-Workshop (24.-25.11.2022). accessed: 10.9.2023. URL: https://indico.ijclab.in2p3.fr/event/8920/contributions/28007/.

[50] S. Ogur et al. “Overall Injection Strategy for FCC-ee”. In: (2019), TUPAB03. DOI: 10.18429/JACoW-eeFACT2018-TUPAB03. URL: https://cds.cern.ch/record/2713264.

[51] K. Cornelis and R. Schmidt. “The performance of the SPS as LEP injector”. In: CERN-SPS-89-16-AOP (1990). URL: https://cds.cern.ch/record/217377.

[52] A. Grudiev. *Layout and design of positron and electron linacs up to 20 GeV*. presented at the FCC Week 2023. accessed: 10.9.2023. URL: https://indico.cern.ch/event/1202105/contributions/5383358/.

[53] J. Bauche, C.J. Eriksson, and F. Saeidi. *Status of the FCC-ee booster and collider magnet developments*. presented at the FCC Week 2023. accessed: 10.9.2023. URL: https://indico.cern.ch/event/1202105/contributions/5385367/.

[54] A. Chance. *Full-energy booster*. presented at the FCC Week 2023. accessed: 10.9.2023. URL: https://indico.cern.ch/event/1202105/contributions/5408586/.

[55] K. Oide. *FCC-ee operation modes*. presented at the FCC-ee Injector Studies Mini-Workshop (24.-25.11.2022). accessed: 10.9.2023. IJCLab, Paris. URL: https://indico.cern.ch/event/1202105/contributions/5384834/.

[56] H. Wiedemann. *Particle accelerator physics; 3rd ed.* Berlin: Springer, 2007. DOI: 10.1007/978-3-540-49045-6. URL: https://cds.cern.ch/record/1083415.

[57] *CAS - CERN Accelerator School: Beam Injection, Extraction and Transfer: Erice, Italy 10 - 19 Mar 2017. CAS - CERN Accelerator School: Beam Injection, Extraction and Transfer*. CERN. Geneva: CERN, 2018. DOI: 10.23730/CYRSP-2018-005.

[58] P Pearce. *Pulsed Power for Future Linear Accelerators*. Tech. rep. Geneva: CERN, 1999. URL: https://cds.cern.ch/record/386541.

[59] A. Lechner. "Particle interactions with matter". In: *CERN Yellow Rep. School Proc.* 5 (2018), p. 47. DOI: 10.23730/CYRSP-2018-005.47. URL: https://cds.cern.ch/record/2674116.

[60] A.B. Timothy. "HIGH POWER TARGETS FOR SPALLATION SOURCES". In: 1996.

[61] B. Humann. "Energy Deposition Studies for the Experimental Insertions of FCC-hh". Presented 10 Jan 2020. 2019. URL: https://cds.cern.ch/record/2706382.

[62] J. Beringer et al. "Review of Particle Physics, 2012-2013. Review of Particle Properties". In: *Phys. Rev. D* 86.1 (2012), p. 010001. DOI: 10.1103/PhysRevD.86.010001. URL: https://cds.cern.ch/record/1481544.

[63] *The Nobel Prize in Physics 1921*. https://www.nobelprize.org/prizes/physics/1921/summary/. accessed: 10.9.2023.

[64] A. Fasso et al. "FLUKA Realistic Modeling of Radiation Induced Damage". In: *Progress in NUCLEAR SCIENCE and TECHNOLOGY* 2 (Oct. 2011), pp. 769–775. DOI: 10.15669/pnst.2.769.

[65] J. Frenkel. "Über die Wärmebewegung in festen und flüssigen Körpern". In: *Zeitschrift für Physik* 35.8 (Aug. 1926), pp. 652–669. DOI: 10.1007/BF01379812.

[66] Ferrari, A. *Interactions of Particles with Matter*. CAS - Medical Applications. accessed 13/05/2022. 2015. URL: https://indico.cern.ch/event/324187/contributions/752822/attachments/628087/864333/Ferrari_CAS_May15.pdf.

[67] M. Delmaestro. *Particle interactions in particle detectors*. ESIPAP (2014) - Module 1 - Physics of particle and astroparticle detectors. accessed 13/09/2023. URL: https://indico.cern.ch/event/294651/contributions/671929/.

[68] *Atomic and Nuclear Properties for W*. accessed: 10.9.2023. URL: https://pdg.lbl.gov/2020/AtomicNuclearProperties/HTML/tungsten_W.html.

[69] M. Gupta. *Calculation of radiation length in materials*. Tech. rep. Geneva: CERN, 2010. URL: https://cds.cern.ch/record/1279627.

[70] *Atomic and Nuclear Properties of Materials*. accessed: 10.9.2023. URL: https://pdg.lbl.gov/2009/AtomicNuclearProperties/.

[71] W. Heitler. *The Quantum Theory of Radiation*. Clarendon Press, Oxford, 1954.

[72] *Bremsstrahlung*. Geant4 Tutorial (2006). accessed 13/09/2023. URL: https://lappweb.in2p3.fr/~maire/tutorials/bremsstrahlung.pdf.

[73] H. Bethe and W. Heitler. “On the Stopping of fast particles and on the creation of positive electrons”. In: *Proc. Roy. Soc. Lond. A* 146 (1934), pp. 83–112. DOI: 10.1098/rspa.1934.0140.

[74] B. M. Spicer. “The Giant Dipole Resonance”. In: *Advances in Nuclear Physics: Volume 2*. Ed. by Michel Baranger and Erich Vogt. New York, NY: Springer US, 1969, pp. 1–78. ISBN: 978-1-4684-8343-7. DOI: 10.1007/978-1-4684-8343-7_1.

[75] *Evaluated Nuclear Data File (ENDF)*. accessed 13/05/2022. URL: https://www.nndc.bnl.gov/endf/.

[76] *The Swiss Light Source*. https://www.psi.ch/en/sls/about-sls. accessed: 10.9.2023.

[77] E. Wiechert. “Elektrodynamische Elementargesetze”. In: *Annalen der Physik* 309.4 (1901), pp. 667–689. DOI: https://doi.org/10.1002/andp.19013090403.

[78] J.P. Blewett. “Radiation Losses in the Induction Electron Accelerator”. In: *Phys. Rev.* 69 (3-4 Feb. 1946), pp. 87–95. DOI: 10.1103/PhysRev.69.87.

[79] F. R. Elder et al. “Radiation from Electrons in a Synchrotron”. In: *Phys. Rev.* 71 (11 June 1947), pp. 829–830. DOI: 10.1103/PhysRev.71.829.5. URL: https://link.aps.org/doi/10.1103/PhysRev.71.829.5.

[80] M. Luckhof. “Background Processes Affecting the Machine-Detector Interface at FCC-ee With Focus on Synchrotron Radiation at 182.5 Gev Beam Energy”. Presented 12 Mar 2021. 2020. URL: https://cds.cern.ch/record/2766209.

[81] J. Larmor D.Sc. F.R.S. “LXIII. On the theory of the magnetic influence on spectra; and on the radiation from moving ions”. In: *The London, Edinburgh, and Dublin Philosophical Magazine and Journal of Science* 44.271 (1897), pp. 503–512. DOI: 10.1080/14786449708621095.

[82] R.P. Walker. “Synchrotron radiation”. In: (1994). DOI: 10.5170/CERN-1994-001.437. URL: https://cds.cern.ch/record/398429.

[83] J. Gareyte. “LHC main parameters”. In: *Part. Accel.* 50 (1995), pp. 61–68. URL: https://cds.cern.ch/record/304825.

[84] R. Bailey et al. “Synchrotron Radiation Effects at LEP”. In: (1998). URL: https://cds.cern.ch/record/360833.

[85] J.D. Jackson. *Classical Electrodynamics*. Wiley, 1998. ISBN: 978-0-471-30932-1.

[86] Barletta W.A. *Unit 11 - Lecture 18: Synchrotron Radiation I*. USPAS (2016). accessed 13/05/2022. 2020. URL: https://uspas.fnal.gov/materials/09UNM/Unit_11_Lecture_18_Synchrotron_radiation.pdf.

[87] J. Schwinger. “On the Classical Radiation of Accelerated Electrons”. In: *Phys. Rev.* 75 (12 June 1949), pp. 1912–1925. DOI: 10.1103/PhysRev.75.1912.

[88] D. Ivanenko and A. Sokolov. “Classical Field theory”. In: *GITTL (in Russian)* (1972).

[89] *Introduction to FLUKA*. presented at the Beginner course - ULB, May 2022. accessed: 10.9.2023. URL: https://indico.cern.ch/event/1123370/contributions/4715929/attachments/2444325/4188339/01_Introduction_to_FLUKA_2022_ULB.pdf.

[90] *Introduction to the Monte Carlo simulation of radiation transport*. presented at the Beginner course - ULB, May 2022. accessed: 10.9.2023. URL: https://indico.cern.ch/event/1123370/contributions/4715934/attachments/2444331/4188477/02_Monte_Carlo_Basics_2022_ULB.pdf.

[91] D.M. Benov. "The Manhattan Project, the first electronic computer and the Monte Carlo method". In: *Monte Carlo Methods and Applications* 22.1 (2016), pp. 73–79. DOI: doi:10.1515/mcma-2016-0102. URL: https://doi.org/10.1515/mcma-2016-0102.

[92] N. Metropolis and S. Ulam. "The Monte Carlo Method". In: *Journal of the American Statistical Association* 44.247 (1949), pp. 335–341. ISSN: 01621459.

[93] N. Metropolis. "The Beginning of the Monte Carlo Method". In: *Los Alamos science. Special Issue dedicated to Stanislaw Ulam*. 1987, pp. 125–130.

[94] CERN. *FLUKA Website*. https://fluka.cern. accessed: 2023.

[95] C. Ahdida et al. "New Capabilities of the FLUKA Multi-Purpose Code". In: *Frontiers in Physics* 9 (2022). DOI: 10.3389/fphy.2021.788253. URL: https://www.frontiersin.org/article/10.3389/fphy.2021.

[96] G. Battistoni et al. "Overview of the FLUKA code". In: *Ann. Nucl. Energy* 82 (2015), 10–18. 9 p. DOI: 10.1016/j.anucene.2014.11.007. URL: http://cds.cern.ch/record/2162467.

[97] S. Agostinelli et al. "Geant4—a simulation toolkit". In: *Nuclear Instruments and Methods in Physics Research Section A: Accelerators, Spectrometers, Detectors and Associated Equipment* 506.3 (2003), pp. 250–303. ISSN: 0168-9002. DOI: https://doi.org/10.1016/S0168-9002(03)01368-8. URL: https://www.sciencedirect.com/science/article/pii/S0168900203013688.

[98] C. J. Werner et al. "MCNP Version 6.2 Release Notes". In: LA-UR-18-20808 (Feb. 2018). DOI: 10.2172/1419730. URL: https://www.osti.gov/biblio/1419730.

[99] N.V. Mokhov and C.C. James. "The MARS Code System User's Guide Version 15(2016)". In: (). DOI: 10.2172/1462233. URL: https://www.osti.gov/biblio/1462233.

[100] Tatsuhiko Sato et al. "Features of Particle and Heavy Ion Transport code System (PHITS) version 3.02". In: *Journal of Nuclear Science and Technology* 55.6 (2018), pp. 684–690. DOI: 10.1080/00223131.2017.1419890. eprint: https://doi.org/10.1080/00223131.2017.1419890. URL: https://doi.org/10.1080/00223131.2017.1419890.

[101] F. Salvat, J.M. Fernández-Varea, and J. Sempau. "PENELOPE-2011: A Code System for Monte Carlo Simulation of Electron and Photon Transport". In: *OECD NEA Data Bank/NSC DOC(2011)/5* (). URL: https://www.oecd-nea.org/upload/docs/application/pdf/2020-10/penelope-2018__a_code_system_for_monte_carlo_simulation_of_electron_and_photon_transport.pdf.

[102] V. Vlachoudis. "FLAIR: A Powerful But User Friendly Graphical Interface For FLUKA"". In: *Proc. Int. Conf. on Mathematics, Computational Methods & Reactor Physics (M&C 2009), Saratoga Springs, New York, 2009*. Apr. 2009.

[103] T. Williams, C. Kelley, and many others. *Gnuplot 4.6: an interactive plotting program*. http://gnuplot.sourceforge.net/. Apr. 2013.

[104] A. Mereghetti et al. "The Fluka Linebuilder and Element Database: Tools for Building Complex Models of Accelerators Beam Lines". In: *Conf. Proc.* C1205201 (2012), WEPPD071. URL: https://cds.cern.ch/record/1481554.

[105] H. Grote and F. Schmidt. "MAD-X: An upgrade from MAD8". In: *Conf. Proc. C* 030512 (2003), p. 3497.

[106] *MGDRAW Routine (FLUKA)*. accessed: 10.9.2023. URL: https://flukafiles.web.cern.ch/manual/chapters/user_routines/user_routines/mgdraw.html.

[107] *USRMED Routine (FLUKA)*. accessed: 10.9.2023. URL: https://flukafiles.web.cern.ch/manual/chapters/user_routines/user_routines/usrmed.html.

[108] N.V. Mokhov and F. Cerutti. "Beam-Material Interaction". In: (2016). Contribution to the 2014 Joint International Accelerator School: Beam Loss and Accelerator Protection, Newport Beach, CA, USA , 5-14 Nov 2014, pp. 83–110. DOI: 10.5170/CERN-2016-002.83. arXiv: 1608.02476. URL: https://cds.cern.ch/record/2206746.

[109] D. Tommasini. *Radiation limits of normal- and superconducting magnets*. presented at the FCC other Magnet Design Meeting #1. accessed 05/12/2019. 2017. URL: https://indico.cern.ch/event/647002/contributions/2628503/.

[110] G. Lerner et al. *RADIATION LEVEL SPECIFICATIONS FOR HL-LHC*. EDMS NO. 2302154 v1.0. accessed 13/05/2022. 2020. URL: https://edms.cern.ch/ui/file/2302154/1.0/HLLHC_Specification_Document_v1.0.pdf.

[111] G.H. Kinchin and R.S. Pease. "The Displacement of Atoms in Solids by Radiation". In: *Reports on Progress in Physics* 18.1 (1955), p. 1. DOI: 10.1088/0034-4885/18/1/301. URL: https://dx.doi.org/10.1088/0034-4885/18/1/301.

[112] M.T. Robinson and I.M. Torrens. "Computer simulation of atomic-displacement cascades in solids in the binary-collision approximation". In: *Phys. Rev. B* 9 (12 June 1974), pp. 5008–5024. DOI: 10.1103/PhysRevB.9.5008. URL: https://link.aps.org/doi/10.1103/PhysRevB.9.5008.

[113] M.J. Norgett, M.T. Robinson, and I.M. Torrens. "A proposed method of calculating displacement dose rates". In: *Nuclear Engineering and Design* 33.1 (1975), pp. 50–54. ISSN: 0029-5493. DOI: https://doi.org/10.1016/0029-5493(75)90035-7. URL: https://www.sciencedirect.com/science/article/pii/0029549375900357.

[114] K. Nordlund et al. "Improving atomic displacement and replacement calculations with physically realistic damage models". In: *Nature Communications* 9 (Mar. 2018). DOI: 10.1038/s41467-018-03415-5.

[115] R. García Alía. "Radiation Fields in High Energy Accelerators and their impact on Single Event Effects. Champs ionisants dans un accélérateur à haute énergie et leur impact sur les Effets Singuliers". Presented 15 Dec 2014. 2014. URL: https://cds.cern.ch/record/2012360.

[116] G. Lerner. *Accelerator radiation environment: modeling and monitoring tools and approaches*. presented at SERESSA (02.12.2020). accessed: 10.9.2023. URL: https://www.ufrgs.br/seressa2020/program.php.

[117] B. Humann et al. "Radiation Load Studies for the FCC-ee Positron Source with a Superconducting Matching Device". In: *Proc. 13th International Particle Accelerator Conference (IPAC'22)* (Bangkok, Thailand). JACoW Publishing, Geneva, Switzerland, July 2022, pp. 2879–2882. ISBN: 978-3-95450-227-1. DOI: 10.18429/JACoW-IPAC2022-THPOTK048.

[118] L. Bandiera et al. "Crystal-based pair production for a lepton collider positron source". In: *The European Physical Journal C* 82.8 (Aug. 2022). DOI: 10.1140/epjc/s10052-022-10666-6.

[119] R. Chehab et al. "Experimental study of a crystal positron source". In: *Physics Letters B* 525.1 (2002), pp. 41–48. ISSN: 0370-2693. DOI: https://doi.org/10.1016/S0370-2693(01)01395-8.

[120] T. Suwada et al. "Measurement of positron production efficiency from a tungsten monocrystalline target using 4- and 8-GeV electrons". In: *Phys. Rev. E* 67 (1 Jan. 2003), p. 016502. DOI: 10.1103/PhysRevE.67.016502.

[121] E.M. Reuter et al. "Mechanical design and development of a high power target system for the SLC positron source". In: *Conf. Proc. C* 910506 (1991). Ed. by Loretta Lizama and Joe Chew, pp. 1999–2001.

[122] L. Zang et al. "Design Optimization of Flux Concentrator for SuperKEKB". In: *Proc. 3rd International Particle Accelerator Conference (IPAC'12)* (New Orelans, Louisiana, USA). May 2012, pp. 2003–2006.

[123] Y. Enomoto et al. "A New Flux Concentrator Made of Cu Alloy for the SuperKEKB Positron Source". In: *Proc. IPAC'21* (Campinas, SP, Brazil). International Particle Accelerator Conference 12. JACoW Publishing, Geneva, Switzerland, pp. 2954–2956. DOI: 10.18429/JACoW-IPAC2021-WEPAB144.

[124] A.V. Kulikov, S.D. Ecklund, and E.M. Reuter. “SLC positron source pulsed flux concentrator”. In: (June 1991).

[125] L. Jd et al. “System design and measurements of flux concentrator and its solid-state modulator for CEPC positron source”. In: *Nuclear Science and Techniques* 32 (July 2021). DOI: 10.1007/s41365-021-00904-z.

[126] R. Chehab et al. “An adiabatic matching device for the Orsay linear positron accelerator”. In: *IEEE Trans. Nucl. Sci.* 30 (1983), pp. 2850–2852. URL: https://cds.cern.ch/record/143691.

[127] P. Martyshkin. *R&D on the Flux Concentrator and NC solenoid.* presented at the Physics design of the positron target and capture system - meeting # 01. accessed: 10.9.2023. URL: https://indico.cern.ch/event/938292/.

[128] Y. Zhao et al. “Comparison of Different Matching Device Field Profiles for the FCC-ee Positron Source”. In: *Proc. IPAC’21* (Campinas, SP, Brazil). International Particle Accelerator Conference 12. JACoW Publishing, Geneva, Switzerland, Aug. 2021, WEPAB015, pp. 2617–2620. DOI: 10.18429/JACoW-IPAC2021-WEPAB015. URL: https://jacow.org/ipac2021/papers/wepab015.pdf.

[129] I. Chaikovska. *Positron source advantages/disadvantages of single bunch vs multi-bunch operation.* presented at the Single bunch vs. multi-bunch operation - meeting #04. accessed: 10.9.2023. URL: https://indico.cern.ch/event/1023813/.

[130] T. Kamitani et al. “SuperKEKB Positron Source Construction Status”. In: *Proc. 5th International Particle Accelerator Conference (IPAC’14), Dresden, Germany, June 15-20, 2014* (Dresden, Germany). Geneva, Switzerland: JACoW, July 2014, pp. 579–581. DOI: https://doi.org/10.18429/JACoW-IPAC2014-MOPRI004.

[131] Y. Zhao. *e+ capture section simulations.* presented at the FCC-ee Injector Studies Mini-Workshop (24.-25.11.2022). accessed: 10.9.2023. URL: https://indico.ijclab.in2p3.fr/event/8920/contributions/28015/.

[132] Y. Zhao et al. “Optimisation of the FCC-ee Positron Source Using a HTS Solenoid Matching Device”. In: *Proc. 13th International Particle Accelerator Conference (IPAC’22)* (Bangkok, Thailand). July 2022, pp. 2003–2006. DOI: 10.18429/JACoW-IPAC2022-WEPOPT062.

[133] B. Humann. *Radiation effects and Heat load.* presented at the FCC-ee Injector Studies Mini-Workshop (24.-25.11.2022). accessed: 10.9.2023. URL: https://indico.ijclab.in2p3.fr/event/8920/contributions/28013/.

[134] N. Vallis et al. “The PSI Positron Production Project”. In: *JACoW* LINAC2022 (2022), pp. 577–580. DOI: 10.18429/JACoW-LINAC2022-TUPORI16.

[135] M. K. Wu et al. “Superconductivity at 93 K in a new mixed-phase Y-Ba-Cu-O compound system at ambient pressure”. In: *Phys. Rev. Lett.* 58 (9 Mar. 1987), pp. 908–910. DOI: 10.1103/PhysRevLett.58.908.

[136] Z.H. Wang et al. "Dose Measurement Experiments for Single and Composite Targets in 6 Mev Linear Accelerators". In: *Proc. 10th International Particle Accelerator Conference (IPAC'19), Melbourne, Australia, 19-24 May 2019* (Melbourne, Australia). International Particle Accelerator Conference 10. Geneva, Switzerland: JACoW Publishing, pp. 3937–3939. ISBN: 978-3-95450-208-0. DOI: doi:10.18429/JACoW-IPAC2019-THPRB056.

[137] Y. Zhao. *Private communication*. 21.02.2023.

[138] R. R. Mena Andrade et al. *Design of the FCC-ee positron source target: current status & challenges*. presented at the FCC Week 2023. accessed: 10.9.2023. URL: https://indico.cern.ch/event/1202105/contributions/5395359/.

[139] M. Li. "Experience with moving from DPA to changes in material properties". In: *Proceedings of HB2010, Morschach, Switzerland* (Morschach, Switzerland), WEO1B05, pp. 468–471.

[140] R. Mena Andrade and J.L. Grenard. *Design of the target and integration of positron target area*. presented at the FCC-ee Injector Studies Mini-Workshop (24.-25.11.2022). accessed: 10.9.2023. URL: https://indico.ijclab.in2p3.fr/event/8920/contributions/28014/.

[141] R. Mena Andrade. *Private communication*. 24.11.2022.

[142] M. Schaer. *Private communication*. 24.11.2022.

[143] M. Schaer. *e+ linac design*. presented at the FCC-ee Injector Studies Mini-Workshop (24.-25.11.2022). accessed: 10.9.2023. URL: https://indico.ijclab.in2p3.fr/event/8920/contributions/28004/.

[144] H.W. Pommerenke. *Private communication*. 01.09.2022.

[145] A. Grudiev, H.W. Pommerenke, and R. Zennaro. *Update on Task 3.3 (Capture system: Design of the RF structures and NC solenoids)*. presented at the Joint WP3 meeting #3. accessed: 10.9.2023. URL: https://indico.cern.ch/event/1188056/\#3-update-on-task-33-capture-sy.

[146] A. Latina. "RF-Track: Beam Tracking in Field Maps Including Space-Charge Effects, Features and Benchmarks". In: *Proc. of Linear Accelerator Conference (LINAC'16), East Lansing, MI, USA, 25-30 September 2016* (East Lansing, MI, USA). Linear Accelerator Conference 28. Geneva, Switzerland: JACoW, May 2017, pp. 104–107. DOI: https://doi.org/10.18429/JACoW-LINAC2016-MOPRC016.

[147] A. Grudiev. *Private communication*. 24.11.2022.

[148] A. Grudiev. *Private communication*. 10.01.2023.

[149] B. Humann, F. Cerutti, and R. Kersevan. "Synchrotron Radiation Impact on the FCC-ee Arcs". In: *Proc. 13th International Particle Accelerator Conference (IPAC'22)* (Bangkok, Thailand). JACoW Publishing, Geneva, Switzerland, July 2022, pp. 1675–1678. ISBN: 978-3-95450-227-1. DOI: 10.18429/JACoW-IPAC2022-WEPOST002.

[150] R.P. Walker. “Synchrotron radiation”. In: (1994). DOI: 10.5170/CERN-1994-001.437. URL: http://cds.cern.ch/record/398429.

[151] M. Ady and O. Katsunobu. *Private communication*. 26.03.2020.

[152] Y. Suetsugu. “High-Intensity Synchrotron Radiation Effects”. In: (2016). Contribution to the 2014 Joint International Accelerator School: Beam Loss and Accelerator Protection, Newport Beach, CA, USA , 5-14 Nov 2014, pp. 63–82. DOI: 10.5170/CERN-2016-002.63. arXiv: 1608.02462. URL: https://cds.cern.ch/record/2206743.

[153] R. Kersevan. “The FCC-ee vacuum system, from conceptual to prototyping”. In: *EPJ Techniques and Instrumentation* 12 (). DOI: 10.1140/epjti/s40485-022-00087-w.

[154] H. Gamper and B. Humann. *Meeting Minutes of the Coordination of FCC Technology and R&D Programmes*. presented at the FCC-ee Injector Studies Mini-Workshop (24.-25.11.2022). 26.03.2021. URL: https://indico.cern.ch/event/1030771/contributions/4327978/attachments/2232349/3783433/Coordination_of_FCC_Technology_R_D_programmes__01.pdf.

[155] A. Milanese, J. Bauche, and C. Petrone. “Magnetic Measurements of the First Short Models of Twin Aperture Magnets for FCC-ee”. In: *IEEE Transactions on Applied Superconductivity* 30.4 (2020), pp. 1–5. DOI: 10.1109/TASC.2020.2976949.

[156] H. Gamper and B. Humann. *Meeting Minutes of the Coordination of FCC Technology and R&D Programmes*. presented at the FCC-ee Injector Studies Mini-Workshop (24.-25.11.2022). 22.09.2022. URL: https://indico.cern.ch/event/1217454/attachments/2545323/4383108/Coordination_of_FCC_Technology_R_D_programmes__10.pdf.

[157] A. Fassò, K. Gobel, and M. Höfert. *Lead shielding around the LEP vacuum chamber*. Tech. rep. Geneva: CERN, 1982. URL: https://cds.cern.ch/record/142098.

[158] *Tungsten Market price*. accessed: 10.9.2023. URL: https://almonty.com/tungsten/demand-pricing/.

[159] *Copper Market price*. accessed: 10.9.2023. URL: https://markets.businessinsider.com/commodities/copper-price.

[160] F. Valchkova-Georgieva. *Integration of FCC-ee*. presented at the Reuinion Integration FCC (20.7.2023). accessed: 10.9.2023. URL: https://indico.cern.ch/event/1304184/contributions/5485050/attachments/2687666/4664756/FCC\%20.07.23\%20Integration_FV.pdf.

[161] *SPECSOUR (FLUKA)*. accessed: 10.9.2023. URL: https://flukafiles.web.cern.ch/manual/chapters/description_input/description_options/specsour.html.

[162] *SYRASTEP (FLUKA)*. accessed: 10.9.2023. URL: https://flukafiles.web.cern.ch/manual/chapters/description_input/description_options/syrastep.html.

[163] *EMFCUT (FLUKA)*. accessed: 10.9.2023. URL: https://flukafiles.web.cern.ch/manual/chapters/description_input/description_options/emfcut.html.

[164] A. Wattenberg. "Photo-Neutron Sources and the Energy of the Photo-Neutrons". In: *Phys. Rev.* 71 (8 Apr. 1947), pp. 497–507. DOI: 10.1103/PhysRev.71.497.

[165] *PHOTONUC (FLUKA)*. accessed: 10.9.2023. URL: https://flukafiles.web.cern.ch/manual/chapters/description_input/description_options/photonuc.html.

[166] P. Chiggiato. *Outgassing properties of vacuum materials for particle accelerators*. Tech. rep. 47 pages. 2020. arXiv: 2006.07124. URL: https://cds.cern.ch/record/2723690.

[167] C. Hauviller. "Design rules for vacuum chambers". In: (2007). DOI: 10.5170/CERN-2007-003.31. URL: https://cds.cern.ch/record/1046848.

[168] R.W. Powell, C.Y. Ho, and P.E. Liley. *Thermal Conductivity of Selected Materials*. NSRDS-NBS Nr. 8,Bd. 1. U.S. Department of Commerce, National Bureau of Standards, 1966.

[169] F. Valchkova-Georgieva and J.P Corso. *Integration of FCC-ee RF Sections*. presented at the FCC Week 2022. accessed: 10.9.2023. URL: https://indico.cern.ch/event/1064327/contributions/4888567/.

[170] H. Schönbacher and M. Tavlet. "Absorbed doses and radiation damage during the 11 years of LEP operation". In: *Nucl. Instrum. Methods Phys. Res., B* 217 (2004), pp. 77–96. DOI: 10.1016/j.nimb.2003.09.034.

[171] National Nuclear Data Center. *Nuclear Database*. accessed: 10.9.2023. URL: https://www.nndc.bnl.gov/.

[172] A. Wallner et al. "Stellar and thermal neutron capture cross section of ^{9}Be". In: *Phys. Rev. C* 99.1 (2019), p. 015804. DOI: 10.1103/PhysRevC.99.015804.

[173] M. Silari. *A (CERN) History of Accelerator Shielding*. Tech. rep. Geneva: CERN, 2008.

[174] F. Gunsing, A. Menelle, and O. Aberle. *Determination of the boron content in polyethylene samples using the reactor Orphée*. Tech. rep. Saclay: CEA, 2017.

[175] E. Al-Dmour. *Fundamentals of Vacuum Physics and Technology*. 2020. arXiv: 2006.01464 [physics.acc-ph].

[176] R. Kersevan. *Private communication*. 04.02.2022.